UNIVERSIDADE FEDERAL DO RIO GRANDE DO NORTE
CENTRO DE TECNOLOGIA
PROGRAMA DE PÓS-GRADUAÇÃO EM ENGENHARIA CIVIL

João Paulo da Silva Costa

UPLIFT BEHAVIOUR OF HELICAL PILES IN SAND SUBJECTED TO CYCLIC LOADING

Natal – RN
2017

João Paulo da Silva Costa

UPLIFT BEHAVIOUR OF HELICAL PILES IN SAND SUBJECTED TO CYCLIC LOADING

Dissertation submitted to the Graduate Program in Civil Engineering of the University of Rio Grande do Norte in partial fulfilment of the requirements for the degree of Master of Science in Civil Engineering.

Advisor: Prof. Dr. Yuri Daniel Jatobá Costa

Natal – RN
2017

João Paulo da Silva Costa

COMPORTAMENTO À TRAÇÃO DE ESTACAS HELICOIDAIS EM AREIA SUBMETIDAS A CARREGAMENTOS CÍCLICOS

Dissertação apresentada ao Programa de Pós-graduação em Engenharia Civil, da Universidade Federal do Rio Grande do Norte, como requisito parcial à obtenção do título de Mestre em Engenharia Civil.

Orientador: Prof. Dr. Yuri Daniel Jatobá Costa

Natal – RN
2017

Universidade Federal do Rio Grande do Norte – UFRN
Sistema de Bibliotecas – SISBI
Catalogação da Publicação na Fonte - Biblioteca Central Zila Mamede

Costa, João Paulo da Silva.
Comportamento à tração de estacas helicoidais em areia submetidas a carregamentos cíclicos / João Paulo da Silva Costa. - 2017.
126 f. : il.

Dissertação (mestrado) - Universidade Federal do Rio Grande do Norte, Centro de Tecnologia, Programa de Pós-graduação em Engenharia Civil. Natal, RN, 2017.
Orientador: Prof. Dr. Yuri Daniel Jatobá Costa.

1. Engenharia civil - Dissertação. 2. Estaca helicoidal- Dissertação. 3. Ancoragem - Dissertação. 4. Prova de carga à tração - Dissertação. 5. Modelagem numérica – Dissertação. 6. Carregamento cíclico – Dissertação. I. Costa, Yuri Daniel Jatobá. II. Título.

RN/UF/BCZM CDU 624

JOÃO PAULO DA SILVA COSTA

"UPLIFT BEHAVIOUR OF HELICAL PILES IN SAND SUBJECTED TO CYCLIC LOADING"

Dissertação apresentada ao Programa de Pós-graduação em Engenharia Civil, da Universidade Federal do Rio Grande do Norte, como requisito parcial à obtenção do título de Mestre em Engenharia Civil.

BANCA EXAMINADORA

Prof. Dr. **Yuri Daniel Jatobá Costa** – Orientador
(Universidade Federal do Rio Grande do Norte/UFRN)

Prof.ª Dra. **Carina Maia Lins Costa** – Examinadora Interna
(Universidade Federal do Rio Grande do Norte/UFRN)

Prof.ª Dra. **Cristina de Hollanda Cavalcanti Tsuha** – Examinadora Externa
(Escola de Engenharia de São Carlos/EESC)

Natal, 28 de agosto de 2017

Dedicated to my parents and my brother.

Acknowledgements

First, I would like to thank God, for His infinite love and mercy.

I would like to thank my parents, Paulo and Grasiela, and my brother Geraldo for their love, support and encouragement. Warm thanks to my grandmother, Maria Pureza, for her immeasurable love and kindness.

I would like to express my sincere gratitude to my advisor, Dr. Yuri Costa, for his guidance and enthusiasm in this study. His advice, encouragement and patience have had invaluable importance for the completion of this project.

Special thanks to Dr. Olavo Santos Jr., for the opportunity of working at the soil mechanics laboratory when I was an undergraduate and sparking my interest in Geotechnical Engineering.

I would like to thank all the professors from the Civil Engineering Graduate Program, for sharing their knowledge and their passion for Engineering, especially Dr. Carina Costa and Dr. José Neres da Silva Filho, for their contributions during the qualification stage of this project. I also thank Dr. Cristina Tsuha, from USP, and Dr. Carina Costa, for their suggestions as part of the examination committee of this thesis.

Many thanks to the undergraduate students Plenyo Araújo, Alex Dantas e Gustavo Figueiredo, for their assistance during the arduous field tests.

I would also like to thank my classmates, specially Andriele, Esteban, Felipy, Nathalia, and Silvia, for their friendship and support.

Thanks to the laboratory technicians Anderson Morais, João Batista and Sandro Ricardo for their assistance and advice.

Thanks to Eng. Avelino Lourenço, representing Geoquality Geotecnia, for his advice and for providing the equipment for the load tests, to Eng. Floriano Medeiros, representing Engeo Engenharia, for proving the staff and the equipment necessary to install the piles, and to Eng. Alexandre Pereira and Murilo Delgado, representing UniFACEX, for giving access to their laboratory facilities.

I gratefully acknowledge the scholarship provided by the Coordination for the Improvement of Higher Education Personal (CAPES) and the National Council for Scientific and Technological Development (CNPq) for the grant provided for this project.

Abstract

COSTA, J. P. da S. **Uplift behaviour of helical piles in sand subjected to cyclic loading**. 2017. 126 pp. Master's Thesis – Department of Civil Engineering, Centre of Technology, Federal University of Rio Grande do Norte.

Helical piles are foundation systems used for supporting compression, tension, and lateral loads. Advantages of helical piles over other foundation systems include fast installation and possibility to apply load immediately after installation. Despite the significant growth of the use of helical piles around the world in the last 25 years, studies on the behavior of this type of foundation remain scarce. Field test results in pure sand deposits are particularly needed. In order to fulfil this demand, a field testing program involving helical piles subjected to vertical uplift loads has been conceived. A full-scale prototype of a helical pile with three bearing plates has been designed and built. Seven axial tensile load tests with cyclic loading have been performed in a pure sand deposit. Three tests were carried out with static cyclic loading, and included up to 15 load-unload cycles. Two other tests were conducted with quasi-static cyclic loading. The results of the static load tests revealed that soil-pile system stiffness increases after completion of each static loading cycle. Theoretical and empirical methods were used to predict pile ultimate static tensile load capacity, and resulted in conservative predictions as compared to the experimental field test results. The two tests with quasi-static cyclic loading were carried out with distinct mean cyclic loads and load amplitudes. The results of these tests revealed that increasing mean cyclic load and load amplitude tend to reduce pile stability and soil-pile system stiffness. The static uplift capacity of the pile was found to improve after application of quasi-static cyclic loads. Two dimensional numerical models using the finite element method were developed to evaluate how the behavior of a pile under static loading and embedded in a sandy soil profile is affected by variations of important design parameters, such as depth of installation, plate diameter, spacing between helices, and number of plates. Parametric analysis results gave insight into the distribution of stresses and strains in the soil mass around the pile, and clarified some aspects of soil-pile failure mechanisms. Uplift capacity increases linearly with depth of installation, and the pile transitions from shallow to deep failure mode when the ratio between depth and the diameter of the first helix is around four. Capacity was found to increase linearly with plate area. The failure mechanism of the pile transitions from cylindrical shear to individual capacity with a spacing ratio equal to three. It was also observed that multi-helix configurations are less efficient than single-helix piles, in the investigated conditions.

Keywords: Helical pile, anchor, pull out load test, numerical modelling, cyclic loading, sand.

Resumo

COSTA, J. P. da S. **Comportamento à tração de estacas helicoidais em areia submetidas a carregamentos cíclicos**. 2017. 126 pp. Dissertação de Mestrado – Departamento de Engenharia Civil, Centro de Tecnologia, Universidade Federal do Rio Grande do Norte.

Estacas helicoidais são fundações usadas para resistir cargas de compressão, de tração e laterais. Elas apresentam muitas vantagens em relação a outros tipos de fundações, como alta produtividade e possibilidade de serem carregadas logo após a instalação. Seu uso vem crescendo muito nos últimos 25 anos ao redor do mundo. Entretanto o volume de estudos sobre o comportamento desse tipo de fundação ainda é relativamente pequeno. Resultados de testes em campo em areia pura são particularmente necessários. Nesse aspecto, um programa de ensaios de campo envolvendo estacas helicoidais submetidas à tração foi elaborado. Projetou-se e construiu-se um protótipo em escala real de uma estaca helicoidal dotada de três hélices. Foram executados sete ensaios distintos de carregamento axial cíclico à tração, em um depósito de areia pura. Três testes foram efetuados com carregamentos cíclicos estáticos e incluíram até 15 ciclos de carga e descarga. Dois outros testes foram conduzidos com carregamentos cíclicos quase estáticos. Aumentos na rigidez do sistema solo-estaca foram observados com os resultados dos ensaios de carga estática, após a aplicação dos ciclos. Métodos teóricos e empíricos foram utilizados para prever a capacidade de carga estática à tração da estaca e produziram estimativas conservadoras comparadas aos resultados experimentais. Os testes com carregamentos quase estáticos foram feitos com valores diferentes de carga cíclica média e amplitude de carga. Os resultados desses ensaios mostraram que o aumento da amplitude e da média das cargas tende a reduzir a estabilidade da estaca e a rigidez do sistema. A capacidade de carga estática do sistema aumentou após a aplicação dos carregamentos cíclicos quase estáticos. Modelos numéricos bidimensionais utilizando o método dos elementos finitos foram desenvolvidos para avaliar como o comportamento de uma estaca sujeita a carregamento estático, em solo arenoso, é afetado por parâmetros como profundidade de instalação, diâmetro das hélices, espaçamento entre hélices e número de hélices. A análise paramétrica permitiu avaliar tensões e deformações na massa de solo adjacente à estaca, assim como esclarecer aspectos dos mecanismos de ruptura. A capacidade de carga aumenta linearmente com a profundidade de instalação e com a área das hélices. O modo de ruptura da estaca muda de raso para profundo com uma razão de profundidade próxima a quatro. O mecanismo de ruptura muda de cisalhamento cilíndrico para capacidade individual com uma razão de espaçamento igual a três. Observou-se também que configurações com mais de uma hélice são menos eficientes que aquelas com apenas uma.

Palavras-chave: Estaca helicoidal, ancoragem, prova de carga à tração, modelagem numérica, carregamento cíclico, areia.

List of figures

List of tables

List of symbols

A_g	gross cross-sectional area of the pile shaft
A_n	area of the nth helical bearing plate
A_{top}	area of the top helix
B	width of the foundation element
CS	cylindrical shear method
D	helical plate diameter
D_{avg}	average diameter of the helices
E	modulus of elasticity of the shaft steel
E_{50}	reference Young's modulus for loading
FS	factor of safety
G_s	soil specific gravity
H	depth of a helical bearing plate
H_{eff}	effective length of the shaft above the top helix
IDF	installation disturbance factor
IB	individual bearing method
K_0	at-rest coefficient of lateral earth pressure
K_h	coefficient of lateral pressure
K_t	empirical factor or torque correlation factor
KT	torque correlation factor method
L	length of the foundation element
N	number of cycles
N_{70}	SPT blow count with an energy ratio of 70
N_f	number of cycles before failure
$N_{q,pc}$	post-cyclic helix bearing capacity factor
N_q	capacity factor
N'_q	combined capacity factor
OW	one-way loading
P	load applied to the head of the pile
P'_0	effective overburden stress
Q	load applied to the head of the pile
Q_h	uplift capacity of a single helix
Q_C	static compressive capacity
$Q_{T,pc}$	post-cyclic ultimate tensile capacity
Q_T	static tensile capacity
Q_a	allowable design load capacity
Q_{cyclic}	cyclic load amplitude
Q_{inters}	difference between the minimum load of a step and the maximum load of its previous step
Q_{max}	maximum load during a cycle
Q_{max}^{field}	maximum static load achieved during a field test
Q_{mean}	mean cyclic load
Q_{min}	minimum load during a cycle
Q_{ref}	reference load, or load applied in the first step of each step
Q_s	shaft resistance
$Q_{u,modDav}^{Plaxis}$	uplift capacity obtained from Plaxis results using the modified Davisson

$Q_{u,moddav}^{field}$	uplift capacity obtained from field results using the modified Davisson criterion
$Q_{u,vdv}^{field}$	uplift capacity obtained from field results using Van der Veen's method
Q_u	ultimate uplift capacity of the pile
R_{inter}	reduction factor parameter applied to the strength between interfaces
T	installation torque
U_{acc}	accumulated pile head displacement
U_{max}	maximum displacement of the head of the pile
V	displacement accumulation rate
c'	effective cohesion
d	diameter of the pile shaft
d_c	effective diameter of a helix
d_{eff}	effective diameter of a pile shaft
d_q	depth factor
f	frequency of cycles
f_y	tensile yield strength of steel
h_w	height of the water above depth z
k	secant axial stiffness
k_L	secant axial stiffness during loading
k_U	secant axial stiffness during unloading
k_{ref}	reference secant axial stiffness
k_{res}	residual axial stiffness
m	power for stress-level dependency of stiffness
q_{ult}	ultimate bearing pressure
s	spacing between helical bearing plates
s_q	shape factor
z	depth
α	friction between the soil and the shaft
γ	unit weight of the soil
γ_{unsat}	unsaturated weight
γ_w	unit weight of water
δ	elastic deflection of a fixed-end, free-standing, frictionless pile
δ_r	residual interface friction angle between the helix material and the surrounding sand
θ_p	angle of the helical plate with the horizontal
θ	angle of the pullout cone with the vertical
λ_k	fitting factor used to calculate torque factor
λ_{SPT}	SPT blow count correlation factor
σ'_n	effective confining stress
τ	shear stress
$\tau_{y,max}$	yield shear limit of steel
υ	Poisson's ratio
ϕ	internal friction angle of the soil
ψ	dilatancy angle

Contents

1. INTRODUCTION

1.1. Context

A helical pile is a deep foundation system composed of steel helical bearing plates welded to a central steel shaft. The installation process consists of screwing the piles into the ground by the application of rotation torque. The piles can be designed to resist axial compression, axial tension, and/or lateral loads

Helical piles are used to support a variety structures built over a broad diversity of soil conditions, even problematic ones. They present many advantages over regular deep foundations, such as easy installation, simple quality control, easy mobility, and environmental friendliness. Helical piles are relatively light and cheap to transport, and can be quickly installed. In contrast to concrete piles, which require long waiting times to reach adequate strength before receiving loads, helical piles can be loaded immediately after installation, reducing costs and preventing delays in tight construction schedules. Helical piles can also be removed and reused for other tests.

Helical piles have been used in many countries for over 200 years as foundations for residences and commercial buildings, and as tensile members for retaining wall systems and utility guy anchors in projects of all sizes. The use of helical piles in Brazil initiated in 1998, in the construction of towers for power transmission and telecommunications. Since then, many contractors have specialized in this field.

Despite their growing usage, research on helical piles is still very limited in Brazil. Understanding the behaviour of such foundation systems in pure sand deposits, which are common throughout the coast of northeast Brazil, is therefore of vital importance. Also, to the best knowledge of the author, there are few works in worldwide literature on the static performance of full-sized piles in pure sand and virtually none of them describes cyclic performance.

The scarce technical literature about helical piles in Brazil and the insufficient research about the performance of this type of foundation are some of the reasons that motivate this research.

1.2. Objectives

The main objective of this research is to study the behaviour of helical piles subjected to static and cyclic loadings, installed in a pure sand deposit.

The specific objectives of this work are:

a) Design, build and test a helical steel pile prototype.
b) Evaluate the static load-displacement response of the pile in uplift conditions, from results of field tests performed in a pure sand deposit.
c) Compare the experimental results from the field static load tests with predictions from design methods of helical piles proposed in the literature.
d) Evaluate the cyclic load-displacement response of the pile in uplift conditions, from results of field tests performed in a pure sand deposit.
e) Evaluate the degradation of stability of the pile caused by the application of cyclic load cycles.
f) Investigate changes in static capacity after the application of quasi-static load cycles.
g) Validate a FEM numerical model of the static loading tests against experimental results.
h) Evaluate the effect of specific design parameters (i.e. plate diameter, space between plates, depth of installation, and number of plates) on the response of helical piles in pure sand.

1.3. Text organization

This research was structured in five chapters:

- Chapter 1 presents the context in which this research was conceived and the objectives of this work.
- Chapter 2 contains a review of the literature related to the use, design, and testing of helical piles. It first introduces the definition of helical piles and related concepts. This is followed by the usage of helical piles throughout history, modern applications and advantages over other types of foundation systems. Then it presents installation practices, methods to estimate uplift capacity, and procedures used in static and cyclic load tests.

- Chapter 3 presents the materials and methods used in this work. It starts with a description of the research site, including the geological and geotechnical characterization obtained from field experiments and laboratory tests. After this, the methods used for the static and quasi-static load tests are described. At last, it describes how the numerical modelling was conducted.
- Chapter 4 presents and discusses the results from experimental tests and numerical simulations.
- Chapter 5 presents a summary and the conclusion of this work and suggests fields of potential future research.

2. LITERATURE REVIEW

This work evaluates the behaviour of helical piles subjected to static and quasi-static cyclic axial tensile loads. In this chapter, it is presented a review of the available literature concerning helical piles, including the terminology related to its use, basic features, mechanisms affecting load capacity, methods for predicting load capacity, and behaviour when subjected to cyclic loads.

2.1. Definition and terminology

The International Code Council (2014) defines helical piles as manufactured steel deep foundation elements consisting of a central shaft and one or more helical bearing plates. Each helical bearing plate is formed into a screw thread with uniform distance between the leading and the trailing edge, known as pitch. Installation consists in connecting its top end to a hydraulic motor and applying a torque while pressing it against the ground.

According to Perko (2009), a helical pile is composed of a lead section, extensions, a helical bearing plates and a bracket, as shown in Figure 2.1. The lead section has a tapered pilot point and is the first to enter the ground. It contains one or more helical bearing plates. Extension sections are used to increase the depth and are attached to the pile during installation into the ground until the helical bearing plates reach the required soil stratum or another condition is reached. Helical bearing plates (or helices) can be welded to the extension sections when required. The coupling between sections often uses male and female sleeves and bolts.

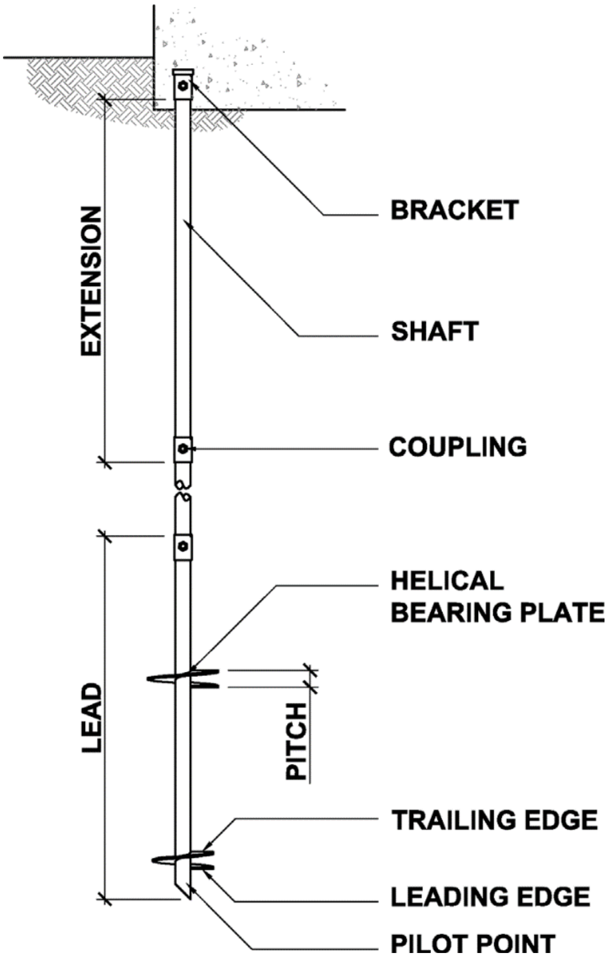

Figure 2.1 – Elements of a helical pile (Perko, 2009).

The term used to refer to helical foundations differs depending on their application, time and place, according to Perko (2009). The original device was named “screw pile”. Between 1920 and 1980, the frequent application for tension turned the term “helical anchor” more common. Manufacturer Hubbell Power Systems, Inc. trademarked the name “helical pier” to promote its compression applications. The system has also been called “helix pier”, “screw pier”, “helical foundation”, “torque anchor”, and others. In 2005, the Deep Foundation Institute decided, through its Helical Foundations and Tie-Backs committee, to henceforth use the term “helical pile”. “Helical anchor” is also used when referring to tension applications. This work focuses on the use of helical piles for tension applications but adopts the more generic phrase “helical pile”, except when a distinction between foundation and anchor applications is required.

2.2. History of helical piles

Perko (2009) recounts some of the most important moments in the history of helical piles. The patent regarding the invention of helical piles was filed in 1833, in London, by Alexander Mitchell, a blind brick maker and civil engineer. One of the first uses for screw piles was ship moorings. Lighthouses were the first buildings where helical piles were used as foundation elements. The Maplin Sands lighthouse, located on an unstable bank near the Thames estuary, was built on helical pile foundations, as illustrated in Figure 2.2. The invention of helical piles allowed the construction of lighthouses on previously inaccessible places. In 1853, Eugenius Birch adopted Mitchell's technology to support seaside piers throughout England. During the expansion of the British Empire, helical piles were used to build new bridges in many countries. From the 1850s through the 1890s, helical piles were used as foundations on more than 100 lighthouses along the East Coast of the United States and along the Gulf of Mexico.

Figure 2.2 – Whole model of the Maplin Sands lighthouse patented by Alexander Mitchell (Science Museum Group, 1838-1887).

Perko (2009) also reports that the use of helical piles declined from about 1900 to 1950 while major developments in pile-driving and drilling equipment occurred, ushering in an era of new types of deep foundations, such as Raymond drilled foundations, belled piers, and Franki piles. The modern helical pile resulted from the development of modern hydraulic torque motors, advances in manufacturing, and new galvanizing techniques, with its use focused on anchor applications. The first compression application of helical piles in the U.S. was designed by engineer Stan Rupiper around 1980.

Perko (2009) studied early U.S. patents related to helical piles. He notes that some designs included continuous spirals. The spirals were later considered unnecessary because of group effects within the soil and their capacity was equivalent to that of single helical bearing plates spaced along the length of the shaft.

Other patents are related to methods for enhancing the lateral stability of a slender helical pile shaft in soil. According to Perko (2009), in 1961, Galloway and Galloway patented a method of placing three triangular plates on a swivel located on the trailing end of a helical pile. Another way to enhance lateral resistance is to increase shaft diameter, a method used by many helical piles manufactures producing light pole bases.

U.S. patents filed regarding helical piles can be grouped generally into four categories or historical eras (Perko, 2009). The period from the invention of the screw pile to 1875 can be generally termed “Marine Era”, when helical piles were used for ship moorings, lighthouses, and other marine structures. Beginning in 1878 and ending in 1931, most of the patents involve fence post applications. This period is named “Agricultural Era”, after the developments in irrigation and plant/soil science during the same time frame. The period between about 1920 to the 1980s is called “Utility Era”, when most patents regard guy anchors, tower legs, utility enclosures, and pipelines. This period corresponds to significant infrastructure projects in the United States. The last group can be termed “Construction Era”. The patents were issued from about 1985 until the present, and are related to buildings and other construction applications.

2.3. Applications of helical piles

The diversity of structures where helical piles can be applied has been reported by many authors (Livneh and El Naggar, 2008; Perko, 2009; Clemence and Lutenegger, 2015). Helical piles can resist compressive, tensile and lateral loads. They can be installed at any angle to improve their capacity against inclined loads. Applications around the world include foundations for houses, commercial buildings, light poles, pedestrian bridges, and sound walls. They can be used as underpinning elements to repair failed foundations or to augment existing foundations to support additional loads. As tensile members, helical piles are used for retaining wall systems, utility guy anchors, membrane roof systems, pipeline buoyancy control, transmission towers, and many other structures. The main application of helical piles in Brazil is in transmission towers, as guyed masts and self-supporting towers (Schiavon, 2016).

2.4. Advantages over other foundation systems

Perko (2009) and Nazir *et al.* (2014) highlight the advantages offered by helical piles over other types of foundations. The installation process is fast and load can be applied immediately, unlike concrete, which takes time to set. Installation machinery is smaller and more manoeuvrable than pile-driving and pile-drilling rigs. The installation process does not produce spoil, excessive vibrations, or disruptive noise, and allow helical piles to be installed in environmentally sensitive areas. Portable equipment can be used in areas of limited access. Helical piles can be removed and reinstalled, which is ideal for temporary applications, correcting location or change of plans. Helical piles are also unaffected by caving soils and groundwater and resist frost heave and expansive soils. The helical pile shaft has a high dampening ratio and can be used to resist vibrations coming from heavy manufacturing equipment. Helical piles can be used in almost any weather condition.

Perko (2009) also argues that helical piles are environmentally sustainable foundation systems. The environmental footprint of many projects where concrete and common steel piles are used can be reduced by replacing these solutions with helical piles. Foundations using helical piles require about 65 percent less raw material by weight to construct as compared to driven steel piles and 95 percent less as compared to drilled shafts or cast auger piles. This means less traffic, less pollution, and less wear-and-tear on roads, streets, and highways. The replacement of concrete by helical piles can also reduce the overall cost of foundations, especially in remote sites.

The benefits of helical piles can be summarized as follows (Perko, 2009):

- Resistance to scour and undermining for bridge applications.
- Possibility to be removed for temporary applications.
- Easy transportation to remote sites.
- Pile bearing capacity can be verified by torque measurements.
- Fast installation.
- Installation in battered angles for additional lateral resistance.
- Need of smaller, more accessible equipment.
- Installation with low noise and minimal vibration.
- Possibility to be grouted in place after installation.
- Corrosion-resistant after galvanization.
- Elimination of concrete curing and formwork.
- Elimination of drill spoils.
- Minimization of disturbance to environmentally sensitive sites.
- Reduction of number of truck trips required to a site.
- Cost effectiveness.

2.5. Installation

2.5.1. General procedures

Installation of helical piles is simple but requires proper equipment and procedures, so consistent results can be achieved. The procedures described in this item were detailed by Perko (2009) and the Hubbell Power Systems (2014). The process consists of turning the pile shaft into the ground by application of a rotating moment (torque) using an auger or hydraulic torque motor attached to a truck or other hydraulic machine. The hydraulic torque motor is used to apply torsion to the top of the helical pile.

Helical piles should be installed with high-torque, low-speed torque motors, which allow the helical bearing plates to advance with minimal soil disturbance. Torque motor commonly used for helical pile installation produce a torque of 6,000 to 100,000 N-m, or higher. The torque motor should have clockwise and counter clockwise rotation capability and should be adjustable with respect to revolutions per minute during installation. Hydraulic machinery should be capable of applying crowd and torque simultaneously to ensure normal advancement of helical piles.

The connection between the torque motor and helical piles should be in-line, straight, and rigid, and should consist of a hexagonal, square, or round adapter and helical shaft socket.

A convenient aspect of most helical piles is that the capacity can be verified from the installation torque. The capacity is experimentally and theoretically well established. A torque indicator should be used to measure torque during installation. Torque motors operated by hand can also be used to install helical piles.

The installation process is described as follows:

- The first piece of the pile to be installed is the leading section. It must be attached to the torque motor using a drive tool and a drive pin, then it should be positioned and aligned at the desired position and inclination.
- The pilot point should be pushed downward until it touches the ground surface. Plumbness and alignment should be checked.
- Rotation and crowd should be applied at the same time. The sections should be advanced into the soil in a continuous manner at a rate of rotation typically less than 30 rpm.
- As the installation continues, plumbness and alignment must be checked regularly. Installation torque and depth should be recorded periodically.
- Rotation should be stopped so that the drive pin can be seen.
- Extension sections are added until the required depth or installation torque is achieved.
- The shaft should then be cut to the elevation required for the project.
- Bolt holes should be drilled at the end of the shaft to allow mounting the top cap. Helical pile caps can consist of brackets for compression applications or thread bars attached to a sleeve for tension applications.

“Crowd”, or downward thrust, is a constant axial force that should be applied while rotating helical piles into the ground. Optimally, the crowd applied should be enough to make the pile advance one blade pitch during after each revolution. Insufficient crowd can result in augering.

Helical piles are installed until a set of conditions is achieved. These conditions can include required installation torque based on empirical correlations, or minimum depth, to ensure the bearing plates reached the planned stratum. Torsional strength of the helical pile should not be exceeded.

When the required installation torque is not achieved within a reasonable depth, the contractor and the engineer have some options available:

- Use additional extension sections to make the helical bearing plates reach a deeper stratum.
- Add extension sections with bearing plates.
- Remove the helical pile and install another with more and/or larger helical piles.
- Decrease the rated loaded capacity of the pile and install new piles to resist the load.

The calculation of bearing or pull-out capacity for pile design should be based on traditional soil boring information, and installation torque should be used as a method of field verification of ultimate capacity.

Helical pile designs should consider small variations in location and orientation. Typical tolerances are +-25 mm for location and +- 5 degrees for orientation.

The direction of the torque should never be reversed during installation. Typical tolerances for elevation of the top end of the shaft range from +25 mm to -13 mm.

Predrilling is not common in practice. If the process is required, Sakr (2010) recommends limiting its depth to about one helix diameter above the top helix to prevent disturbing the bearing stratum for the top helix.

Helical pile installation requires a person to operate the hydraulic machine and a spotter who handles the pile sections and performs coupling duties.

The location of all underground utilities, such as electrical, gas, high-pressure water, or communication lines should be known by the engineer in charge of specifying the position of the helical piles. A helical pile encountering an underground line can result in high repair costs, serious injury, or death. Public and private service companies are available for locating underground utilities. The minimum recommended distance between a helical pile and an underground utility is three helix diameters or 0.30 m plus the uncertainty in the location, whichever is greater.

In tension applications, Livneh and El Naggar (2008) recommend that the centre-to-centre spacing between two adjacent piles should be a minimum distance of five helix diameters to prevent interaction between the piles and ensure the capacity of each pile will be fully mobilized.

2.5.2. Effects of installation disturbance

Installation and testing procedures cause the displacement of the sand particles, as observed by Schiavon (2016). The author performed excavations in sand samples after installation and after uplift loading. It was observed that installation makes the soil above the helix rise upwards and drags the soil close to the shaft down. After uplift, it was observed that the pile response depends on the properties of the disturbed soil right above the helix. Micro-tomographic images from the samples show the installation of the helix results in a cylindrical zone of disturbed material, i.e., less dense sand.

Tsuha *et al.* (2012a) studied how the number of helical plates influence uplift capacity and observed that, although capacity generally increases with number of helices, it is also affected by the relative density of sand. The authors suggest that in sands with low relative density, the penetration of the first helix causes total loosening of the particles and no additional loosening is caused by the passage of other helices, as illustrated in Figure 2.3a. In contrast, the high degree of compactness of dense sands is reduced by the passage of the first helix but can be reduced further still by the penetration of additional plates, as shown in Figure 2.3b.

Disturbance in the soil caused by installation of helical piles should be kept to a minimum. Lutenegger *et al.* (2014) proposes quantifying installation disturbance using an Installation Disturbance Factor (IDF), expressed as a ratio between the measured and the ideal number of revolutions per unit of advance. According to the authors, a high-quality installation is one in which the pile would advance one pitch distance for each complete revolution, what corresponds to a value of IDF equal to 1. Difficult or poor-quality installations have values as high as 4 or 5. Ideally, each helical plate should cut through the soil only once. According to Ruberti (2015), the loss of strength associated with disturbance is more important when dealing with sensitive fine-grained soils. The author suggests that the effect of the quality of installations may be less noticeable in sands because they are free draining and their strength is almost not affected by remoulding.

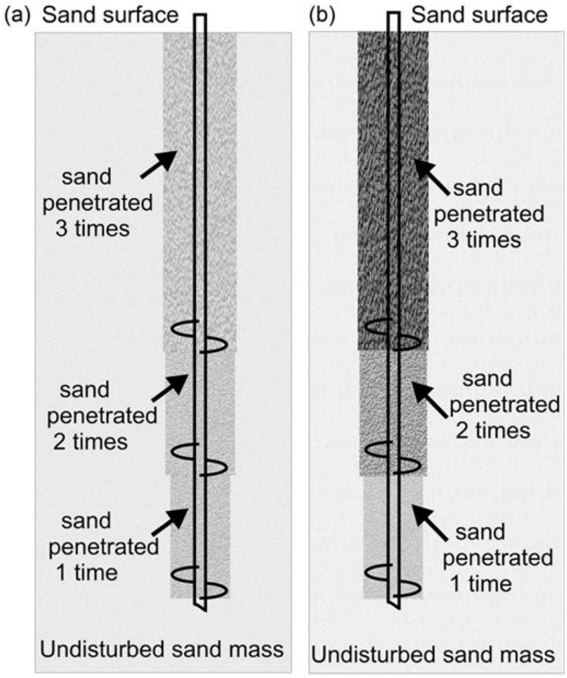

Figure 2.3 – Illustration of the hypothesis for sand disturbance after installation of a three-helix anchor: a) loose sand; b) dense sand (Tsuha *et al.*, 2012a).

Another approach to study the effect of installation disturbance is comparing the bearing and the uplift capacities of helical piles installed in the same soil. Zhang (1999) found that the bearing capacity of multi-helix piles in compression was almost twice the capacity in tension in cohesive and cohesionless soils. According to the author, the soil mobilized during uplift was disturbed during installation while the soil below the bottom helix, mobilized in compression, was undisturbed.

Lutenegger and Tsuha (2015) reported ratios between tension and compression capacities between 0.70 to 0.79 in piles installed in silty sand.

Gavin *et al.* (2014) performed compression and tension load tests in dense sand and observed that the tensile capacity was between 30% to 50% of the compressive capacity.

Schiavon (2016) performed centrifuge tests on model anchors in steel strongboxes filled with sand through raining deposition technique and found the opposite behaviour. Anchors placed before sand deposition, to prevent the disturbance caused by installation, exhibited lower uplift capacity than anchors installed in flight. The author attributed the behaviour to a limitation in the deposition process, causing the zone of sand around the models was actually less dense than the rest of the sample resulting in reduced uplift capacity.

Schiavon (2016) also performed micro-tomographic analysis on a model anchor to investigate density changes in sand after installation. A micro-tomographic image of the longitudinal section shows that the sand around the helix and around the shaft present different densities compared to the rest of the sand specimen. The study also showed that the uplift movement of a model anchor after the application of a tensile load caused the formation of a gap and a less dense sand zone below the helix. The author observed that the application of upward movement to the anchor caused the displacement of sand particles around and below the plate towards the gap. The movement of the particles is illustrated in Figure 2.4.

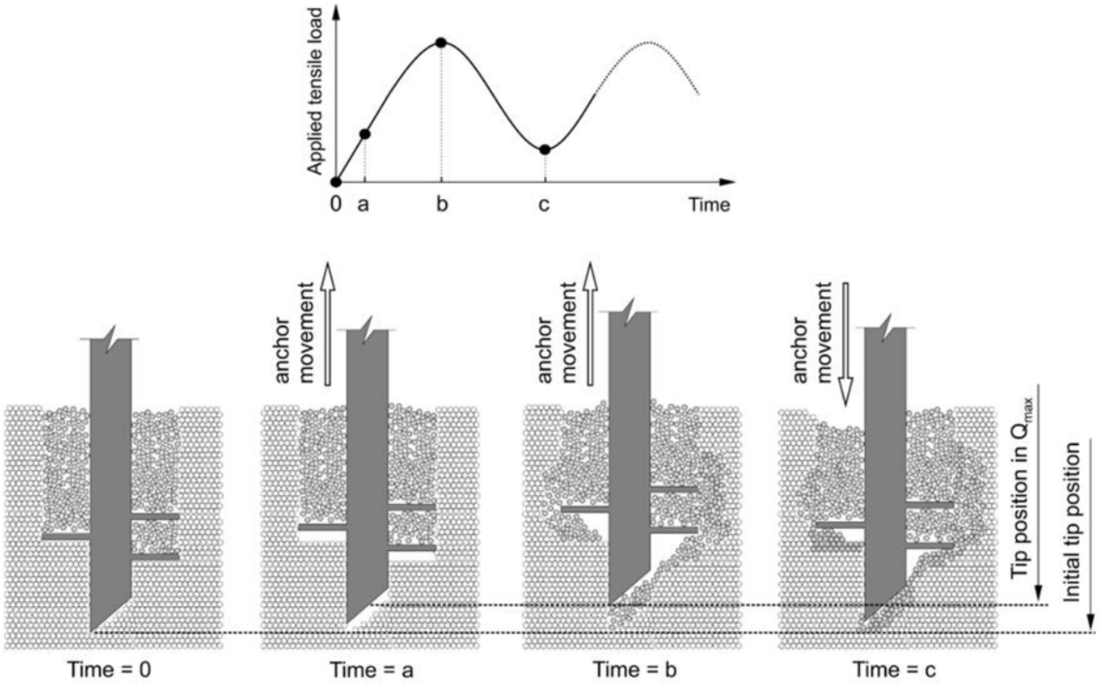

Figure 2.4 – Gap formation and sand particles movement during cyclic loading (Schiavon, 2016).

2.5.3. Installation torque measurements

Installation torque measurements are recommended on all projects. For safety reasons, the installation torque should be limited to not exceed the torsional capacity of the pile. It was also verified that a correlation between the installation torque and the capacity of the piles exist (Hoyt and Clemence, 1989). According to Clemence and Lutenegger (2015) it is common practice to measure the torque in modern projects.

Several methods are available to measure torque during pile installation (Perko, 2009):

Shear pin indicator. This method consists of two plates attached together by a central hub. One of the plates is attached to the helical pile and the other is attached to the torque motor. The plates have holes arranged along the perimeter where calibrated shear pins are placed. The pins shear at a known torque and provide a one-time measurement of the applied torque. This solution is less expensive than other solutions, provides accurate measurements and can be used to limit the maximum installation torque. Because of the nature of the solution, only the final torque can be measured, whereas other solutions can provide continuous logs. Reloading the pins can also be difficult.

Mechanical dial gauge. This method uses a spring-actuated strain transducer and the measurements are read from a dial gauge. It provides continuous torque readings and does not require electric power. Since the dial gauge rotates with the pile, readings can be missed by the observer.

Electronic load cells (transducers). Load cells contain strain gauges that detect elastic deformation of the steel housing under torsion. They can be very accurate and provide direct measurements of torque. The torque can be read from an external display and be logged on a portable electronic device. Load cells, however, can be expensive.

Pressure drop across a hydraulic motor. This method can provide the installation torque indirectly through measurements of the pressure drop across a hydraulic motor. The motor should be calibrated to obtain an accurate correlation between pressure drop and torque. Calibrations should be performed periodically, since motors can lose efficiency over time. Torque correlation curves are also affected by other factors such as hydraulic fluid viscosities and operating temperatures. Methods based on differential pressure are less accurate than readings from load cells.

The simplest way to measure torque is installing a helical pile to the maximum torque provided by a torque motor, when the stall torque of the motor is known. The stall torque method is frequently used on small projects with success.

One general recommendation is to calibrate torque measurement devices at least once a year and whenever torque readings are questionable. Standard uncertainty can be determined using a spreadsheet and calculating correlations between measured torque and actual torque. Accepting the uncertainty of the method of measuring torque depends on how critical the project is and on the variability of underground conditions. Perko (2009) also recommends that multiple sources should be used to obtain reliable torque measurements.

2.6. Site suitability

Subsurface investigations are used to help identify the best foundation solutions for a given soil profile. Helical piles can be used in most soil conditions where deep foundations are being considered, including expansive soils, unknown fill, and collapsible soils.

Shallow foundations are often the preferred solution for new constructions because they are relatively inexpensive when placed on stable soils, like dense sand and gravel, and stiff clays with low expansion/shrinkage potential. When new foundations are required inside existing buildings, remotes sites, and other places of limited access, helical piles have advantages over shallow foundations that might result in lower final costs. Soth and Sailer (2004) reported helical piles are cost less than footings and concrete stem walls for support of residential additions due to the lower costs associated with excavations and time for construction.

According to Hubbell Power Systems (2014), site investigations are required for helical piles installations because of the following reasons:

- To determine the depth and the thickness of the soil layer that will provide bearing for the helical plate.
- To establish the location of weak zones, that can compromise the stability of the pile.
- To locate the groundwater table.
- To determine the presence of materials that can obstruct the progress of the pile installation.
- To evaluate the corrosion potential of the foundation.

Perko (2009) describes some soil conditions that can be a hindrance to the installation of helical piles, but argues that most of the problems can be overcome. Difficult soils include thin layers of very dense or very hard materials, which require increased crowd or previously drilling pilot holes. Discontinuities in soil strength also require increased crowd or additional helices. The frequency and the arrangement of cobbles and boulders may require the helical piles to be removed and relocated. According to Bobbitt and Rogers (2006), hitting boulders and cobbles may fold the leading edge and the damage can result in reduced capacity. When relocation is not possible, contractors should use helices with thicker plates or made from steel with higher strength.

2.7. Design of helical piles

2.7.1. Overview

This item presents the most common methods for calculating theoretical ultimate axial static tensile load capacity of helical piles. Individual bearing and cylindrical shear methods described are based on traditional limit state analysis. These methods can be used to calculate both compressive and tensile strength of a pile, provided sufficient embedment to ensure deep anchor behaviour.

The failure mechanism of a multi-helix pile depends on the spacing (s) between the bearing plates. Larger spacing leads the plates to behave independently, and the ultimate bearing capacity of the pile will be equal to the sum of the individual capacities of all bearing plates. In this case, the pile ultimate bearing capacity can be predicted by the "individual bearing" method (Hoyt and Clemence, 1989).

On the other hand, smaller spacing between helical bearing plates makes the plates behave as a group. The total bearing capacity of the pile will then be equal to the bearing capacity of the cylinder of soil encased between the uppermost and the lowermost helices, plus the bearing capacity of the bottom helical bearing plate, for compression applications, or the bearing capacity of the top helical bearing plate, for tension applications. In this case, the theoretical cylinder capacity is calculated by the "cylindrical shear" method (Hoyt and Clemence, 1989).

How the proximity between plates influence the overall behaviour of the soil-pile system depends on several aspects, which include pile geometry and surrounding soil conditions. Therefore, both methods should be used to determine the capacity and the least value should be adopted as the limiting state.

According to Perko (2009) when helical bearing plates are optimally spaced, the results from the two theoretical methods will be equal, resulting in no wasting of shaft length or helical bearing plates. Seider (2004) reports that optimal spacing is commonly taken as two to three times the average diameter of the helical bearing plates, for shaft sizes from 38 mm square to 89 mm diameter in most soil types.

Perko (2009) recommends that the space between piles should be defined in increments of the pitch so that the plates track the same path during installation, reducing soil disturbance.

Spacing between helical bearing plates is usually quantified by the inter-helix spacing ratio, defined as the spacing between helical bearing plates divided by their average diameter. The spacing considered optimal and used as industry standards is three times the diameter of the lower helix (Hubbell Power Systems, 2014).

2.7.2. Individual bearing method

According to Perko (2009), this method assumes that each helical bearing plate displaces the soil in a characteristic deep bearing failure mode, which means the weight of soil each helix can provide sufficient pullout pressure (failure modes are discussed in item 2.7.10). A schematic distribution of stresses on a helical pile in the individual bearing method is shown in Figure 2.5. It shows the pressure is uniformly distributed on the upper side of each helical pile. Lateral resistance develops along the entire length of the shaft.

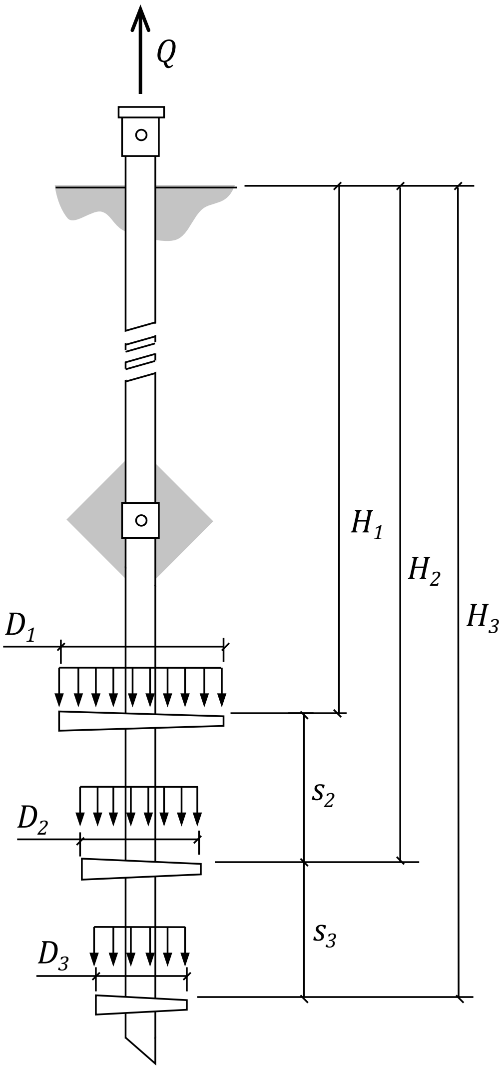

Figure 2.5 – Individual bearing method for helical piles (after Perko, 2009).

The procedure used to determine ultimate tensile load is similar to that used for ultimate compressive load, provided the pile are sufficiently embedded in the ground to ensure a deep mode of behaviour. The ultimate uplift capacity of the pile, Q_u, is the sum of individual bearing capacities of the helical bearing plates plus friction along the shaft, given by Equation 2.1.

$$Q_u = \sum_n q_{ult} A_n + \alpha H_{eff} (\pi d) \tag{2.1}$$

Where q_{ult} = ultimate bearing pressure; A_n = area of the nth helical bearing plate; α = friction between the soil and the shaft; H_{eff} = effective length of the shaft above the top helix; and d = diameter of the pile shaft.

When the ultimate bearing pressure is not available, it can be calculated for helical piles using equation 2.2 (Perko, 2009):

$$q_{ult} = 2D_{avg}\gamma N'_q \tag{2.2}$$

Where: D_{avg} = average diameter of the helices; γ = unit weight of the soil; and N'_q = combined bearing factor, calculated using Equations 2.3 to 2.6.

$$N'_q = N_q s_q d_q \tag{2.3}$$

$$N_q = e^{\pi \tan\phi} \tan^2\left(45° + \frac{\phi}{2}\right) \tag{2.4}$$

$$s_q = 1 + \frac{B}{L}\tan\phi \cong 1 \tag{2.5}$$

$$d_q = 1 + 2\tan^{-1}\left(\frac{H}{B}\right)\tan\phi\,(1-\sin\phi)^2 \cong 1 + \pi\tan\phi\,(1-\sin\phi)^2 \tag{2.6}$$

The original concept of bearing capacity factors was developed by Terzaghi (1943). Meyerhof (1951) refined the formulas and proposed factors for shape of the bearing element and depth. The shape and capacity factors were redefined later by Hansen (1970) and Vesic (1973), respectively.

Penetration test blow count in coarse-grained soils can be used to estimate the ultimate bearing pressure, q_{ult}, in uplift. Perko (2009) suggests the correlation expressed in Equation 2.7. The author compared the predicted axial capacity with the capacity measured in 54 load tests and found the results are more consistent than those using bearing capacity factors.

$$q_{ult} = 12\lambda_{SPT}N_{70} \tag{2.7}$$

Where: λ_{SPT} = 6.2 kPa/blow/30 cm; and N_{70} = SPT blow count at an energy ratio of 70.

2.7.3. Cylindrical shear method

In the cylindrical shear method, it is assumed that the entire volume of soil between the helical bearing plates is mobilized. A free body diagram showing the forces acting on a pile in the cylindrical shear method are shown in Figure 2.6. In uplift applications, uniform pressure is distributed above the top helix, and shear stresses are distributed around the soil encapsulated between the helical bearing plates. Friction develops along the length of the helical pile shaft above the top helix.

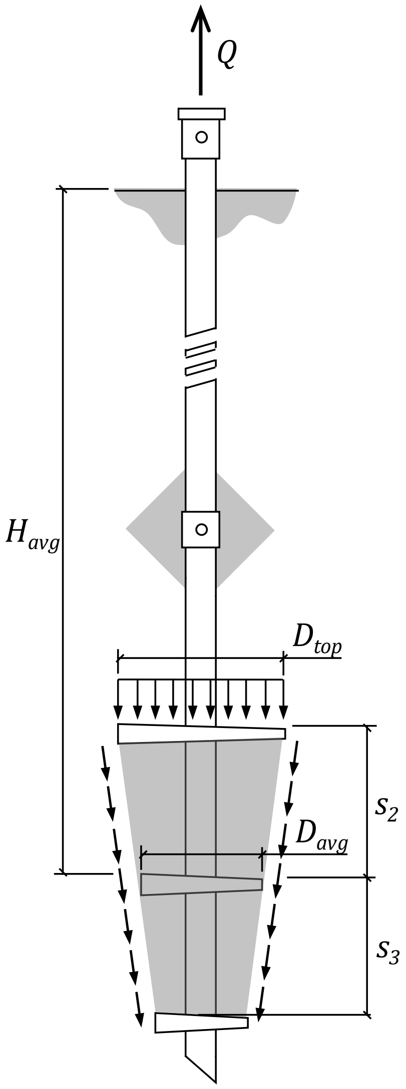

Figure 2.6 – Cylindrical shear method for helical piles (after Perko, 2009).

The ultimate uplift capacity of the pile, Q_u, is the sum of shear stress along the cylinder, adhesion along the shaft, and bearing capacity of the top helix (Equation 2.8).

$$Q_u = q_{ult}A_{top} + \tau(n-1)s\pi D_{avg} + \alpha H_{eff}(\pi d) \qquad (2.8)$$

Where: A_{top} = area of the upper helix; τ = soil shear strength; and $(n-1)s$ = length of soil between the helices. All other parameters have been defined previously.

In coarse-grained soils, the shear strength depends on the effective confining stress, σ'_n. In undisturbed ground, the effective confining stress at a depth z can be calculated with Equation 2.9.

$$\sigma'_n = K_0 P'_0 \tag{2.9}$$

Where: K_0 = at-rest coefficient of lateral earth pressure; and P'_0 = effective overburden stress at depth z.

Ideal installation of helical piles causes minimal disturbance when threading the soil, but the soil displaced laterally by the pile increases the lateral stresses immediately adjacent to the pile. Mitsch and Clemence (1985) computed inter-helix shear stress from several load tests and recommended lateral earth pressure coefficients based on internal friction angle, ϕ, shown in Figure 2.7. Equation 2.10 is the best-fit regression for the results.

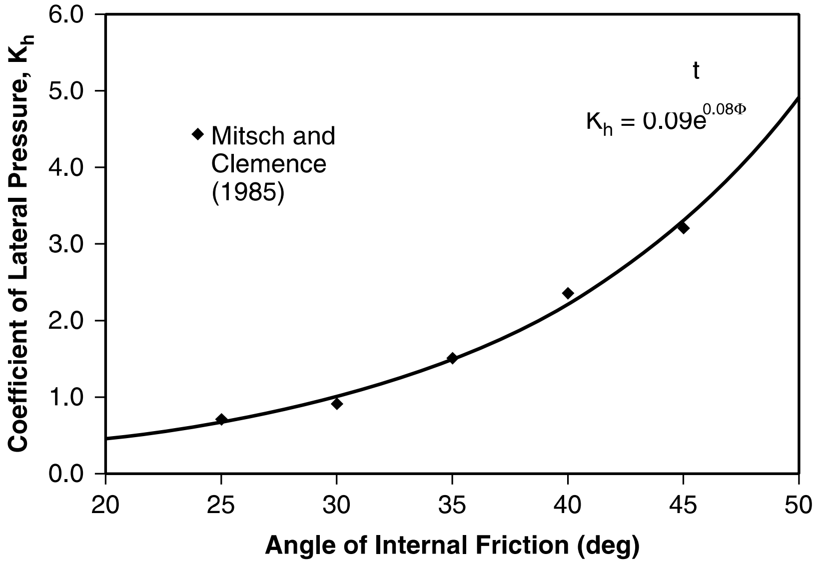

Figure 2.7 – Lateral earth pressure coefficient for cylindrical shear method (Perko, 2009, adapted from Mitsch and Clemence, 1985).

$$K_h = 0.09e^{0.08\phi} \tag{2.10}$$

Shear stress acting on the cylinder can be calculated by combining equations 2.9 and 2.10 into equation 2.11:

$$\tau = \left(0.09e^{0.08\phi}\right)(\gamma z - \gamma_w h_w)\tan\phi \tag{2.11}$$

Where: h_w = height of the water above depth z.

2.7.4. Shaft friction

Shaft friction is usually ignored when using correlations because shaft geometry, coupling sleeves, and wobbling loosen the soil close to the shaft. Research using instrumented piles by Gavin *et al.* (2014) and Schiavon (2016) found that the majority of axial resistance is provided by the stress mobilized on the helical plate in static and quasi-static cyclic uplift loads, respectively. In some cases, however, the shaft-soil interface may exhibit significant strength. Deep piles with large-diameter shafts and smooth shafts with flush couplings are examples in which friction is not negligible. Shaft friction can be approximated by Equation 2.12. This reduction factor is adopted for bare or galvanized steel. Different factors may be appropriate for other surface finishes.

$$\alpha = \frac{2}{3}\tau \tag{2.12}$$

Narasimha Rao, Prasad, and Veeresh (1993) recommend the shaft length where friction is considered should be limited to an effective shaft length (H_{eff}). Zhang (1999) concluded that H_{eff} can be approximated by subtracting the diameter of the upper helix from the available shaft length

2.7.5. Limit state analysis

Both the individual bearing and the cylindrical shear methods should be used to predict the theoretical capacity of helical piles. The smallest value should be used as the predicted ultimate pile capacity. This procedure defines the limit state of the pile.

After evaluating the results from static load tests, Perko (2009) affirms that, although the theoretical predictions for bearing and pull-out capacity should be similar, in practice they differ, which may be attributed to the disturbance of the soil above the helical bearing plates caused by the installation process, as commented in item 2.5.2. He recommends that conservative designers may use a reduction factor of 0.87 to multiply the results obtained from limit state analysis.

2.7.6. Capacity-to-Torque Ratio

The torsional energy required to install a helical pile can provide a reliable mean to predict its load capacity (Hubbell Power Systems, 2014). An empirical relationship between installation torque and load capacity was developed by the Hubbell Power Systems, Inc. in the late 1950s and early 1960s. This method has been used to verify the load capacity during installation and is one of the advantageous features of helical piles.

The capacity-to-torque ratio method is based on the assumption that the amount of torque required to make the helical bearing plates cut through the soil would indicate the soil strength.

The data regarding the relationship between helical pile capacity and installation torque was kept proprietary until disclosure by public agencies (Gill and Udwari, 1980). Hoyt and Clemence (1989) were the first to publish the relationship in professional literature. Based on empirical data and experience, they proposed the Equation 2.13 to calculate the total anchor capacity:

$$Q_u = K_t T_{avg} \tag{2.13}$$

Where: Q_u = uplift axial capacity; K_t = empirical factor or torque correlation factor; and T = average installation torque

The parameter K_t is also known as the capacity-to-torque ratio and has units of m^{-1}. It depends only on the size and shape of the shaft cross section. The value of torque used in the equation is the average of the torque measured in the final distance of penetration, equal to three times the diameter of the largest helix.

Hoyt and Clemence (1989) compared the results from pull-out tests with predictions obtained from the cylindrical shear, the individual bearing and the capacity-to-torque ratio methods, and concluded that the torque correlation method yielded more consistent results than either of the other two methods.

The capacity-to-torque ratios adopted by the Acceptance Criteria 358 (ICC-ES, 2007) are similar to the empirical values used by Hoyt and Clemence (1989). Based on a more extensive sample of test results, Perko (2009) suggests calculating the empirical factor K_t using the following best-fit empirical equation:

$$K_t = \frac{\lambda_k}{{d_{eff}}^{0.92}} \tag{2.14}$$

Where: λ_k = fitting factor equal to 1433 mm$^{0.92}$/m; and d_{eff} = diameter of round shafts or the diagonal distance between opposite corners of square shafts.

Tappenden (2006) observes that values of torque correlation factors obtained from regression analysis (Equation 2.14) correspond well to values obtained from tests performed on larger sized shafts.

Livneh and El Naggar (2008) found that other factors besides geometry affect the correlation factors, such as the relative density of the soil and if the load is applied in compression or tension. The authors performed load tests and found that the torque correlation factors obtained from the experiments were smaller than those obtained from regression analysis. Equation 2.18 estimates a torque correlation factor of 31.4 m^{-1} for a pile with 45 mm square shaft. The authors obtained correlation factors between 26.1 and 62.1 m^{-1} for compression and between 21.3 and 36.3 m^{-1} for tension. The upper range of values corresponded to piles tested in dense silt and sand and the lower range was for piles tested in clayey silt.

The use of torque measurements during helical pile installations should be used to supplement the data collected from traditional soil survey methods. Although SPT blow count and CPT tip resistance can be estimated from torque measurements, it is not advisable to replace the penetration tests entirely. Precious information, like soil type, cannot be obtained from torque measurements.

2.7.7. Relationship between installation torque and uplift capacity

Tsuha and Aoki (2010) evaluated the physical relationship between uplift capacity and installation torque of deep helical piles in sand. The theoretical correlation, expressed by Equation 2.15, showed good agreement between predicted and values measured from physical modelling.

$$T = \frac{Q_s d}{2} + \frac{\sum_{i=1}^{n} Q_{hi} d_{ci} tan(\theta_i + \delta_{ri})}{2} \tag{2.15}$$

Where: Q_s = shaft resistance; Q_{hi} = uplift capacity of helix i; $d_{c,i} = \frac{2}{3}\left(\frac{D_i^3 - d^3}{D_i^2 - d^2}\right)$; $\theta_{p,i} = \tan^{-1}\left(\frac{p}{\pi d_{ci}}\right)$; p = helix pitch; $\delta_{r,i}$ = residual interface friction angle between helix material and surrounding sand at the depth of helix i.

Combining equations 2.13 and 2.15 shows that K_t increases with decreasing helical plate diameter, represented by d_{ci}, and shaft diameter, d. According to the authors, this relationship helps explain the influence of pile geometry on K_t values reported in the literature. The residual interface friction angle δ_r also influences K_t. The authors demonstrated that, in cases where δ_{ri} was influenced by the sand friction angle φ, the magnitude of K_t decreases with an increase in φ, in similar piles.

2.7.8. Factor of safety

The ultimate capacity determined through one of the design methods must be divided by an appropriate factor of safety resulting in the allowable design load capacity, Q_a, following Equation 2.16.

$$Q_a = \frac{Q_u}{FS} \tag{2.16}$$

Where: Q_u = ultimate capacity based on theoretical calculation, installation torque correlations, or load tests; and FS = factor of safety.

Factors of safety that range between 1.5 and 3.0 can be used in piles loaded in tension or compression (USACE, 1991). Low factors are used when load tests are performed on a high percentage of helical piles, as is the case of earth retention systems. Higher factors of safety should be used where direct observations of the bearing stratum of each bearing element is limited.

The most used value for factor of safety is 2.0, according to Clemence and Lutenegger (2015). This value can be used when torque correlations are used to verify pile capacity. Perko (2009) found that applying a factor of safety of 2.0 on the results of 112 load tests resulted in a probability of 84 percent that the actual capacity measured in the field will exceed the theoretical prediction.

2.7.9. Pile deflection

Based on years of experience, Perko (2009) affirms the deflection of properly designed and installed piles is on the order of 13 to 25 mm or less under design loads, when installed in soils with a blow count higher than 20.

According to Perko (2009), deflection is affected by mechanical properties of the pile, such as helix pitch, shaft diameter, and shaft thickness, as well as geotechnical conditions of the soil mass where the pile was installed, such as soil layering, effective stress, density, and elasticity. He also affirms, based on several studies, that finite element and discrete element software can help estimating the settlement of a helical pile.

2.7.10. Minimum embedment

Embedment is one of the most important factors influencing the capacity of helical piles. Depending on embedment, failure of helical piles can take place in two different modes. If the top bearing plate is located too close to the surface, shallow failure occurs because the soil above the top helix does not provide enough confinement. Soil mass protruding on the ground surface is an identifier of shallow failure.

To take full advantage of the weight of the soil above the helix for pullout applications, the helical piles must be embedded into the ground to a minimum depth, below which the pile will fail in a deep mode. The complex geometry of the actual failure surface above the top helix is usually simplified into a truncated inverted cone (Ghaly, Hanna and Hanna, 1991). The minimum embedment depth is defined as the height of the truncated cone of soil above the top helix that can provide sufficient weight to hold down the helical pile.

Relative embedment, or depth, ratio is defined as the depth to the shallowest helix by its diameter (H_1/D_1). It is the standard way of referring to embedment in the industry. Experiments performed by Ghaly and Hanna (1992) show that the transition between shallow and deep failure modes is not sudden and a transition between the two occurs for embedment ratios of 7 for loose coarse-grain soil and 11 for dense coarse-grain soil. The same set of experiments showed the critical depth ratios for loose and dense sands are 9 and 14, respectively. Based on the estimates by Perko (2009) for coarse-grain soil, the minimum embedment ratio is 4 for loose soil and 7 for dense soil, for a helical bearing plate with 304 mm in diameter. The minimum embedment depth recommended by Hubbell Power Systems (2014) is five helix diameters

Many authors tried to determine the angle of the pull-out cone to the vertical (θ). Ghaly and Hanna (1992) and Ghaly, Hanna, and Hanna (1991) using the angle of the cone equal to 2/3 times the angle of internal friction of the soil better approximates the results from their experiments. Meyerhof and Adams (1968) found the angle to vary from $\theta = \phi/2$ to $\theta = \phi/4$ for circular footings. Laboratory experiments by Veesaert and Clemence (1977) suggested the cone may be modelled with an angle $\theta = \phi/2$. Murray and Geddes (1987), and Ilamparuthi *et al.* (2002) proposed the same value. Perko (2009) recommends ignoring the side friction and using 45º as the angle of the cone.

2.7.11. Groundwater

The pull-out capacity of helical piles can be significantly affected by the presence of groundwater. Buoyant forces can cut the effective unit weight of soil by half, consequently decreasing the pressure applied on the top of the bearing plates and reducing the pull-out capacity of the helical pile. Perko (2009) suggests the embedment ratio should be increased by 20 % to counter buoyant forces.

The reduced effective stresses in the soil around the pile can decrease their capacity in both compression and tension applications. The ultimate bearing pressure in areas where the depth of the water table fluctuates should be calculated using effective stress analysis.

2.7.12. Structural capacity

The structural capacity of helical piles can be provided by manufacturers or calculated by an engineering professional. The pile must have sufficient structural capacity to resist the pull-out capacity. Evaluation product reports written in accordance with the Acceptance Criteria for Helical Foundation Systems and Devices, developed by the ICC-Evaluation Service (2007), should include a list of the helical foundation systems, devices, and combinations along with proposed structural capacities, as well the calculations of Allowable Stress Design (ASD) and Load and Resistance Factor Design (LRFD) structural capacities.

According to Perko (2009), when considering the capacity of a helical pile, both shaft and helix capacity should be evaluated. The evaluation of shaft capacity should include calculations of gross yielding of the shaft and fracture of any couplings. The evaluation of helix capacity can be done using plate punching analysis or numerical modelling software. The results from these calculations can be used to check the welds between the helix and the shaft. Engineering properties should be computed considering the loss of thickness to long-term corrosion. Laboratory tests can also be used to check the structural capacity of the pile elements.

The structural capacity of helical piles must also consider torsional resistance, since the shaft must resist the torsional load applied to them during installation. According to Perko (2009), most helical piles are manufactured of high-strength carbon steel yield strength, f_y, between 345 to 483 MPa. According to NBR 8800 (ABNT, 2008), the design strength of steel under shearing is given by Equation 2.17.

$$\tau_{y,max} = 0.9 \times 0.6 \times f_y \tag{2.17}$$

Where: $\tau_{y,max}$ = yield shear limit of steel; and f_y = tensile yield strength of steel.

2.8. Axial load testing

2.8.1. Overview

The use of axial load tests is recommended by some engineers to verify the axial capacity and the capacity-to-torque ratio at sites with a large number of helical piles (Perko, 2009).

In this item, the procedures for axial tension load testing and methods for the interpretation of results are described.

There are two categories of axial tension tests: proof load tests and performance tests. Proof load tests are often used in the construction of earth retention systems while the more rigorous performance tests have broader applications, which include use on shoring, tension membrane structures, tall buildings, tie-back retaining walls, and cable guy systems.

According to ASTM D3689 – 07(2013)e1, the distance between the test pile and the reaction device shall be at least five times the pile butt diameter and no less than 2.5 m. This criterion can be waived for deep helical piles. Perko (2009) affirms that practitioners found no effect on the tension capacity caused by reaction supports at ground level when the depth to helix diameter ratio is greater than 5.

2.8.2. Loading procedures

ASTM D3689 – 07(2013)e1 allows six different procedures for tensile load testing of piles. The procedures include quick, maintained load, loading in excess of maintained load, constant time interval, constant rate of uplift, and cyclic loading. According to Perko (2009), the interval between the application of a load and the reaction from the pile is generally short. The quick load test is the most frequently applied test procedure.

A seating, or alignment, load of 5% to 10% of the design load is commonly applied to the helical pile before taking the initial readings. The load helps fastening the shaft couplings and the thread bar transition system (Hubbell Power Systems, 2014).

In the quick test, the load is applied in increments of 5% of the anticipated failure load. Each load increment is added continuously and immediately after the completion of movement readings for the previous load interval. The load is increased until the failure load is reached. The safe structural capacity of the pile should not be exceeded. During each load interval, the load must be kept constant for a time interval of not less than 4 minutes and not more than 15 minutes, and the same interval should be used for all loading increments throughout the test. The load must be removed in five to ten equal decrements, should be kept constant for a time interval between 4 to 5 minutes long, using the same time interval for all unloading decrements. Creep behaviour can be assessed by increasing the time interval for the failure load. Rebound behaviour can be assessed by doing the same for the final zero load. This test is preferred by contractors, because it can be completed in a few hours as opposed to several days for the maintained and cyclic load test procedures.

2.8.3. Interpretation of results

Several methods can be used for interpreting the capacity of a pile obtained from an axial load test. According to Perko (2009), the basic definition of ultimate capacity is the highest load that can be applied to a pile until deflection continues without application of additional loads. This definition is based just on strength but there are structures that can be damaged if movements are not limited. This is why many interpretation methods are based on deflection.

In deflection methods, the capacity is defined as the load at a predefined amount of deflection. The historic method, based on a suggestion from Terzaghi (1943), limits the pile movement to 10 percent of the pile diameter. It was one of the first criterion to be ever proposed and is still accepted in engineering practice. In this method, the ultimate load is located within the nonlinear region of the load-displacement curve. The design load of the pile will be located within the linear region of the curve after applying an appropriate factor of safety (Abdelghany and El Naggar, 2010).

Local building codes may limit the maximum deflection, with values between 20 mm to 40 mm. Engineering professionals may choose to limit the deflection at the design load based on the sensitivity of the structure, desired rigidity of the foundation, and local experience, with typical values ranging from 10 mm to 25 mm.

In tests made in conformance with the 2015 International Building Code (ICC, 2014), the ultimate load capacity shall be assessed by one of the following methods:

- Davisson Offset Limit
- Brinch-Hansen 90% Criterion
- Butler-Hoy Criterion
- Other methods approved by building official.

The ultimate pile load in the Davisson Offset Limit method (Davisson, 1972) is defined as the intersection of the pile load-deflection curve with an elastic line for a fixed-base, free standing column offset by 3.8 mm plus the pile diameter divided by 120.

The elastic line of deformation of a fixed-end, free-standing, frictionless pile can be obtained by using Equation 2.18.

$$\delta = \frac{Pz}{A_g E} \tag{2.18}$$

Where: δ = deflection; P = load applied to the pile; z = length of the pile shaft; A_g = gross cross-sectional area of the pile shaft; and E = modulus of elasticity of the shaft steel.

According to Perko (2009), a modified version of the Davisson Offset Limit method is recommended by the ICC-ES (2007). This version defines the maximum load capacity as the one achieved when plunging of the helical pile occurs or when net deflection exceeds 10 percent of the helix plate diameter, whichever occurs first. Net deflection is calculated by subtracting the elastic deformation of the pile from the total deflection. For multi-helix configurations, the average helix plate diameter shall be used. This method may result in unreasonable values when applied to large-diameter helical bearing plates. In these cases, it is recommended to limit the deflection under design loads.

The 2015 International Building Code (ICC, 2014) defines ultimate pile capacity as two times the allowable design load. Perlow Jr. (2011) evaluated 75 helical pile test loads and proposed defining the allowable pile design load upon a maximum allowable displacement criterion of 6.4 mm to 8.4 mm. The ultimate pile capacity yielded by this method corresponds to displacements equal to 10% to 12% of the shaft diameter and/or 5% of the average helix diameter.

The Brinch-Hansen 90% criterion (Brinch-Hansen, 1963) defines the failure load as the load associated with four times the movement of the pile head as obtained for 90% of the load. The ultimate capacity is found graphically through trial and error.

In the Butler-Hoy criterion (Butler and Hoyt, 1977), the ultimate pile load capacity is determined by drawing a line tangent to the initial portion of the load-deflection curve and drawing another line tangent to the plunging portion of the curve with a slope of 0.05 in. of deflection per ton (0.143 mm/kN). The intersection of the two lines represents the ultimate capacity of the pile.

Livneh and El Naggar (2008) investigated the axial performance of helical piles using the results from 19 full-scale load tests in different soils and numerical modelling using FEM. They proposed the ultimate load criterion of helical piles be defined as the load corresponding to a pile head movement of a net displacement equal to 8 percent of the largest helix diameter.

When testing high capacity piles with large diameter helical plates (762-1016 mm), Sakr (2010) defined ultimate capacity as the load level that produced a displacement equal to 5% of the diameter of the largest helix.

A survey commissioned by the Helical Piles and Tiebacks Committee and published by Clemence and Lutenegger (2014) found that most practitioners interpret the load-deflection curve using methods traditionally used for other types of deep foundations. The Davisson Offset Limit method is the most frequently used followed by other methods based on maximum limit deflection. Deflection methods typically define the ultimate capacity as the load at 10% of net or gross movement of the largest helix diameter or the average helix diameter.

2.9. Cyclic Behaviour of Helical Piles

2.9.1. Overview

Helical anchors are used as foundation solutions for many structures where the tensile loads fluctuate due to natural factors such as wind, wave, or tide action (Hanna, 1978). These loads can be called "cyclic" when they exhibit clearly repeated patterns and their amplitude and return period are regular (Andersen *et al.*, 2013). Traffic, plant operations and rotating machinery are other sources of cyclic loads. Common examples of structures subjected to cyclic loads are guyed cable foundations used for wind towers, communication towers, and power transmission poles. The wind acting on these structures results in variable cyclic load on the anchors. Safe operation of these structures depends on their ability to resist cyclic loading (Tsuha *et al.*, 2012b).

According to Andersen *et al.* (2013), most natural cyclic load events actually have irregular amplitude waves distributed randomly over time. However, it is common to study these phenomena using cyclic field, laboratory-model, and soil-element tests with load or displacement series with fixed frequency and regular amplitude. These tests can be defined by their number of cycles (N), cycle period (T) (or frequency of cycles, f), average load (Q_{mean}), and cyclic amplitude (Q_{cyclic}), as defined in Figure 2.8. Chan and Hanna (1980) observed that beyond these properties, the cyclic response of displacement piles in sand is also affected by pile depth (L), loading history, and sand characteristics.

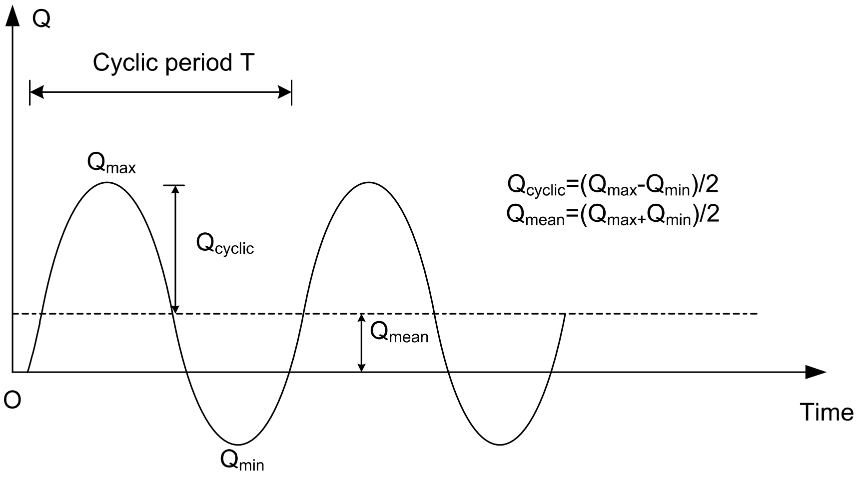

Figure 2.8 – Definition of cyclic loading parameters for both field and laboratory model tests (Tsuha *et al.*, 2012b)

The characteristics of common cyclic loading events are illustrated in Figure 2.9.

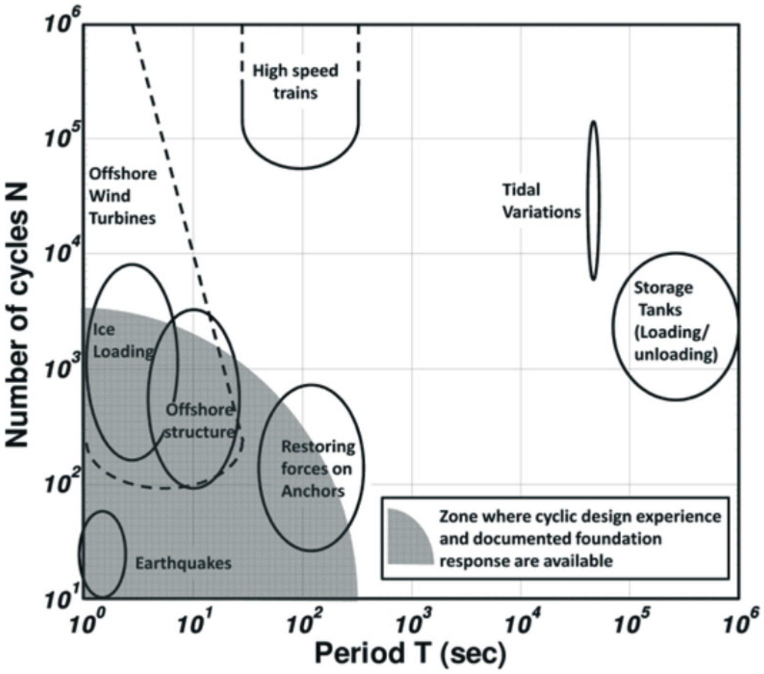

Figure 2.9 – Periods and number of cycles characterizing typical cyclic loading events (Andersen *et al.*, 2013).

According to Wichtmann (2005), when load cycles are applied with low frequency, the inertia forces are low and can be neglected and the nature of the load is considered quasi-static. When the frequency is increased, and the inertia have to be considered, the load is called dynamic. The limit between the two behaviours also depends on the amplitude of the applied loading but this parameter is often ignored, and the limit frequency is assumed to be 5 Hz.

A cyclic loading is considered symmetrical when the average load is equal to zero. Non-symmetrical loads are more common than symmetrical loads. Non-symmetrical loadings are grouped according to the loading direction. One-way (OW) loading is applied either in compression or tension, and $Q_{cyclic} < Q_{mean}$. Compression and tension are applied alternately in two-way (TW) loading, and $Q_{cyclic} > Q_{mean}$ (Andersen *et al.*, 2013; Schiavon, 2016).

2.9.2. Effects of cyclic loads on pile behaviour

Repeated cyclic loads can cause changes in the uplift capacity of piles, as observed by Turner and Kulhawy (1990), Airey *et al.* (1992), Jardine and Standing (2000). According to Andersen *et al.* (2013), the capacity of a pile after receiving high-level cycles is smaller than the monotonic capacity, while the application of low-level cycles can improve the capacity of the pile.

Degradation of the shaft capacity, due to skin friction, of conventional (non-helical) piles subjected to cyclic loading has been observed in the field (Poulos, 1989; Turner and Kulhway, 1990) and replicated in laboratory (Fioravante, 2002). DeJong *et al.* (2003) attribute cyclic degradation in sands to a decrease in the normal stress due to cumulative contraction of the soil within the shear zone contacting the interface. Chan and Hanna (1980) reported failure under one-way loading for a maximum load (Q_{max}) equal to 30% of the ultimate static capacity. Gudehus and Hettler (1981) defined failure as the increasing accumulation of permanent displacements with increasing number of cycles. They found that loads as small as 10% of the ultimate capacity can result in failure and higher load levels reduce the number of cycles before failure.

On helical piles, cyclic loadings have been observed to cause degradation and improvement of the anchor capacity. Clemence and Smithling (1984) observed increases in load capacity caused by stiffening of the soil-anchor system after the application of cyclic loadings. Victor and Cerato (2008) suggest that the diverging results may be explained by how much the soil was disturbed during the installation process.

The study of foundation systems subjected to cyclic loads must include not only its capacity but also its displacements over time. Poulos (1989) associated cyclic axial failure of conventional piles with two mechanisms: cyclic degradation of shaft skin friction and base resistance, expected to dominate under two-way loading; and accumulation of permanent displacements with increasing load cycles, expected to dominate under one-way loading. Van

Weele (1979) attributed displacement accumulation to continuous rearrangement and possible crushing of particles.

The movement of loaded anchors over time is called creep. Ghaly and Clemence (1998) report that cyclic loads below 25 percent of the ultimate static resistance results in almost no plastic upward creep. Based on this, Perko (2009) recommends that service loads on helical anchors subjected to cyclical loading should be limited to 25 percent of the ultimate capacity.

2.9.3. Stability of foundations under cyclic loading

Tsuha *et al.* (2012b) subjected instrumented piles in sand to cyclic tension axial loads and used displacement rates and number of cycles performed before failure to classify the pile behaviour. For these experiments, cyclic failure was assumed to be reached for an accumulated displacement of 10% of the pile diameter, or the displacement rate per cycle showed a sharp increase.

The main parameters that influence the number of load cycles a pile can sustain before failure are the mean cyclic load, the cyclic load amplitude, and the shaft and base resistances (Schiavon, 2016). According to Puech et at. (2013), cyclic response analyses of piles can be represented synthetically based on their combinations of mean and cyclic load through the use of cyclic interaction (or stability) diagrams. The concept of cyclic diagrams was introduced by Karlsrud *et al.* (1986) for clays and by Poulos (1988) for sands.

The generic diagram proposed by Poulos (1988) is shown in Figure 2.10. The diagram is based on the static compressive capacity, Q_C, static tensile capacity, Q_T, and the parameters P_a and P_c, equivalent to Q_{mean} and Q_{cyciic}, respectively, previously defined. Three main regions can be identified in the diagram: (1) a cyclic stable region A in which cyclic loading has no influence on the axial capacity of the pile; (2) a cyclically metastable region B in which cyclic loading causes some reduction of axial load capacity, but the pile does not fail within a specified number of cycles; and (3) a cyclically unstable zone C in which cyclic loading causes sufficient reduction of axial capacity for the pile to fail within a specified number of cycles of load.

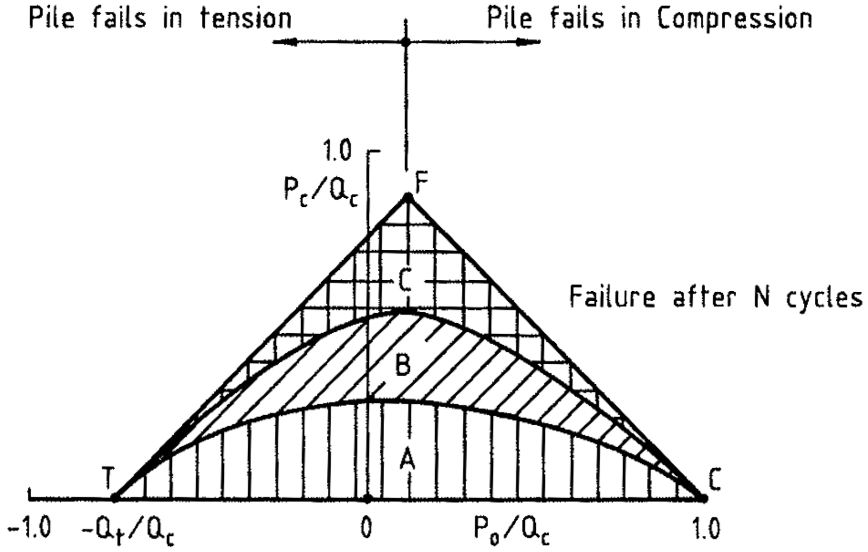

Figure 2.10 – Main features of a cyclic stability diagram (Poulos, 1988).

Tsuha *et al.* (2012b) recommend a quantitative definition of stability zones, associating them with the displacement accumulation rates. The three response classes that were established are described below and illustrated in Figure 2.11 for piles in tension applications. Displacement rates were considered slow when accumulated displacement was less than 1 mm per 10^4 cycles. Rates equal or above 1 mm per 10^2 cycles were considered fast. The defined zones include:

- A Stable (S) Zone, where axial permanent displacements stabilize or accumulate very slowly over hundreds of cycles, under either two-way or one-way loading, with potential increases in shaft capacity. Failure occurs after 1000 cycles.
- An Unstable (US) Zone, where displacements accumulate rapidly under OW or TW cycling, with noticeable decreases in shaft capacity. Shaft failure occurs in less than 100 cycles.
- An intermediate Meta-Stable (MS) Zone, where displacements accumulate at moderate rates over tens of cycles without stabilizing. Failure occurs between 100 and 1000 cycles.

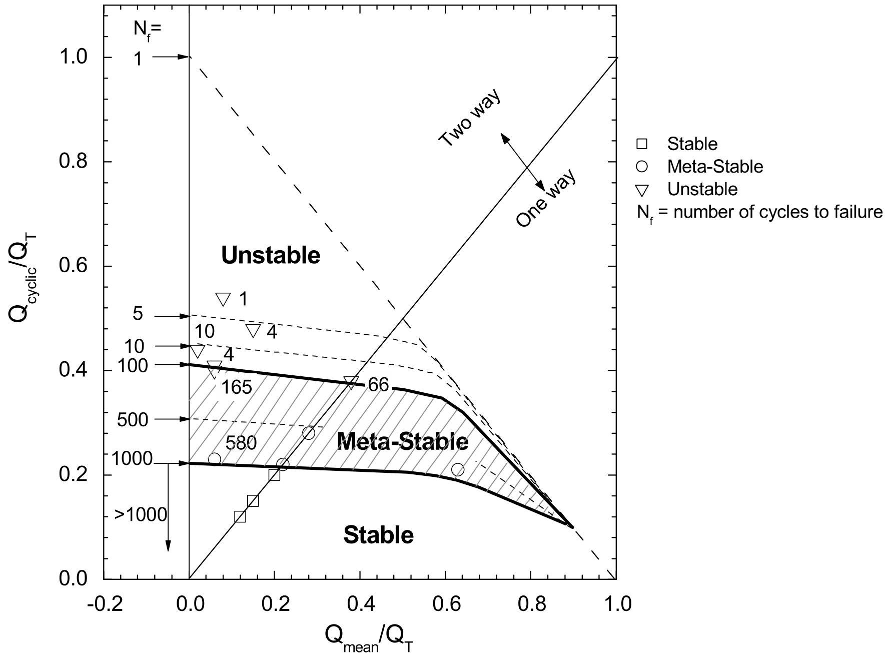

Figure 2.11 – Summary of average cyclic shaft loading and failure conditions in Mini-ICP tests, showing tentative Stable, Meta-Stable and Unstable Zone boundaries (Tsuha *et al.*, 2012b).

According to Schiavon (2016), the estimation of the number of cycles a foundation can sustain before failure is important to establish the interval between adjustments of the prestressing load in a guy-cable. The author observed two different trends in the accumulation of displacements according to the combination of cyclic parameters, as shown in Figure 2.12. Two equations, 2.19 and 2.20, were proposed to estimate the accumulated displacements in the 0-1 and 1-2 segments, respectively. A third equation, (2.21), was proposed to estimate the number of cycles where the transition between the two behaviours occurs. The equations also can be used to generate interaction diagrams, as shown in Figure 2.13.

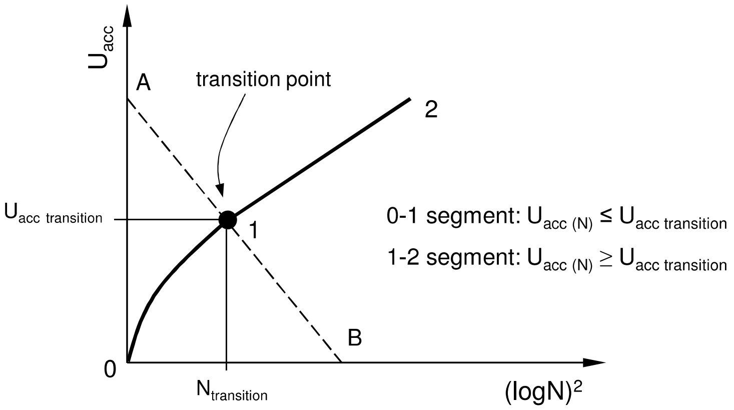

Figure 2.12 – Two different trends in displacement accumulation (Schiavon, 2016).

$$U_{acc(N)} = \frac{10\times\frac{Q_{cyclic}}{Q_T}\times(\log N)^{2.5}}{2+\frac{Q_{max}}{Q_T}} + U_{acc(N=1)} \qquad \text{for} \qquad U_{acc(N)} \leq U_{acc,transition} \tag{2.19}$$

$$U_{acc(N)} = \frac{20\times\frac{Q_{cyclic}}{Q_T}\times[\log(N-N_{transition})]^{1.5}}{2-\frac{Q_{max}}{Q_T}} + U_{acc,onset} \quad \text{for} \quad U_{acc(N)} > U_{acc,transition} \tag{2.20}$$

$$U_{acc,transition} = \frac{1.29Q_{mean}-3.67Q_{cyclic}}{Q_T} - 6.78(\log N_{transition})^2 + 30.36 \tag{2.21}$$

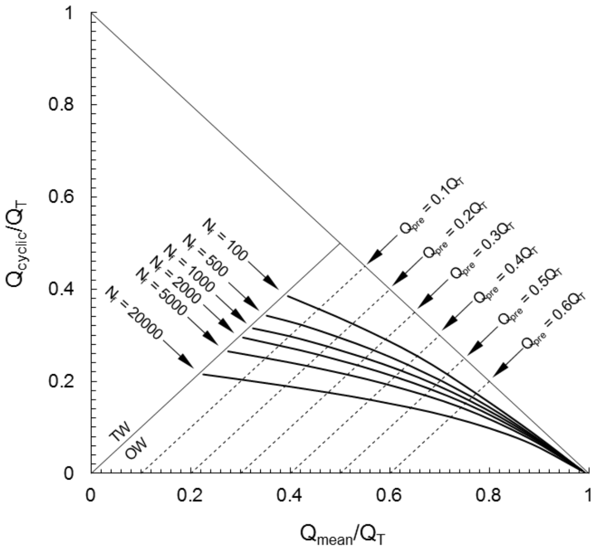

Figure 2.13 – Isovalues lines of cycles to cause a limiting accumulated displacement of 10%*D* (Schiavon, 2016).

Foundations also behave differently when subjected to cyclic loading sequences with different loading parameters. This effect has been studied by Wichtmann (2005), Blanc and Thorel (2016) and Schiavon (2016). Wichtmann (2005) observed that performing high amplitude cycles in triaxial tests diminish the effects of subsequent cycles with lower amplitude.

Blanc and Thorel (2016) assessed the cyclic axial behaviour of piles driven in sand using centrifuge tests. The results are shown in Figure 2.14. The author found that piles previously subjected to low amplitude loads fail earlier than piles subjected only to high amplitude loads, and that piles previously subjected to high amplitude loads don’t fail, in a similar way to piles subjected to low amplitude loads only.

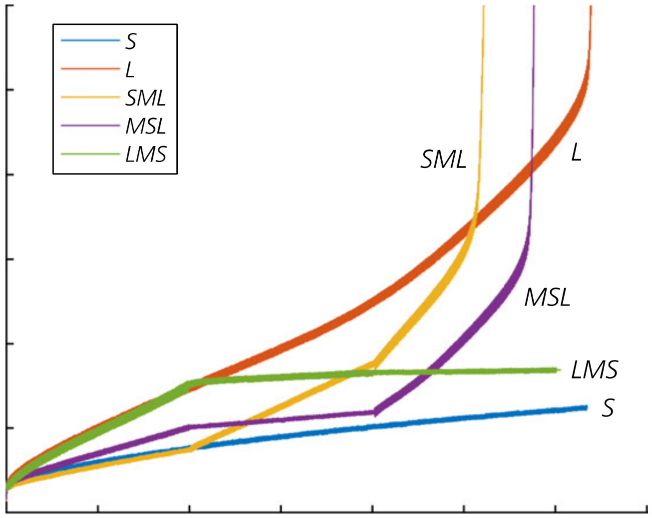

Test	Cyclic amplitude	*S*	*M*	*L*
SML	Q_a/Q_{ut}	0·34	0·34	0·34
	Q_{cy}/Q_{ut}	0·23	0·30	0·35
	w_{200}/B: %	−6·0	−10·3	($N_f = 110$)
MSL	Q_a/Q_{ut}	0·35	0·35	0·35
	Q_{cy}/Q_{ut}	0·23	0·29	0·35
	w_{200}/B: %	−1·8	−8·5	($N_f = 170$)
LMS	Q_a/Q_{ut}	0·34	0·34	0·34
	Q_{cy}/Q_{ut}	0·27	0·32	0·38
	w_{200}/B: %	−0·3	−1·5	−12·3

Figure 2.14 – Cyclic loading tests: normalized settlement (w/B) against number of cycles (Blanc and Thorel, 2016).

Schiavon (2016) performed cyclic load tests in centrifuge models and observed that low amplitude loads following medium amplitude loads cause accumulated displacements 42% smaller than when the inverse loading sequence is applied. In another series of tests, medium and high amplitude loads were used, and it was observed that applying the high amplitude load before the medium amplitude load resulted in larger accumulated displacements than in the inverse sequence. The results are shown in Figure 2.15.

Schiavon (2016) also used instrumented single-helix anchors to carry out field tests. The author performed static load tests before and after performing cyclic load tests. The application of a single, large amplitude load cycle improved the soil above the helical plate and eliminated the accumulated cyclic displacements. However, the cyclic loading did not influence the overall post-cyclic response, but caused changes the distribution of loads between shaft and anchor.

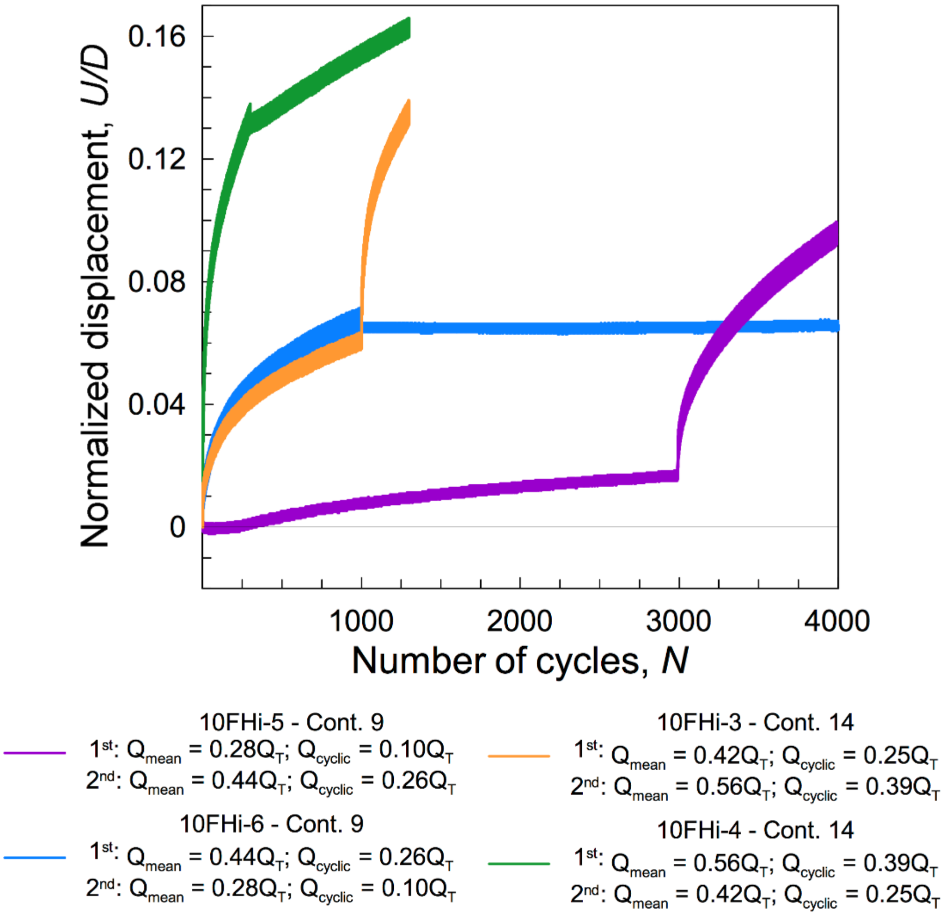

Figure 2.15 – Anchor head vertical displacements of tests with sequences of cyclic loadings (Schiavon, 2016).

2.9.4. Degradation of strength elements due to cyclic loading

According to Poulos (1989), the analysis of cyclic axial pile response must include the degradation of skin friction, base resistance, and soil modulus. He found that the degradation of skin friction in cyclic axial loading is related to amplitude of cyclic displacement, number of cycles, soil type, and the type of pile. He observed that skin friction degradation increases as amplitude of cyclic displacement increases, and displacements of about 0.5 mm can result in significant degradation of the skin friction. He proposed assuming cyclic degradation of base resistance can be ignored in the absence of data showing relationships between base resistance and cyclic loads. His experiments did not show significant degradation of soil modulus after cyclic loads.

Urabe *et al.* (2015) performed vertical loading tests on straight and wing (anchor) piles placed in a centrifuge box and filled with air-pluviated sand. Shaft friction reached its maximum value at a displacement between 6% to 13% of the shaft diameter in monotonic loading tests and decreased gradually with increasing displacements. In cyclic loading tests, maximum shaft friction was observed at displacements between 3% to 6% of the shaft diameter, decreasing significantly with increasing displacements. Shaft friction decreases due to cyclic loads were higher in tension tests than in compression tests. A possible explanation offered by the authors is that pushing the pile resulted in shear deformation that increased the effective stress in the soil around the pile, while pulling the pile reduced the effective stress around the pile. It was also observed that after shaft friction reached its ultimate value, at a displacement of about 30 mm, the anchor was the main element resisting the vertical load. In displacement-controlled axial load cycling.

Schiavon (2016) concluded that the behaviour of helical anchors under cyclic loads is heavily influenced by helix bearing resistance, which functions as the pile base resistance of regular piles. The author analysed the results from instrumented helical anchors subjected to cyclic loading and noticed that skin friction degradation occurred in all cyclic loading tests and that the shaft resistance at the end of cyclic loading was negligible. The instrumentation also revealed that the helical anchor resisted between 70 to 97 percent of the load applied in the first cycles, reaching 92 to 97 percent of the maximum applied load in the last cycle. The author also concluded that shaft resistance is not fully mobilized in one-way tensile loading with low values of Q_{mean} and Q_{cyclic}. The shaft resistance is only fully mobilized and exhibits degradation in early cycles in loadings with higher cyclic amplitudes.

Chow *et al.* (2015) performed monotonic and cyclic load tests in plate anchors installed in dry dense sand and observed that both types of testing have similar load-displacement behaviour. However, cyclic loads with relatively low magnitude resulted in increases in the eventual ultimate capacity of the anchors, as a result of soil densification. This phenomenon was not observed with magnitudes approaching the monotonic capacity.

El Sharnouby and El Naggar (2011) performed tests on reinforced helical pulldown micropiles and found that ultimate capacity improved after applying 15 one-way load cycles, each cycle applied over 2 minutes, with average and maximum load of 40% and 54% of the ultimate capacity, respectively.

Cerato and Victor (2009) found that cyclic loads applied at a frequency of 3-5 Hz may increase the ultimate capacity of anchors when the cyclic load/static capacity ratio is between 0.25 to 0.40.

Abdelghany and El Naggar (2010) performed tests on helical piles and observed that plain and grouted piles exhibited reductions in ultimate capacity between 5% to 10% after 15 load cycles, while grouted piles reinforced with steel fibres presented minimal reduction in axial capacity after cycling.

Schiavon (2016) carried out physical modelling in centrifuge on helical anchor models installed in dry sand. Cyclic loading did not affected helix bearing capacity even with large accumulated displacements after 1000 cycles, but shaft resistance degradation was observed during the first 100 cycles. In some cases, after 1000 cycles, post-cyclic degradation was observed even with the accumulated displacements below 10%D. The author also performed static load tests after the application of cyclic loading. Piles with accumulated displacements greater than 10% D and up to 400 cycles were more likely to display increased post-cyclic capacity. Increases in post-cyclic uplift capacity were observed in the piles previously subjected to a maintained Q_{mean} of around 50% of Q_T and a Q_{max} greater than 80%Q_T. Equation 2.22 was proposed to estimate the post-cyclic helix bearing capacity factor ($N_{q,pc}$) and is valid for the tested interval of 0.4 < Q_{mean}/Q_T < 0.7.

$$\frac{N_{q,pc}}{N_q} = -0.433\left(\frac{N}{100}\right) - 0.236\left(\frac{1}{Q_{mean}}\right)^2 + 0.285\left(\frac{1}{Q_{cyclic}}\right)^2 + 98 \qquad (2.22)$$

Schiavon (2016) also analysed the post-cyclic behaviour using an interaction diagram. He concluded that most of the piles that exhibited post-cyclic increases in capacity were subjected to high Q_{mean} and Q_{cyclic} corresponding to the Meta-Stable and Unstable zones, as shown in Figure 2.16.

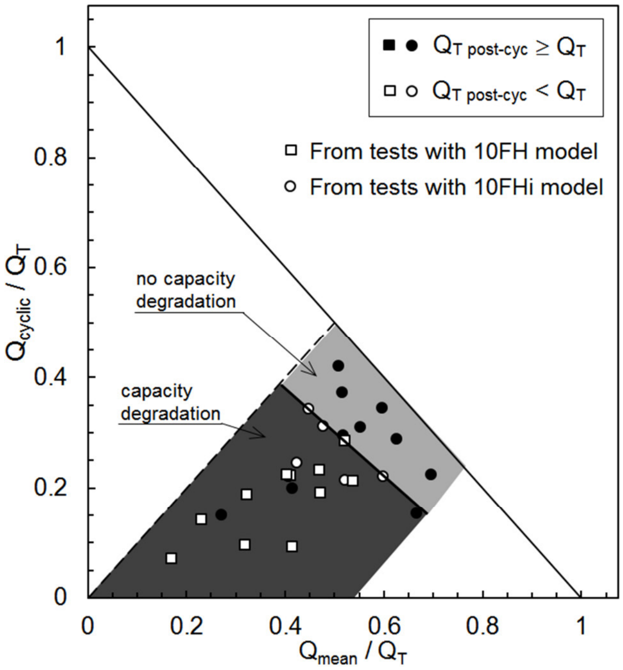

Figure 2.16 – Post-cyclic capacity interaction diagram (Schiavon, 2016).

3. MATERIALS AND METHODS

This chapter presents the procedures used to design the pile prototype used in the present research and the materials and methods followed to install and evaluate the behaviour of steel helical piles subjected to static and quasi-static cyclic tensile loading. A prototype was manufactured and tested in a construction site. Soil samples were collected from the study area and shipped to the laboratory to have geotechnical properties assessed. The results of the pull-out load tests with the helical piles in the field along with the results of the laboratory tests were used to calibrate numerical models of helical pile load tests. A series of parametric investigations was performed based on the calibrated models.

The next items present the site where the research took place, the local geology, the geotechnical parameters obtained from soil samples collected in the area, a description of the load tests performed and the characteristics of the numerical study developed according to the field results.

3.1. Experimental site

The experiments in this work were performed in a construction site within the main Campus of the Federal University of Rio Grande do Norte (UFRN), at Natal, Brazil. The location of the construction site in the Campus is shown in Figure 3.1a.

The location of the tests is shown in Figure 3.1b. The southernmost corner of the construction site was used as a reference point and its coordinates in the UTM system are also shown in the figure.

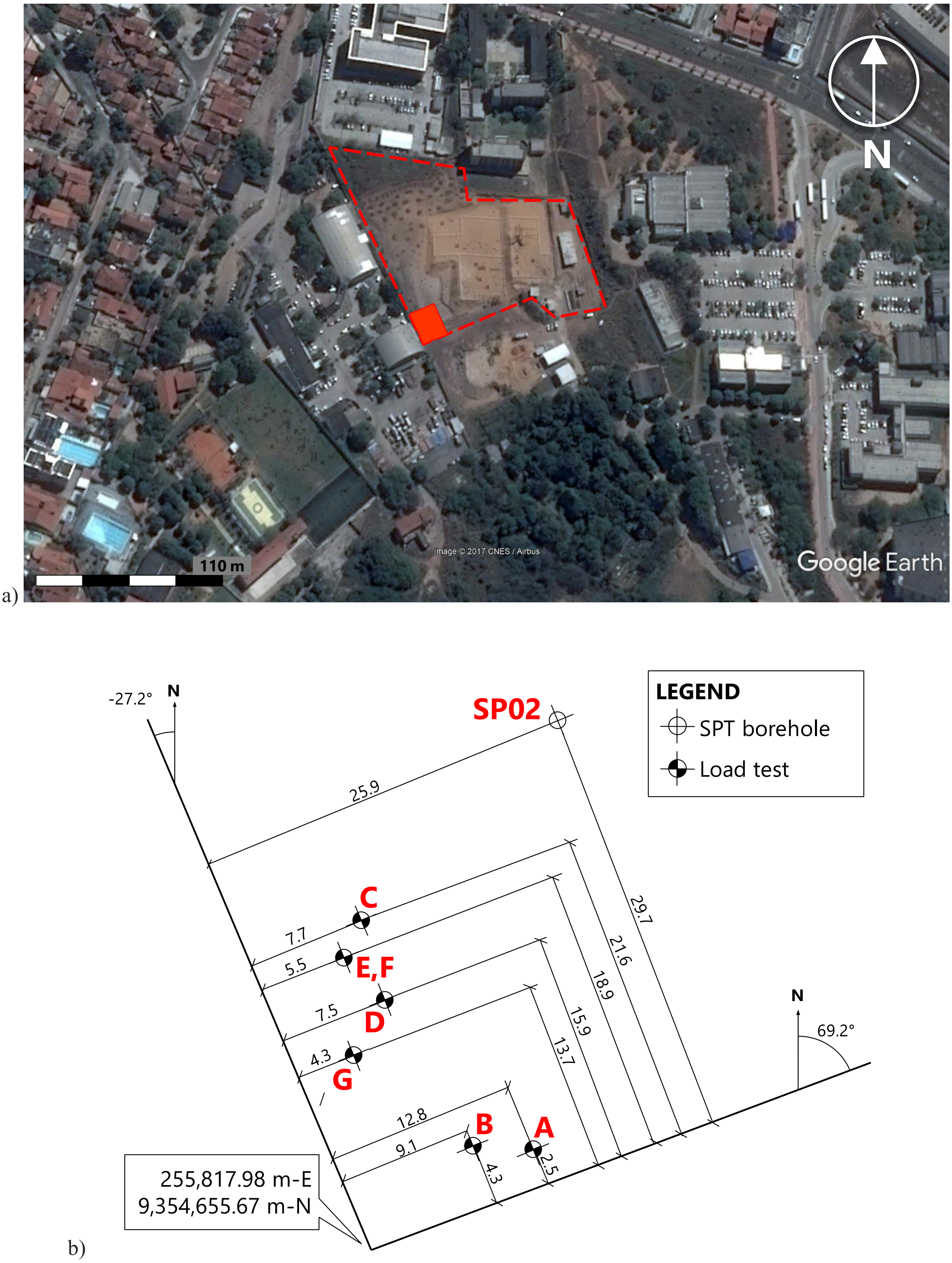

Figure 3.1 – a) Location of the study area inside the construction site (adapted from Google Earth, 24/02/2017); b) Location of the tests and the SPT borehole.

A view of the research site (highlighted in red) before the beginning of the tests is shown in Figure 3.2.

Figure 3.2 – Research site (in red) before the start of construction.

3.2. Site geology

Rio Grande do Norte’s eastern coast, where Natal is located, is covered exclusively by deposits of sedimentary origin. Sediments from the Tertiary and Quaternary periods can be found in the region. Tertiary sediments are represented by the “Barreiras Formation”, a chain of sediments showing little or no consolidation, with assorted colours and different lithofacies ranging from clay to conglomerates. In Rio Grande do Norte, the Barreiras Formation covers the surface of plateaus. Deposits of sediments from the Quaternary Age, originated from wind, river, swamps or beaches, lie above the Barreiras Formation. (Santos Jr. and Chaves, 2005).

The main campus of UFRN, like most of the city of Natal, lies above fields of old Aeolian dunes, also termed Paleodunes, formed between Late Pleistocene and Holocene Ages. The dune materials laying above the Barreiras Formation are composed of fine to medium uniform quartz sands with mafic minerals and round to sub-angular grains (Nogueira, 1981; Jesus, 2002; Silva 2002; Moreira *et al.*, 2014).

3.3. Geotechnical characteristics of the research site

3.3.1. Field tests

3.3.1.1. Soil survey from Standard Penetration Tests

The field survey program in the construction site was composed of thirteen standard penetration tests (SPT), performed according to the recommendations of Brazilian Standard NBR 6484, which is in line with ASTM D 1586 – 11. The soil profile and the N_{SPT} blow count obtained from borehole SP02 are shown in Figure 3.3. N_{SPT} values are for an assumed efficiency of 72%. As shown in Figure 3.1, SP02 is the closest borehole to the tests performed for this investigation, and is similar to the other profiles obtained in the survey program. The ground water table was not detected in the field survey.

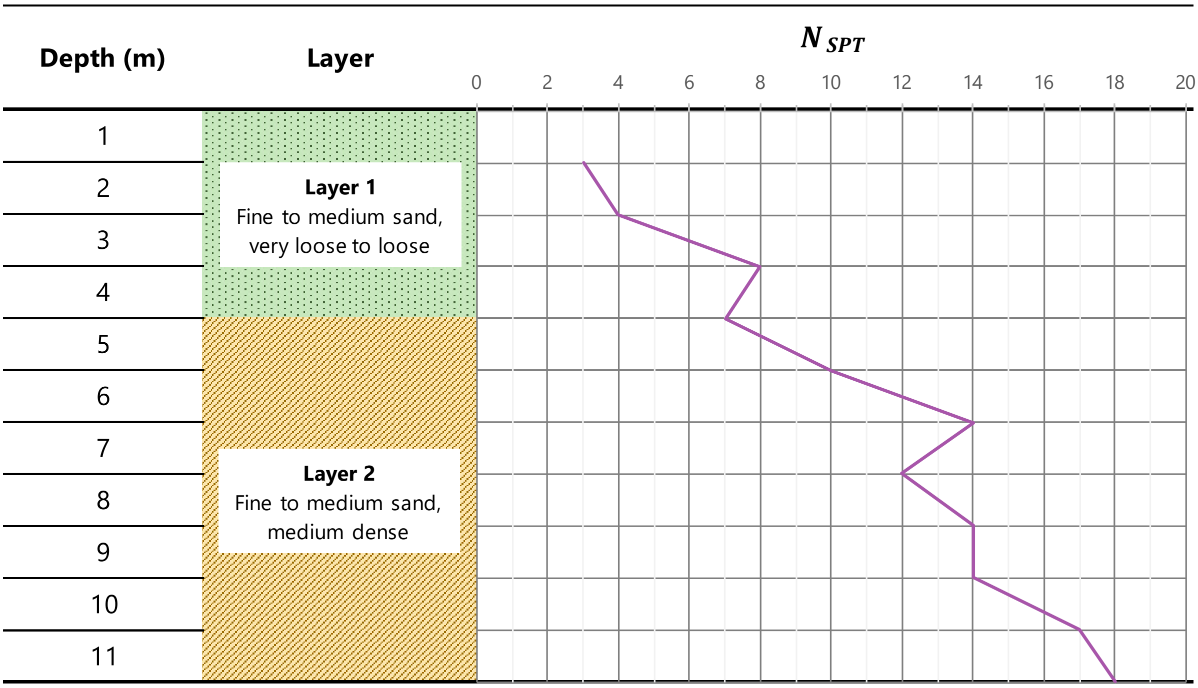

Figure 3.3 – Soil profile obtained from borehole SP02.

After performing the load tests in the field, excavation services were executed in the area, and it was possible to confirm that the profile obtained from borehole SP02 is representative of the subsoil of the entire testing area. The presence of organic matter and demolition debris in the first half meter of the superficial layer was also observed (Figure 3.4).

Figure 3.4 – Side view from a cut performed after completion of the pile load testing program.

3.3.1.2. In-situ unit weight and water content

Two pits with 1 m of depth were excavated in different locations within the area where the pull-out tests were conducted, as shown in Figure 3.5. Samples were collected with a DER P-208 sampler from the bottom of the pit using the procedures from NBR 9813 (2016) and were shipped to the laboratory, in order to determine the soil natural unit weight and water content. The samples were also used for geotechnical characterization and strength tests. The mean dry unit weight from the samples was 14.7 kN/m^3 and the mean water content was 4.3%.

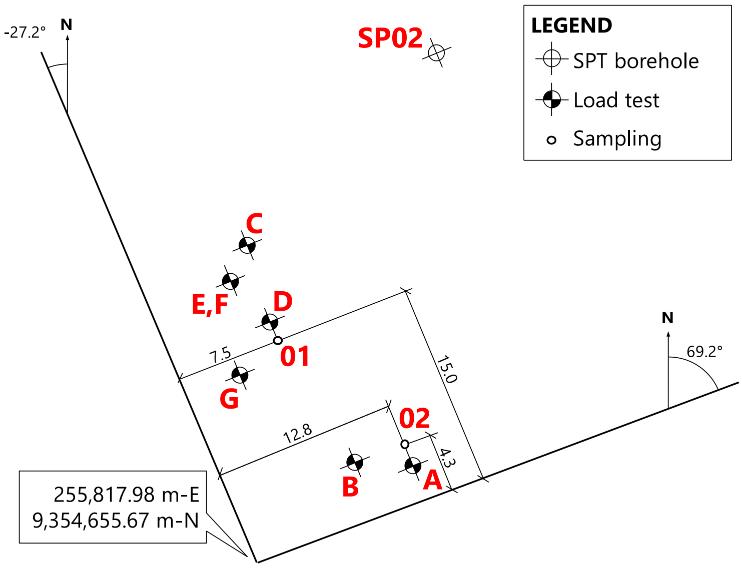

Figure 3.5 – Location of the sample collections.

3.3.2. Laboratory tests

3.3.2.1. Particle size analysis

Samples from the field were subjected to particle size analysis following Brazilian standard NBR 7181 (ABNT, 1984). The obtained grain size distribution curves are shown in Figure 3.6. The corresponding soil fractions according to NBR 6502 (ABNT, 1995) are shown in Table 3.1. Grain contents smaller than 0.075 mm are below 5%.

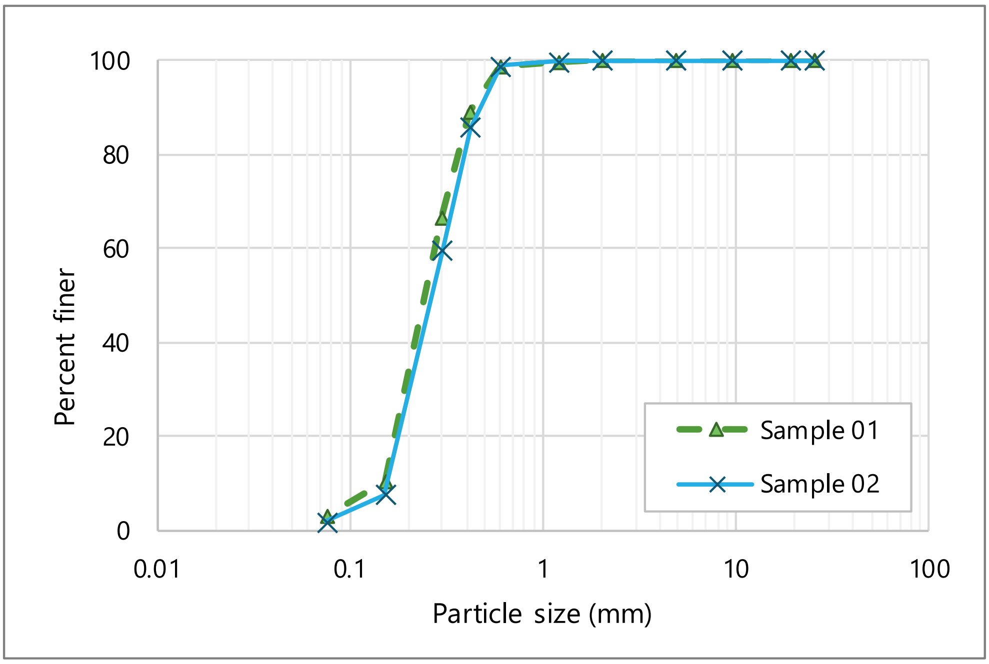

Figure 3.6 – Grain size distribution curves.

Table 3.1 – Soil fractions according to NBR 6502 classification

	Percentage	
Name of soil separate	**Sample 01**	**Sample 02**
Clay	0.00	0.00
Silt	0.00	0.00
Fine sand	29.36	25.10
Medium sand	69.57	73.89
Coarse sand	1.07	1.01
Gravel	0.00	0.00

The soil is classified as a poorly graded sand (SP), according to the Unified Soil Classification System (USCS). The coefficient of uniformity and the coefficient of curvature calculated from the grain size distribution curves are 1.96 and 0.99, respectively.

3.3.2.2. Specific gravity of soil solids

The specific gravity of the soil was determined following the procedures of NBR 6508 (ABNT, 1984). The mean value of G_s was 2.63.

3.3.2.3. Maximum index density and minimum index density

The maximum and minimum void ratios for each sample were determined following the NBR 12004 (ABNT, 1990) and NBR 12051 (ABNT, 1991), respectively. The results are shown in Table 3.2, along with the values of dry unit weight and relative density.

Table 3.2 – Minimum and maximum relative density

Property	**Sample 01**	**Sample 02**
Minimum void ratio	0.61	0.66
Maximum dry unit weight (kN/m³)	16.0	15.4
Maximum void ratio	0.85	0.85
Minimum dry unit weight (kN/m³)	13.9	13.9
In-situ unit weight (kN/m³)	15.3	14.4
In-situ void ratio	0.68	0.79
In-situ relative density	71%	34%

3.3.2.4. Direct shear tests

Direct shear tests were used to determine the internal friction angle of samples 01 and 02. The samples were compacted to the same unit weight observed in-situ: sample 01 with a relative density of 71% and sample 02 relative density of 34%. The tests were performed according to ASTM D3080M – 11. Series with four specimens were tested for each sample. The specimens were tested inside a shear box consisting of two parallel platens of square cross-section with 60 mm sides. The soil was poured into the shear box and vibrated until the specimen reached the required volume. In each test, a vertical load was applied at the top of the specimen and kept constant. Three normal loads were used to apply target normal stresses of

50, 100 and 200 kPa. The shearing rate was kept constant at a rate of 0.7 mm/min. Each test was finished after the horizontal displacement of the lower platen reached 10% of the cross-section size, i.e., 6 mm. Horizontal and vertical displacements were recorded using dial gauges installed in the shearing apparatus. The shear force was measured using a proving ring. Readings from the three gauges were collected at one-minute intervals.

The internal friction angles of the samples 01 and 02 were 36º and 32º, respectively. The graphs for shear stress versus horizontal displacement, volumetric changes versus horizontal displacement, and shear stress versus normal stresses for sample 02 are shown in Figures 3.7 to 3.9. Similarly, results for the samples 03 is shown in Figures 3.10 to 3.12.

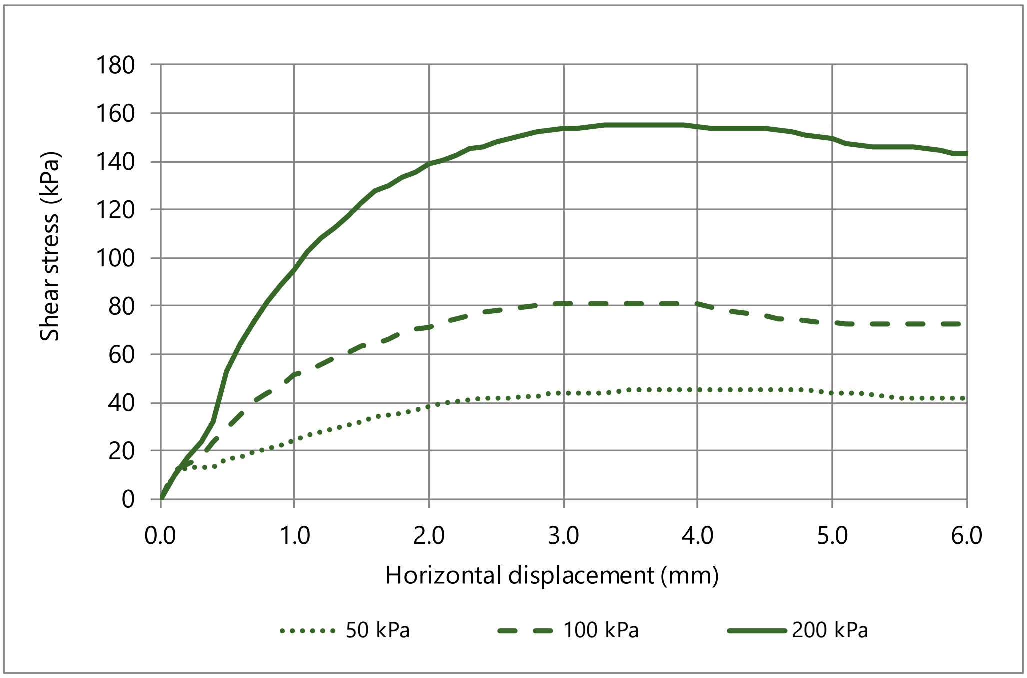

Figure 3.7 – Direct shear test results with sample 01: deviatoric stress x horizontal displacement.

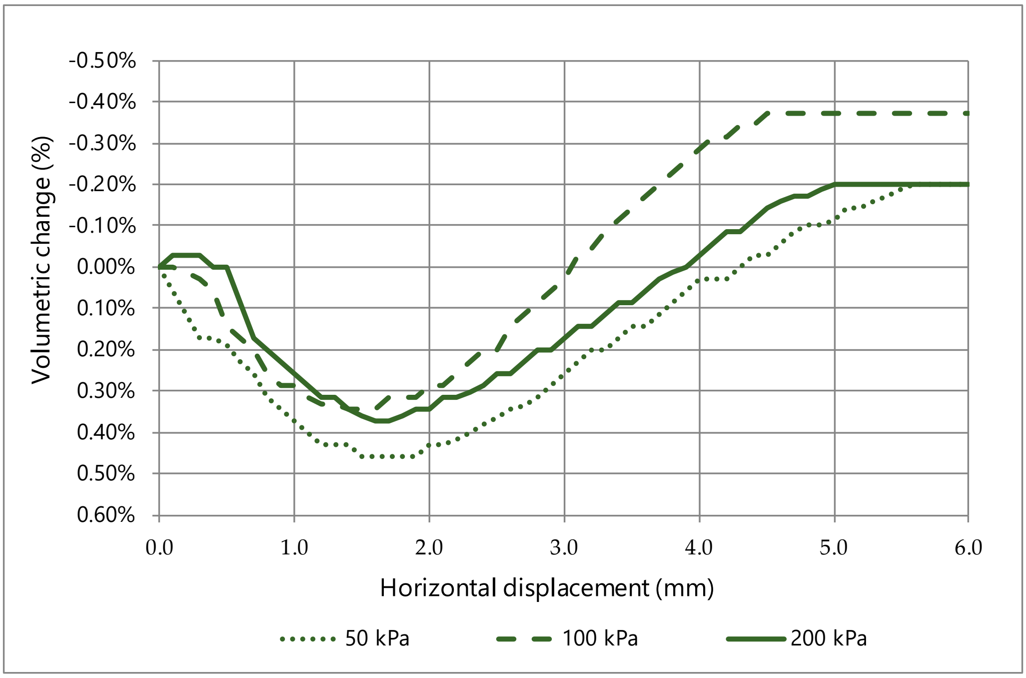

Figure 3.8 – Direct shear test results with sample 01: volumetric change x horizontal displacement.

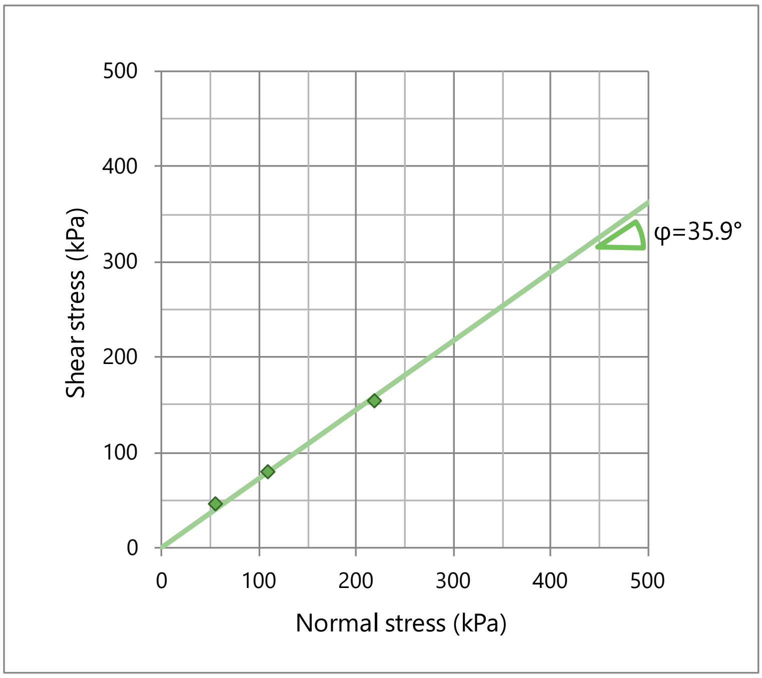

Figure 3.9 – Direct shear test results with sample 01: Mohr-Coulomb failure envelope.

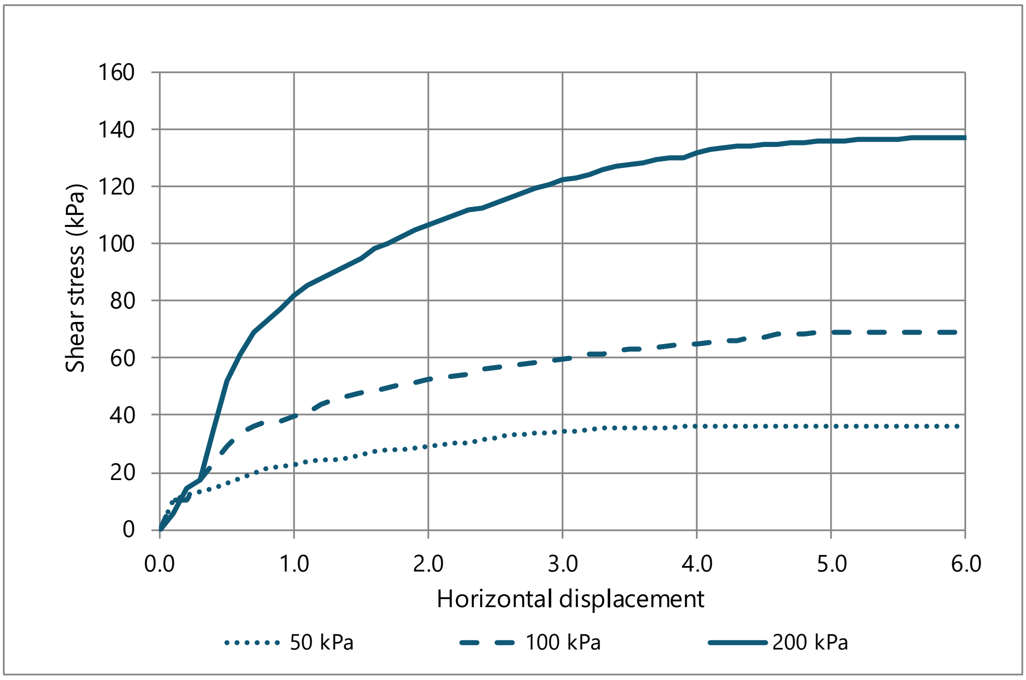

Figure 3.10 – Direct shear test results with sample 02: deviatoric stress x horizontal displacement.

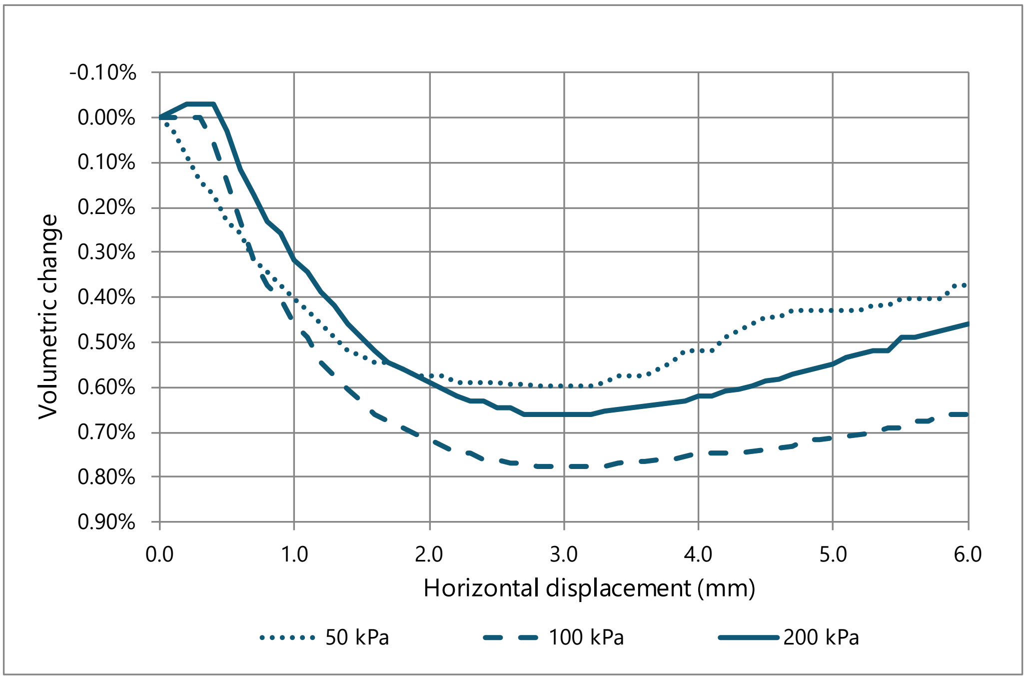

Figure 3.11 – Direct shear test results with sample 02: volumetric change x horizontal displacement.

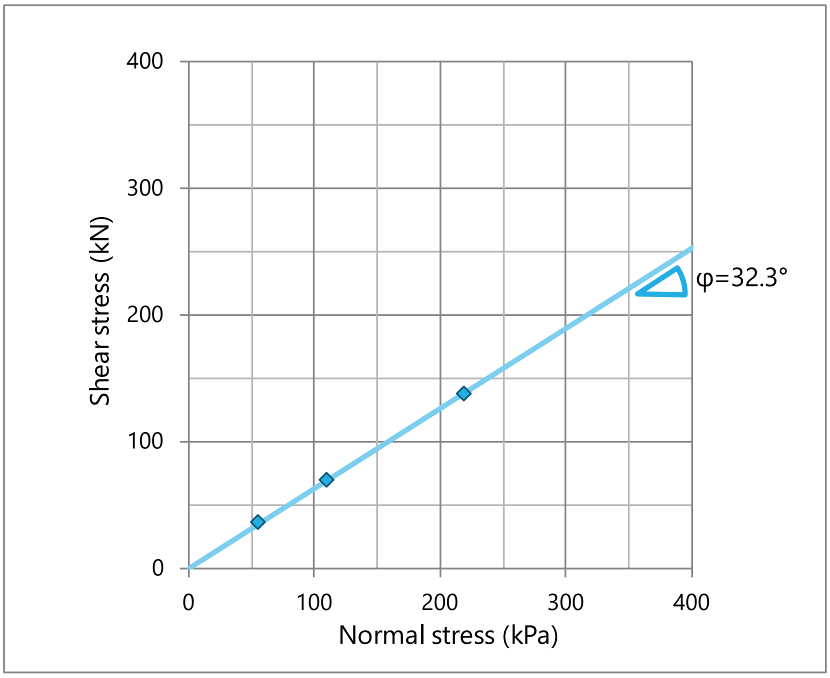

Figure 3.12 – Direct shear test results with sample 02: Mohr-Coulomb failure envelope.

3.4. Load tests

Two types of uplift axial load tests were performed: (1) tests with static loading, with one or more load-unload cycles, and (2) cyclic tests with quasi-static loading, with one of the tests followed by static loading until steep upward movement was observed. The load tests were based on ASTM D3689 – 07(2013)e1.

This item describes the geometric and mechanic properties of the prototype pile used for the tests, and includes the installation process and the test procedures.

3.4.1. Pile design

This item describes the development of the prototype pile used in all tests performed for this research. The helical pile prototype was conceived before the survey results from the construction site were available. Design assumptions, including geometric and mechanical parameters were discussed by Costa and Costa (2016). The soil parameters used in this phase of the research were obtained from laboratory tests performed with a sample collected in a similar sand deposit, also located in Natal/RN. The sand had an apparent specific weight of 17.0 kN/m^3 and internal friction angle equal to 35°.

The main design constraint was the maximum nominal torque from the hydraulic motor installed in the driller, 9.3 kN-m, and machining limitations. Based on these, the next step was to select a steel tube that would be used for the central shaft. It had to satisfy the following requirements: (1) it should have the smallest possible diameter, to reduce the torque necessary to install the pile; (2) it should have sufficient torsional inertia to resist the nominal torque from the hydraulic motor without yielding; (3) it should offer sufficient axial strength to resist the maximum axial load, estimated from using the nominal torque in equation 2.18, without yielding or breaking; (4) it should be made from a material that could be machined using locally available tools. The central shaft of the pile was made with SAE/AISI A1045 steel tubes with 73 mm in external diameter and 53 mm in internal diameter.

The geometry of the pile is presented in Figure 3.13. The pile consisted of one leading section with two helical bearing plates (Figure 3.13a), attached to a section with a single helical bearing plate (Figure 3.13b). The following sections were manufactured without plates, and were used to adjust the designated pile length (Figure 3.13c).

The helical plate sizes were based on commercial sizes, usually in multiples of 50 mm (Hubbell Power Systems, 2014). The tapered configuration was chosen to reduce the effects of disturbance. Equation 2.19 was used to estimate the installation torque caused by specific sets of plates and installation depths. The spacing between the plates was set to be three times the lower helix diameter. All helical plates were made with a pitch of 75 mm, which is commonly used in commercial plates. The capacity of the pile with different sets of plates and installation depths was estimated using the Individual Bearing and Cylindrical Shear methods, described in items 2.7.2 and 2.7.3, respectively. The set of plates selected for the final design required an installation torque close to 9.3 kN-m, which provided the highest pullout capacity. The ultimate loads estimated for the pile were Q_u = 226 kN, for the Individual Bearing method, and Q_u = 166 kN, for the Cylindrical Shear method, with the bottom helix installed at a depth of 3.6 metres. The helical bearing plates were made with SAE/AISI A1045 steel plates with 12.7 mm in thickness. The diameters of the bearing plates of the leading section are 250 and 300 mm (Figure 3.13a), and the diameter of the bearing plate of the following section is 350 mm (Figure 3.13b). The leading and trailing edges of the plates were bevelled to ease cutting the soil during installation.

The design of the couplings was based on commercial helical pile designs and adapted to local availability. Spigot and socket connections were made with SAE/AISI A1045 steel tube with 95 mm in external diameter and 73 mm in internal diameter. Hexagonal bolts, grade 8.8, with 19 mm in diameter, were used to attach the sections together. The motor-pile adapter was based on the motor-auger adapter used for piling and welded to a sleeve. The geometry of the adapter is shown in Figure 3.14.

The structural safety requirements of all sections, couplings and welding were checked according to the NBR 8800 (ABNT, 2008).

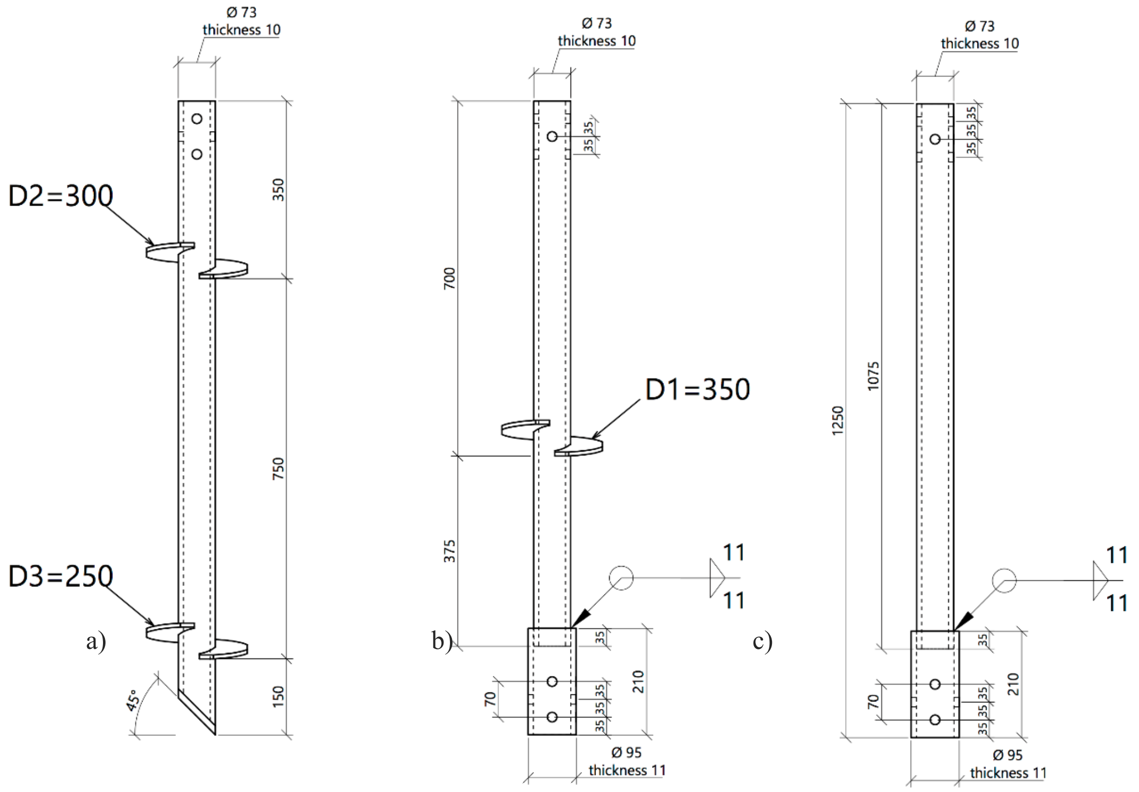

Figure 3.13 – Pile sections: a) leading section; b) extension section with helical plate; c) plain extension section. Dimensions in mm; not to scale.

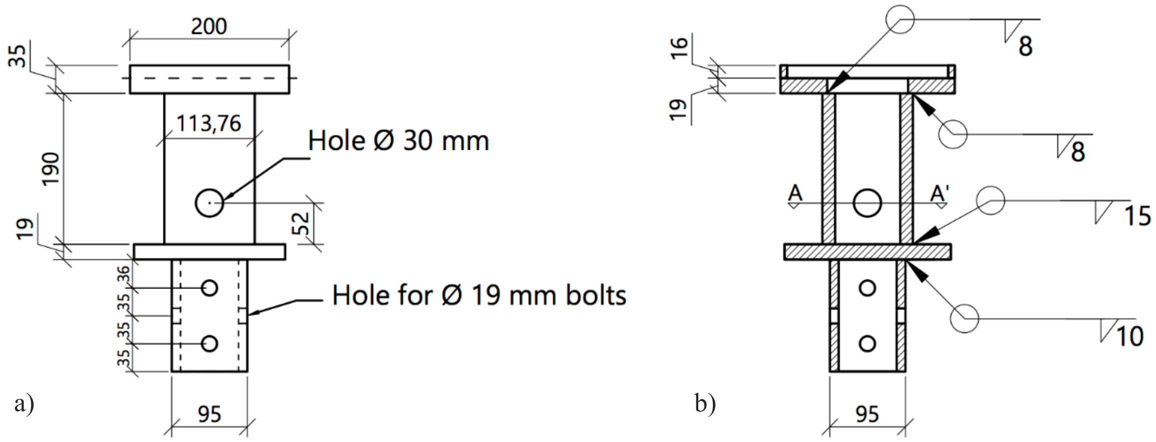

Figure 3.14 – Adapter used to install the helical pile into the ground: a) side view; and b) longitudinal section. Dimensions in mm. Not to scale.

3.4.2. Installation

For each test, the pile was installed into the ground using a drilling machine as shown in Figure 3.15. This is a MC150 unit, manufactured by CZM Foundation Equipment, in Brazil (CZM Foundation Equipment, 2012). Its hydraulic motor has a maximum nominal torque of 9.3 kN-m.

Figure 3.15 – MC150 drilling rig machine, manufactured by CZM.

The adapter use to apply the installation torque was attached to the hydraulic motor by a steel pin, and to the pile sections by three bolts. Since an independent torque measuring device was not available, the piles were screwed into the ground until reaching the machine stall torque. During installation, one extension section with one bearing plate and two plain extension sections were used in addition to the leading section with two bearing plates. The space available between the bottom of the hydraulic motor connector and the ground surface, of 1.50 m, has limited the length of the pile sections to 1.25 m, since the adapter was 0.25 m in length. Figure 3.16 shows the connection between the torque motor and the adapter, which used a pin, and between the adapter and the top of a pile section, which used hexagonal bolts. The pile was then inserted into the ground.

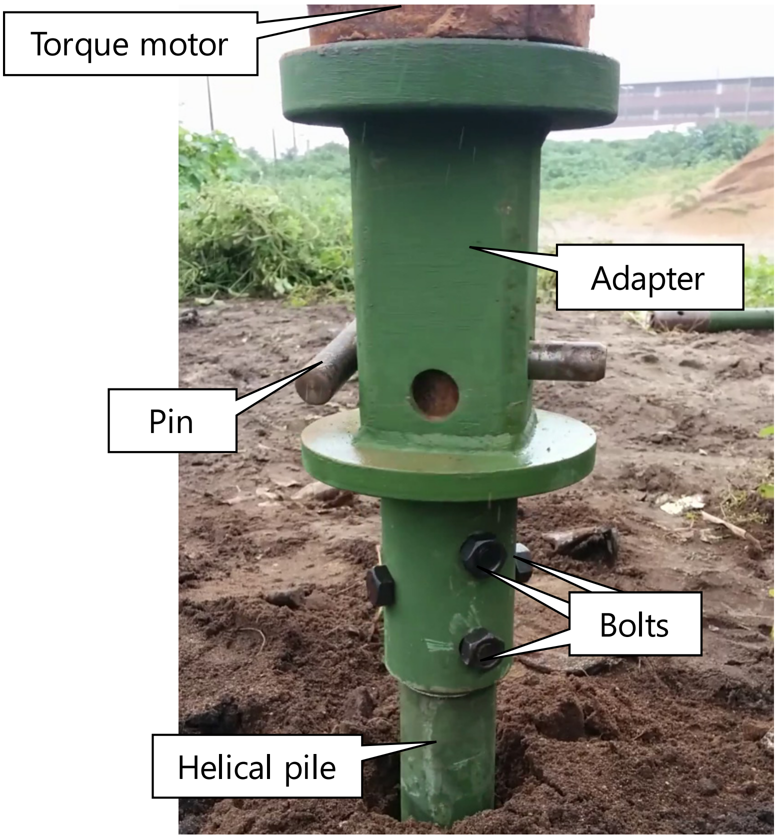

Figure 3.16 – Coupling between drilling machine and helical pile.

A hollow hydraulic cylinder with 500 kN capacity, attached to a manual hydraulic pump, was used to apply the loads during the pull-out tests. The reaction system for the tests used two steel beams 3-m long, resting on timber logs with square section. The position of the hydraulic cylinder, as well the other components of the loading and monitoring systems are presented in Figures 3.17 and 3.18. The adapter shown in Figure 3.16 was also used during the load test to transfer the pull-out force to the pile using a thread bar with 32 mm in diameter and 360 kN of maximum elastic strength. The tension load applied on the pile was measured using a hollow load cell installed above the hydraulic cylinder. The thread bar passes inside the hollow cylinder and the hollow load cell, and was firmly attached to the reaction system by a threaded nut.

Vertical displacements of the pile head were measured with four dial gages, with a stroke of 50 mm and a resolution of 0.01 mm. The dial gages were mounted on the top of the hydraulic cylinder and rested on 3-m long reference metallic beams.

Figure 3.17 – Load test setup.

Figure 3.18 – Reaction frame.

After completion of each test, the pile was unscrewed from the soil and installed in a different place, at a distance at least 5 times the diameter of the largest helical bearing plate, to prevent interference among installations. After the final test, a backhoe was used to make a cut on the soil and expose the pile in the ground.

3.4.3. Static axial tensile load tests

Five uplift static load tests were performed in the study area inside the construction site. The procedures followed for these tests were based on the Quick and the Cyclic Loading tests described in ASTM D3689 – 07(2013)e1. Before each test, a seating load of abut 5 to 10% of the anticipated failure load was applied to the systems. The locations of installation of the pile are shown in Figure 3.1b.

The first test, labelled Test A in the present work, was finished after one load-unload cycle. The load was applied in six increments of 20 kN until reaching 120 kN. Unloading was carried out in three decrements of 30 kN each. During each load and unload interval, the load was kept constant for 15 minutes.

The following two tests, labelled Test B and Test C, were performed with four load-unload cycles, with maximum applied loads of 50 kN, 100 kN, 150 kN, and until plunging failure was reached. In all cycles of test B and C, loading was applied in increments of 10 kN and the unloading was applied in decrements equal to 25% the maximum reached load. During each load and unload interval, the load was kept constant for 10 minutes.

In the fourth test, labelled Test D, the load was applied in 15 load-unload cycles. The final load of each cycle was increased in multiples of 13 kN. The unloading was applied in 1 to 5 steps. During each load and unload interval, the load was kept constant for 10 minutes.

A fifth static test, labelled Test F, was performed after completion of the first cyclic test with quasi-static loading (Test E) and is described in the next item.

3.4.4. Axial tensile load tests with quasi-static cyclic loading

Two uplift load tests with quasi-static cyclic loading were performed in the same study area as the other static tests. The same apparatus used for the static tests was used for quasi-static tests.

The first quasi-static cyclic load test, labelled Test E in the present study, was performed in five steps, defined by a minimum load (Q_{min}) and a maximum load (Q_{max}), both increasing in each step.

Anchors used to support guyed towers are subjected to a constant load at all times, even when not subjected to oscillating loads (Cerato and Victor, 2008). To simulate this condition, a minimum load of 10 kN was applied to the pile in the first step and was increased again in each subsequent step. Each step lasted one hour, during which 60 one-minute loading-unloading cycles were applied to the pile. Within each minute, the applied load oscillated between the minimum and the maximum values. After the last loading step, the pile was unloaded in three stages until reaching the load of 10 kN. From that point, a static loading test, labelled Test F, was performed in the pile by applying load increments of 10 kN until failure and following the same procedures described in item 3.4.3. During each load and unload interval, the load was kept constant for 10 minutes. The cyclic loading parameters, defined in item 2.9.1, applied to Test E are shown in Table 3.4. Figure 3.19 illustrates the amplitude of the loads applied in each step in Test E.

Table 3.3 – Cyclic loading parameters used in Test E

Step	Q_{min} **(kN)**	Q_{max} **(kN)**	Q_{mean} **(kN)**	Q_{cyclic} **(kN)**	N	**Period (s)**
F-01	10.0	20.0	15.0	5.00	60	60
F-02	20.0	35.0	27.5	7.50	60	60
F-03	30.0	55.0	42.5	12.5	60	60
F-04	40.0	75.0	57.5	17.5	60	60
F-05	55.0	100	77.5	22.5	60	60

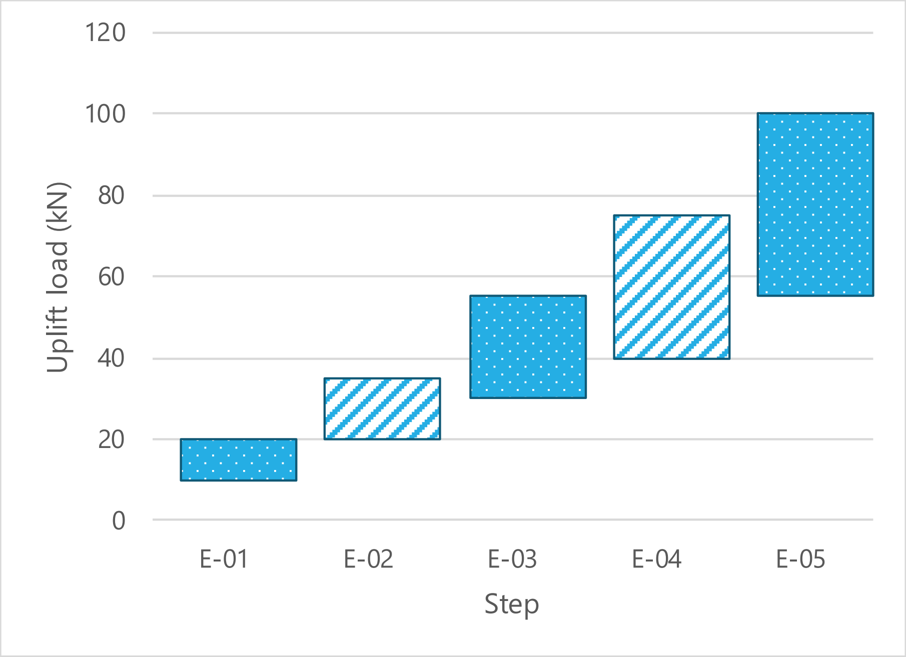

Figure 3.19 – Evolution of the loads applied in each step in Test E.

The second quasi-static cyclic load test (Test G), was also performed in five stages. However, the minimum load was maintained constant and the maximum load was increased at each stage, as shown in Table 3.4 along with the other cyclic loading parameters. Each stage lasted one hour, and comprised 60 one-minute load-unload cycles. In Test G, no static load test was performed after the quasi-static loading phase. Figure 3.20 illustrates the amplitude of the loads applied in each step in Test G.

Table 3.4 – Cyclic loading parameters used in test G

Step	Q_{min} **(kN)**	Q_{max} **(kN)**	Q_{mean} **(kN)**	Q_{cyclic} **(kN)**	N	**Period (s)**
G-01	20.0	40.0	30.0	10.0	60	60
G-02	20.0	60.0	40.0	20.0	60	60
G-03	20.0	80.0	50.0	30.0	60	60
G-04	20.0	100	60.0	40.0	60	60
G-05	20.0	150	85.0	65.0	60	60

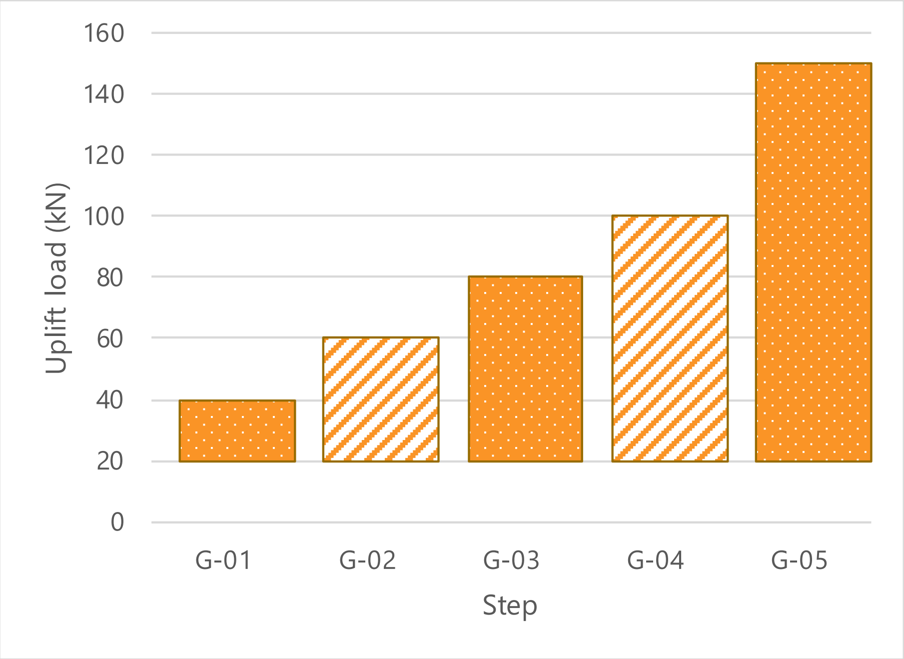

Figure 3.20 – Evolution of the loads applied in each step in Test G.

3.4.5. Testing Sequence

A summary of the testing sequence is shown in Table 3.5.

Table 3.5 – Testing sequence

Test	Type	Number of cycles
A	Static	1
B	Static	4
C	Static	4
D	Static	15
E	Quasi-static	5 × 60
F	Static	1
G	Quasi-static	5 × 60

3.5. Numerical modelling

Numerical analyses were carried out to simulate the behaviour of the pile considering different situations of geometry and loading. The analyses were performed using Finite Element Method (FEM) in software Plaxis 2D version 2016 (Plaxis, 2016).

In Plaxis 2D, axisymmetric modelling was used. It assumes that the state of strains and stresses is the same in any radial direction. The coordinates in the x-axis represent the radius and the ones in the y-axis correspond to the axial line of symmetry. An example of an axisymmetric problem showing the position of the axis is presented in Figure 3.21.

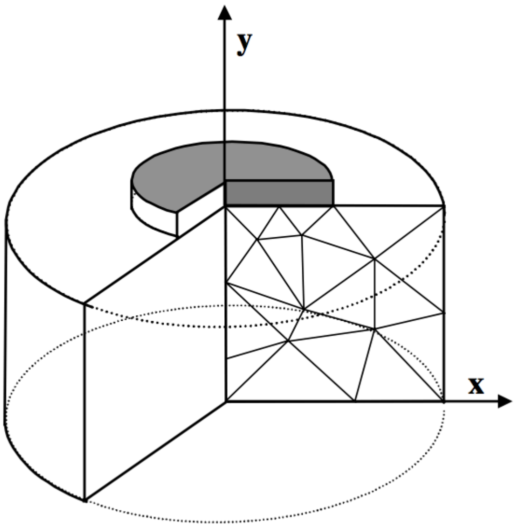

Figure 3.21 – Example of an axisymmetric problem (Plaxis, 2016).

In a two-dimensional problem, each node has two translational degrees of freedom, in the x- and y-directions. The restriction of a type of displacement is called “fixity” in Plaxis. The software automatically applies horizontal fixities to vertical geometry lines that have an x-coordinate value equal to the lowest or the highest x-coordinate values in the model, and vertical and horizontal fixities to horizontal lines in which the y-coordinate value is equal to the lower y-coordinate value from the model. Plate elements that extent to the edge of the model have their rotation restricted at the point of contact with the edge if at least one of the directions of displacement at the point is restricted.

The geometry of the load tests was modelled into three main zones, shown in Figure 3.22. The first zone represents the soil mass at its natural state; the second zone is where the soil was disturbed by pile installation; the third zone simulates the pile material.

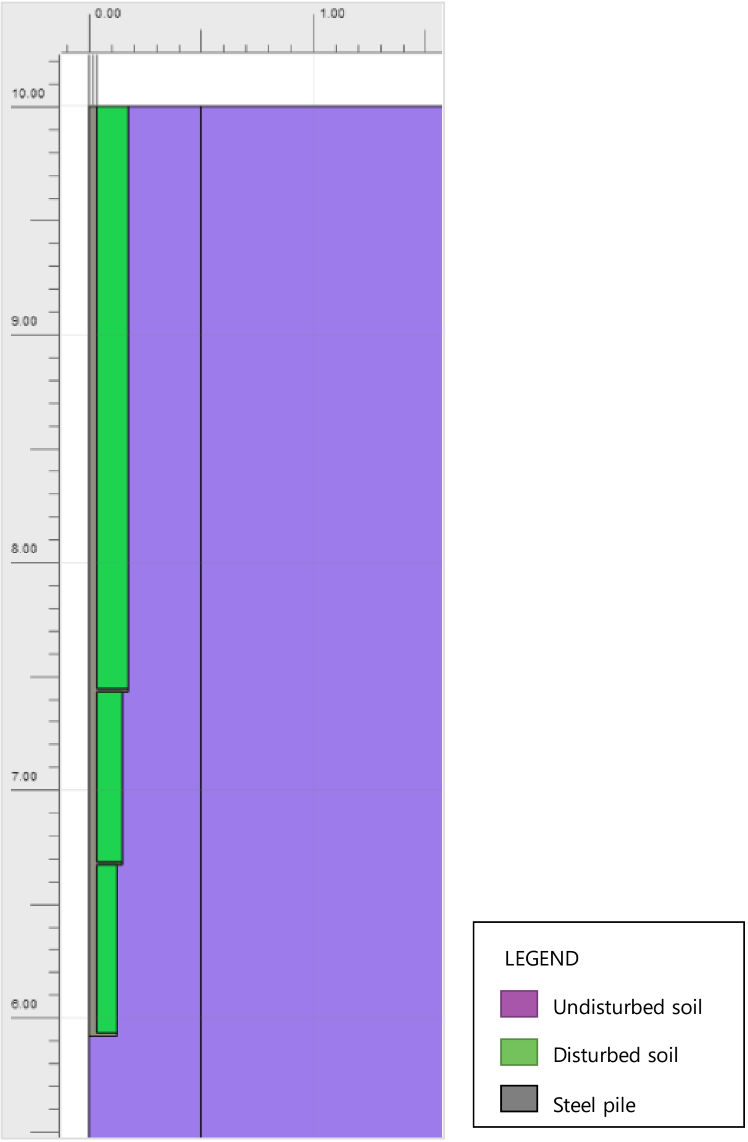

Figure 3.22 – Screenshot from Plaxis: geometry of the problem and the materials assigned to each zone.

The numerical models developed in this study were based on the geometric properties of the prototype pile and the results from the laboratory tests and the static load tests in the field. A two-dimensional 10.0 m × 10.0 m model was created in the (x,y)-plane. The y-dimension, representing depth, was set to be two times larger than the installation depth of the pile in the field to prevent boundary effects. Standard fixities were applied to prevent vertical and horizontal displacements at the base of the model and horizontal displacements at the vertical sides of the model.

The models used triangular elements with 15 nodes, which provide great accuracy for difficult problems at the cost of relatively high memory usage and longer calculation times. The global coarseness of the mesh was set to “medium” and local refinements were made inside the cylindrical zones of disturbed soil above each helix. Each cylindrical zone had a diameter equal to the largest helical plate that passed through it. Further refinements were applied inside a zone of undisturbed material, 500 mm from the axis of the pile. The mesh generated for the numerical model is shown in Figure 3.23.

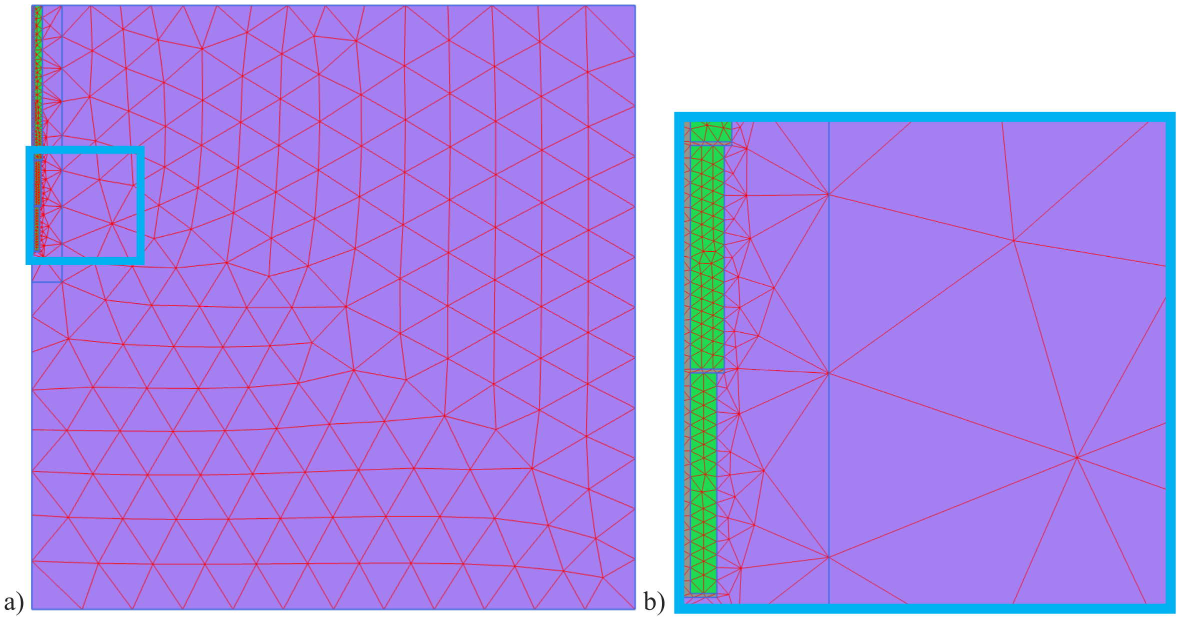

Figure 3.23 – Screenshots from Plaxis: a) mesh characteristics; b) mesh detail.

Two constitutive models were used to represent the materials. The “Elastic” model was assigned for the steel pile, the grey zone shown in Figure 3.23. This is the most suitable model because the low level of stresses during the tests did not cause yielding. The properties assigned for the steel followed the recommendations of Brazilian Standard NBR 8800 (ABNT, 2008) (Table 3.6).

Table 3.6 – Steel parameters applied to the linear elastic model

Young's modulus (MPa)	210,000
Poisson's ratio	0.300
Unit weight (kN/m³)	78.0

The sand was represented by a hyperbolic model with elastoplastic straining behaviour called "Hardening Soil" (Plaxis, 2016). In this model, shear hardening is used to model irreversible strains due to primary deviatoric loading and compression hardening is used to model irreversible plastic strains due to primary compression in oedometer loading and isotropic loading. According to Moraes (2014), this material model can be used satisfactorily to simulate local soils. Results from laboratory and field tests were used to define the soil parameters needed for the numerical model. Two types of soils were considered. The first soil represents the undisturbed soil mass and was assigned to the purple zone in Figure 3.23. The two layers observed in the Figure 3.3 were simplified as a single layer of undisturbed soil with medium relative density. The first estimates of the properties of this zone were based on the geotechnical characterization results from item 3.3. The second layer represents the cylindrical zones disturbed by the installation of the helical plates, observed during exhumation of the prototype, as discussed in item 4.2, and was assigned to the green zones around the pile in Figure 3.23. The same sand material but with reduced stiffness and strength was assigned to this zone, in accordance with the observations from Tsuha *et al.* (2012a), Schiavon (2016) and the present work.

Initially, the parameters were estimated using classic relationships found in the literature and then applied to the model. The output was then compared with the experimental results. The parameters were modified continuously within reasonable limits until the numerical results showed good agreement with the experimental results. The final data sets of mechanical properties for the two soil zones obtained from the validation process are shown in Table 3.7.

Table 3.7 – Soil parameters applied to the Hardening Soil constitutive model

Parameter	**Undisturbed soil**	**Disturbed soil**
E_{50}	50,000	30,000
υ	0.350	0.250
m	0.500	0.500
ϕ'	36.0°	33.0°
c'	5.0	1.0
ψ	6.0°	0°
K_0	0.412	0.455
γ_{unsat}	16.5	15.0

Note: E_{50}= reference Young's modulus for loading; υ = Poisson's ratio; m = power for stress-level dependency of stiffness; ϕ' = effective friction angle; c' = effective cohesion; ψ = dilatancy angle; K_0 = at-rest earth pressure coefficient; γ_{unsat} = unsaturated weight.

Interface elements based on the Mohr-Coulomb model were used to simulate the contact between the pile material and the disturbed soil. Plaxis uses a reduction factor parameter (R_{inter}) to calculate the loss of strength at the interface. The interface parameters are calculated from the soil properties by applying the rules expressed in Equations 3.1 to 3.3 (Plaxis, 2016).

$$c_i = R_{inter} c_{soil} \tag{3.1}$$

$$\tan \varphi_i = R_{inter} \tan \varphi_{soil} \leq \tan \varphi_{soil} \tag{3.2}$$

$$\psi_i = 0^\circ \text{ for } R_{inter} < 1\text{, otherwise } \varphi_i = \varphi_{soil} \tag{3.3}$$

Kulhawy (2984) recommends φ_i/φ_{soil} ratios varying from 0.5 to 0.9 for steel piles in sand, depending on the smoothness of the steel surface. Based on this recommendation, it was assumed R_{inter} = 0.67, which corresponds to φ_i = 23°. Interface stiffness was assumed equal to soil stiffness.

After the definition of input geometry, material data sets, and boundary conditions, Plaxis generates a finite element mesh and calculates the initial stress conditions inside the soil mass based on the at-rest earth pressure coefficient of the undisturbed soil.

In the next step, the program directs the user to the calculation module, the problem can be subdivided in as many phases as necessary to simulate the construction phases performed in the field. In each phase, the user defines the loads and displacements applied to the soil mass and other structures. Two phases were used in this work to simulate a static load test. In the first phase, the material inside the disturbed zone, originally assigned to be undisturbed soil, was replaced by the disturbed soil data. The undisturbed soil in the zone corresponding to the pile was replaced by the steel data. In the second phase, a distributed load was applied to the top of the pile to simulate the uplift load during the test. After the definition of the construction phases, the user can select displacement nodes and stress points that can later be used to generate curves. Plaxis then executes the calculation phases. After the calculation, the user can view the results from the final phase using the output module or generate curves relating the load steps with displacements and stresses inside the soil mass.

The calibrated numerical model was then used as basis of a series of parametric analyses. The effects of four parameters were investigated:

1. **Relative embedment ratio (H_1/D_1):** The depth of the top helical plate used in the numerical simulations ranged between 0.50 to 5.00 m, with 0.50 m intervals, which correspond to relative embedment ratios (H_1/D_1) between 1.43 and 14.3 (D_1 is the diameter of the top plate). The investigation included the same helix diameters and inter-helix distances of the prototype pile tested in the field.
2. **Helical plate diameter (D_i):** This parameter was evaluated in two configurations. In the first configuration the pile was set with three helices with the same size in the first configuration (uniform configuration). In the second configuration, the pile was set with three helices with sizes decreasing with depth (tapered configuration). The diameters used in both configurations are shown in table 3.8. All analyses were performed using an embedment ratio (H_1/D_1) equal to 7.3, which is the same embedment ratio used in the test A. The inter-helix spacing was equal to 3 times the diameter of the smallest helix.

Table 3.8 – Diameters used in the parametric analyses

Uniform configuration	**Tapered configuration**		
$D_1 = D_2 = D_3$ **(mm)**	D_1 **(mm)**	D_2 **(mm)**	D_3 **(mm)**
200	150	200	250
225	175	225	275
250	200	250	300
275	225	275	325
300	250	300	350
325	275	325	375
350	300	350	400
375	325	375	425
400	350	400	450

3. **Inter-helix spacing ratio (s_i/D_i):** The spacing ratios used in the study were: 2, 2.5, 3, 3.5, 4, 4.5 and 5. All spacing ratios were calculated for the tapered configuration with the following plate diameters: D_1 = 350 mm, D_2 = 300 mm, and D_3 = 250 mm. The lower plates of all models in this analysis are located at the same depth as the lower plate in Test A, H_3 = 4.08 m.
4. **Number of helices:** Piles with one, two, three, and four helices were simulated to study the effect of number of plates. A pile with four plates was used as reference. The depth of the top plate in the reference pile was defined as 5.62 m, which corresponded to an embedment ratio (H_1/D_1) of 7.3. The spacing ratio between plates in piles with more the one helix was 3.00. In the piles with three or less helices, the depth of the helices corresponded to the ones used in the four-plate configuration, as summarized in Table 3.9 and illustrated in Figure 3.24. The uplift capacity of piles with multiple helices was compared with the sum of the capacities of single-helix piles.

Table 3.9 – Depths and diameters used in the parametric analyses

Config.	**Number of plates**	D_4 **(mm)**	H_4 **(m)**	D_3 **(mm)**	H_3 **(m)**	H_2 **(mm)**	H_2 **(m)**	D_1 **(mm)**	H_1 **(m)**
a	1	-	-	-	-	-	-	400	2.92
b	1	-	-	-	-	350	3.97	-	-
c	1	-	-	300	4.87	-	-	-	-
d	1	250	5.62	-	-	-	-	-	-
e	2	250	5.62	300	4.87	-	-	-	-
f	3	250	5.62	300	4.87	350	3.97	-	-
g	4	250	5.62	300	4.87	350	3.97	400	2.92

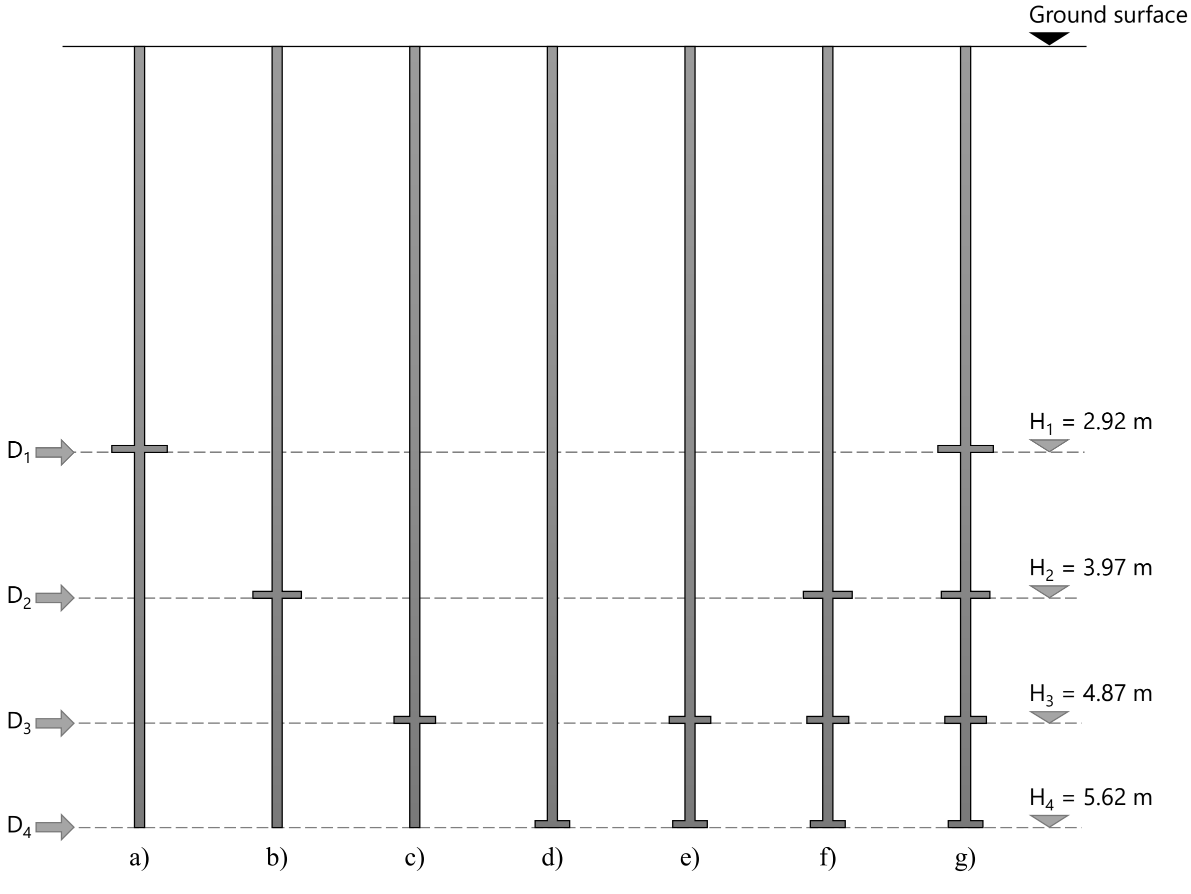

Figure 3.24 – Geometry of the piles used in the analysis of number of helices.

4. RESULTS AND DISCUSSION

This chapter presents and discusses the results from the static and quasi-static cyclic tensile load tests and the numerical simulations and the parametric analyses.

4.1. Installation process

During installation, the pile was inserted into the ground until refusal, at an approximate rotation rate of 40 rpm, and a penetration rate of 19 mm per rotation, corresponding to an Installation Disturbance Factor (Lutenegger *et al.*, 2014) of 2.5. These rates differ slightly from the typical rates recommended by the industry and were chosen because of the low capacity of the torque motor. The augering effect generated by the higher rotation rate and the lower penetration rate allowed the pile to reach greater depths, which enabled deep anchor behaviour. However, this procedure has the disadvantage of causing more disturbance of the soil around the pile, which may reduce pile capacity. The depth at which the top and the bottom helical bearing plates were located after installation, H_1 and H_3, respectively, as well the ratio between H_1 and the diameter of the top helical plate, D_1, are shown in Table 4.1.

Table 4.1 – Depth of the helical plates after installation

Test	H_1 **(m)**	H_1/D_1	H_3 **(m)**
A	2.57	7.3	4.08
B	2.52	7.2	4.03
C	2.22	6.3	3.73
D	2.62	7.5	4.13
E, F	2.77	7.9	4.28
G	2.47	7.1	3.98

Queiroz (2018, in print) measured the maximum torque applied by the MC150 drilling rig machine when installing the pile used in the present work in similar soil conditions and obtained a value of about 8.0 kN-m

4.2. Prototype exhumation after testing

After cyclic test G, the pile was removed from the soil with of a backhoe. The soil was dug and a longitudinal view of the pile was exposed, as shown in Figure 4.1. The same picture shows that the soil on the path of the helical plates exhibited a darker colour than the undisturbed soil mass. The excavation reached a depth of about 2 m before the pile was pulled from the ground. The diameter of the cylinder of disturbed material at this depth was approximately 350 mm, which corresponds to the diameter of the top helix. After laboratory testing, it was confirmed that the material with dark colour presented a water content of 6.4%, which was higher than the water content of the surrounding soil, of 2.5%. Dynamic cone penetrometer tests performed by Costa (2017) before and after the installation of the same prototype pile in similar soil and machinery conditions showed that, after installation, the soil mass close to the pile shaft and above the shallowest helical pate had reduced strength properties.

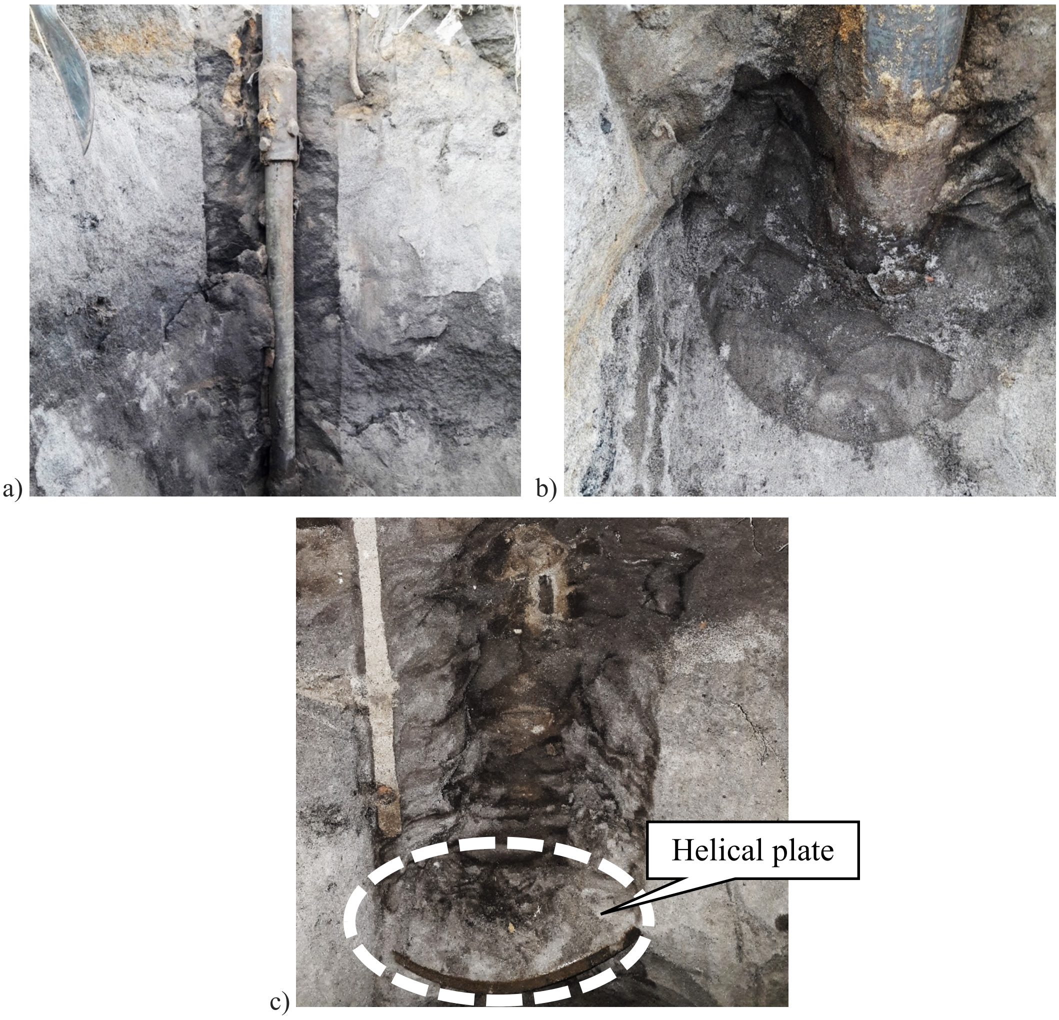

Figure 4.1 – Zone of disturbance in the soil after pile installation for test G: a) side view, b) cross-section view and c) side view showing the top helical plate.

4.3. Static loading tests

Five static load tests were performed on the anchor prototype installed in the site under study. The first four tests were performed according to the procedures described in item 3.4.3 and they were labelled as test A to D, according to their order of execution. A fifth test, labelled Test F, was performed right after the completion of a quasi-static test, using the same installation, and its results are shown in item 4.4.5. The load displacement curves obtained from the test A to D are shown in Figures 4.2 to 4.5, respectively.

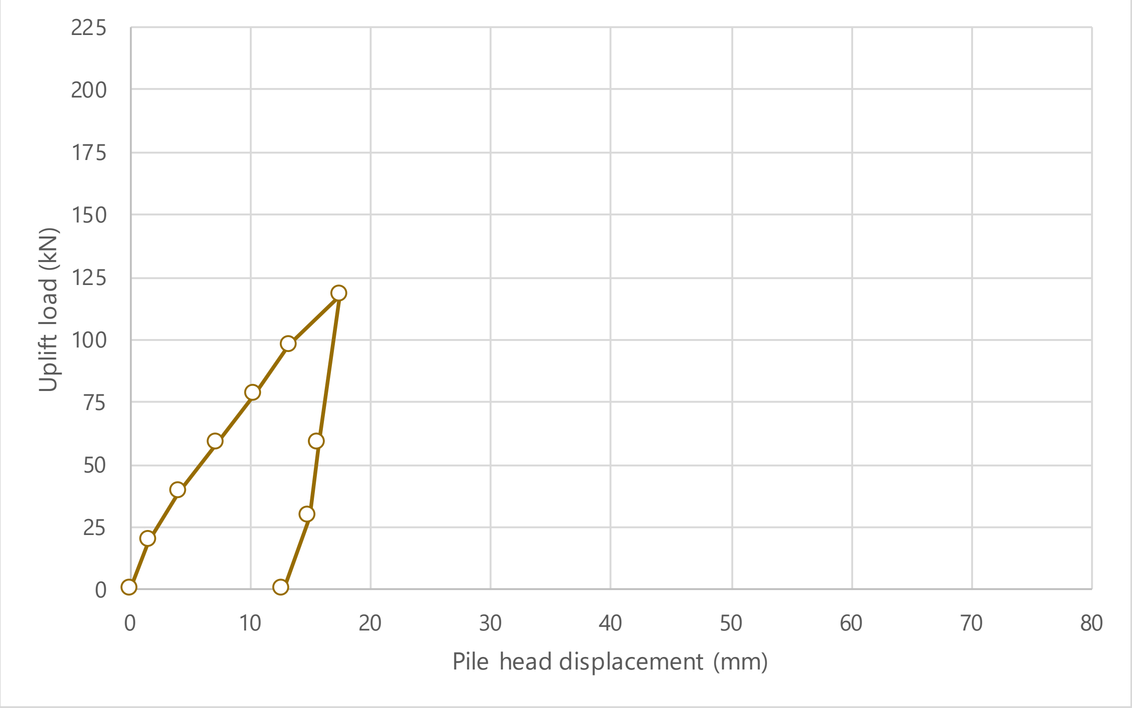

Figure 4.2 – Load-displacement response of Test A.

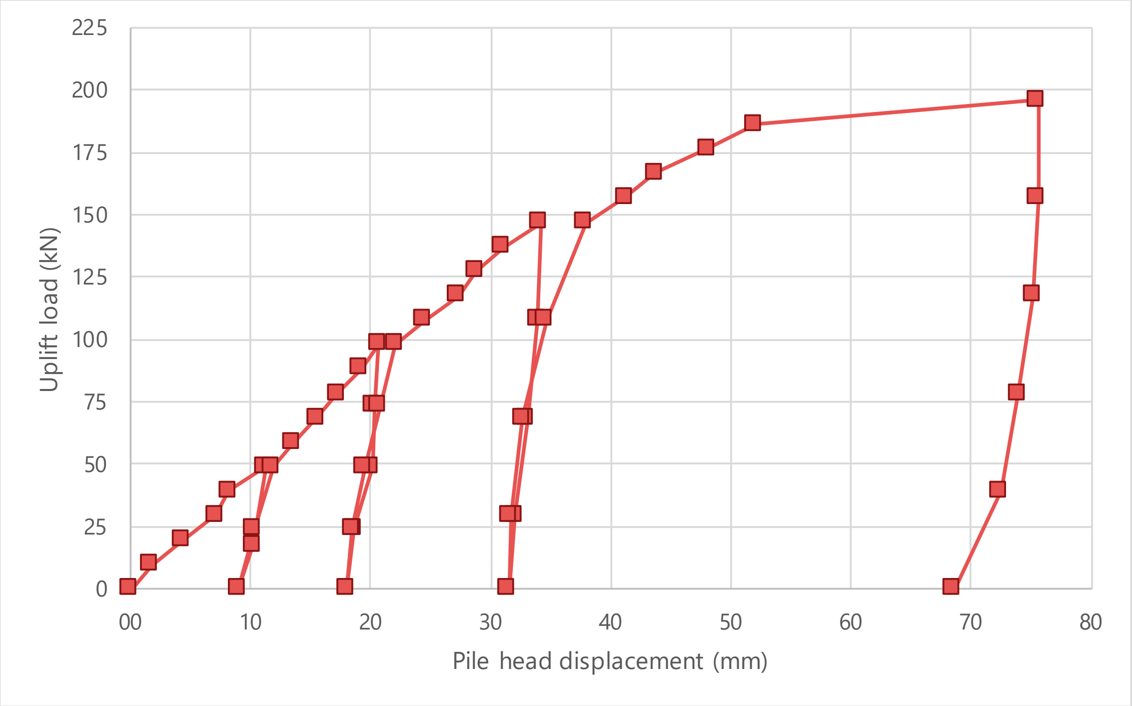

Figure 4.3 – Load-displacement response of Test B.

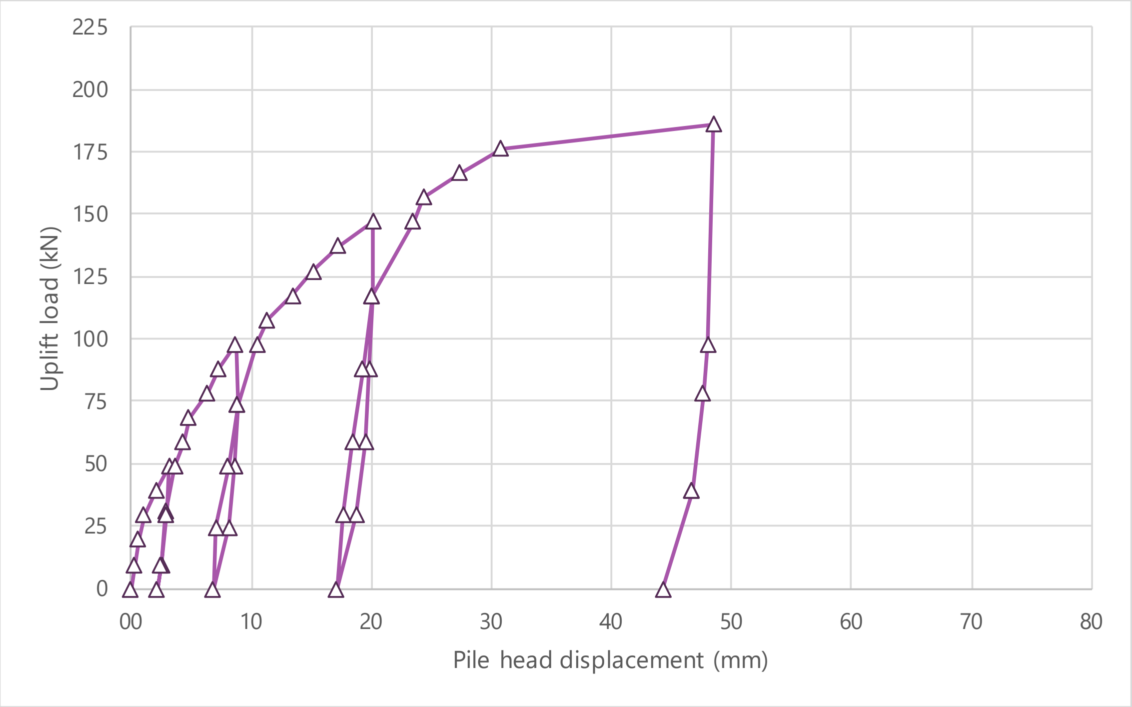

Figure 4.4 – Load-displacement response of Test C.

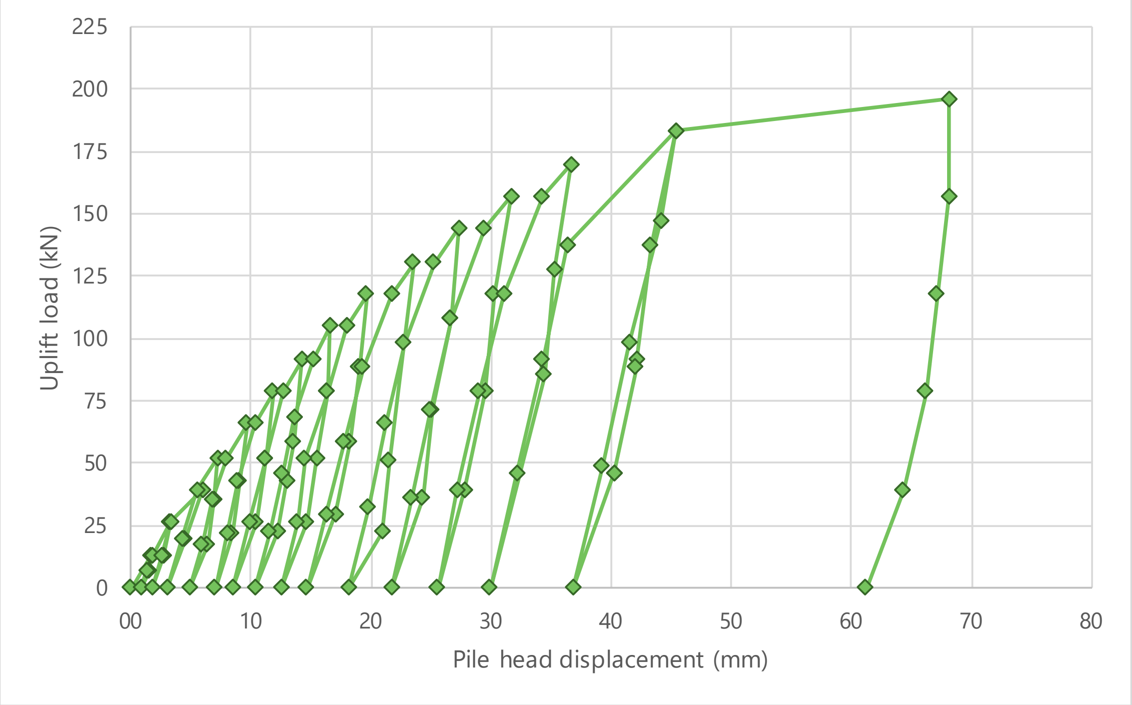

Figure 4.5 – Load-displacement response of Test D.

4.3.1. Ultimate uplift capacity from load-displacement curves

All tests are represented in Figure 4.6 by their respective envelopes, composed by the points of maximum load achieved in each loading cycle. It can be observed that test B, C, and D exhibited physical failure and Test A was not loaded until failure. For tests in which physical failure occurred, the ultimate uplift capacity was determined according to the AC358 (ICC-ES, 2007), which defines it as the load achieved when plunging of the helical plate occurs and is represented by the uppermost point of their corresponding load-deflection curves. The ultimate load capacities are almost identical, and the mean load capacity is 193 kN. The individual values are shown in Table 4.2. Although test A did not fail, its load-deflection curve closely follows the curve from Test D, so that it could be assumed to fail at the same load.

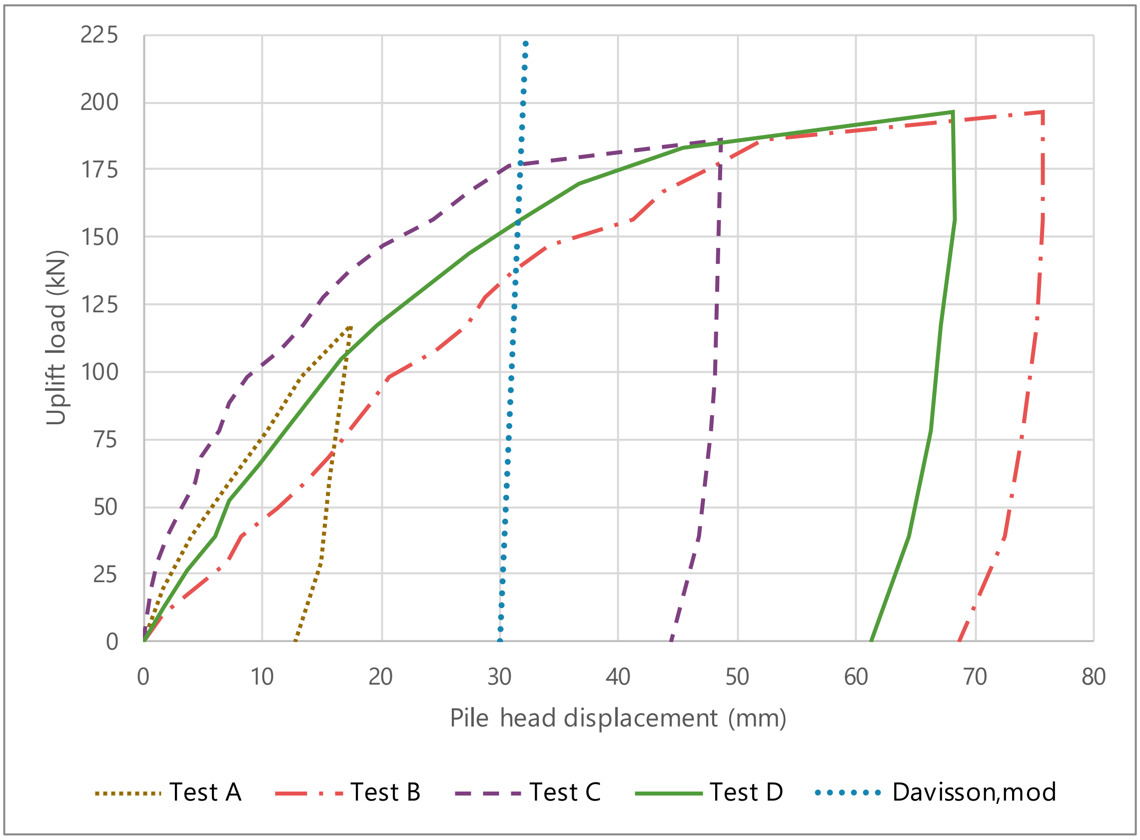

Figure 4.6 – Envelopes of the load-displacement response of all static loading tests.

Figure 4.6 also shows a straight line originated from the modified Davisson method, in which the ultimate capacity is defined as the load that corresponds to a net displacement of the head of the pile equal to 10% of the average diameter of the helical bearing plates. The method is recommended by the AC358 (ICC-ES, 2007) for tests in which plunging of the helical plate is not observed. The condition has been used by Zhang (1999) and Tsuha (2007) and is considered an industry standard (Hubbell Power Systems, 2014). The shapes of the curves are different due to variations in soil and installation conditions, which results in the line originated from the method crossing the curves at different loads.

The maximum load applied in the field tests Q_{max}^{field}, for which plunging was observed, the corresponding displacement at failure (U_{max}), and the associated relative displacement (the ratio between the displacement and the average diameter of the helices, U_{max}/D) are shown in Table 4.2. The ultimate uplift capacity obtained using the modified Davisson criterion ($Q_{u,moddav}^{field}$) and Van der Veen's method ($Q_{u,vdv}^{field}$) are also shown in the table. Particularly, the uplift capacity obtained from Test C is very close to the uplift capacities predicted by the modified Davisson criterion and Van der Veen's method. Table 4.2 also contains the torque correlation factors (K_t) for each test, calculated from the measurements obtained by Queiroz (2018). The torque correlation method will be discussed in the next item.

Table 4.2 – Ultimate capacity from piles Q_u

Test	Q_{max}^{field} **(kN)**	U_{max} **(mm)**	U_{max}/D	K_t **(m^{-1})**	$Q_{u,moddav}^{field}$ **(kN)**	$Q_{u,vdv}^{field}$ **(kN)**
A	-	-	-	-	-	-
B	196	57.2	0.19	24.5	138	230
C	186	42.4	0.14	23.3	177	190
D	196	57.8	0.19	24.5	156	210
Mean	**193**	**52.4**	**0.17**	**24.1**	**157**	**210**

4.3.2. Suitability of design methods to predict ultimate uplift capacity

The ultimate uplift capacity of the piles was also calculated based on soil data obtained from the laboratory tests and the actual installation depths, using the individual bearing (IB) method and the cylindrical shear (CS) method (Equations 2.1 and 2.8, respectively). The properties from sample 01 obtained from laboratory and field tests were used in this analysis. According to the individual bearing method, the uplift capacity of a pile installed in a homogenous deposit does not increase with increasing depths after a critical depth is reached. This resulted the same predicted uplift capacity for all tests, 171 kN. The critical depth was also used to calculate the ultimate bearing pressure, q_{ult}, for the top helical plate in the cylindrical shear method. The predicted uplift loads obtained by this method are very similar, ranging between 164 and 165 kN.

The ultimate uplift capacity was also estimated using the torque correlation (KT) method (equation 2.13). The capacity-to-torque ratio obtained with equation 2.14 has a value of 27.7 m^{-1}, resulting in a predicted uplift load capacity of 222 kN. It was assumed that the maximum torque value of 8.0 kN-m (Queiroz, 2018) was the same for all installations. The predicted uplift capacity is the same for all tests because depth is not directly accounted for in this method. Despite this, the value obtained from the equation is very close to the values calculated from the field tests.

In general, predicted uplift capacities using the IB, CS, and KT methods are fairly close to the field results. The theoretical methods, however, gave underpredicted capacities: the failures loads predicted by the IB and CS methods are 89% and 85% of the maximum load obtained from the field tests, respectively. The failure load predicted by the empirical method (KT) is 15% higher than the maximum load applied in the field. Particularly, the individual bearing method provided the best estimates for uplift capacity. Since equation 2.14 seems to overestimate the capacity-to-torque factor, it is suggested the use of an efficiency factor with an approximate value of 0.87 to correct the calculated uplift capacity.

4.3.3. Secant axial pile stiffness

The secant axial stiffness (k) can be used to assess changes in the soil-pile behaviour during the loading and unloading phases of each cycle. Parameter k is defined in the present work as the ratio between the load applied during a step and its associated final displacement, as expressed by Eq. 4.1.

$$k_i = Q_i/U_i \tag{4.1}$$

In the following analyses, k is normalized by the initial reference secant stiffness (k_{ref}), which is calculated using the load applied in the first step of each test (Q_{ref}) and its associated displacement (U_{ref}). The evolution of the axial stiffness parameter with the applied load in test A to D is shown in Figure 4.7. Figure 4.7a shows the stiffness parameter normalized by reference stiffness (k_i/k_{ref}) plotted against the applied load (Q). The plotted curves show the degradation of stiffness of the soil-pile system with loading and the non-linearity of this behaviour. Large relative stiffness decreases were observed in the last load steps of tests B, C, and D, as plunging failure occurred. Figure 4.7b shows the same data in absolute value. It can be noticed that each test exhibited different axial stiffness values at the first loading steps, which tend to converge to a single value with increasing load.

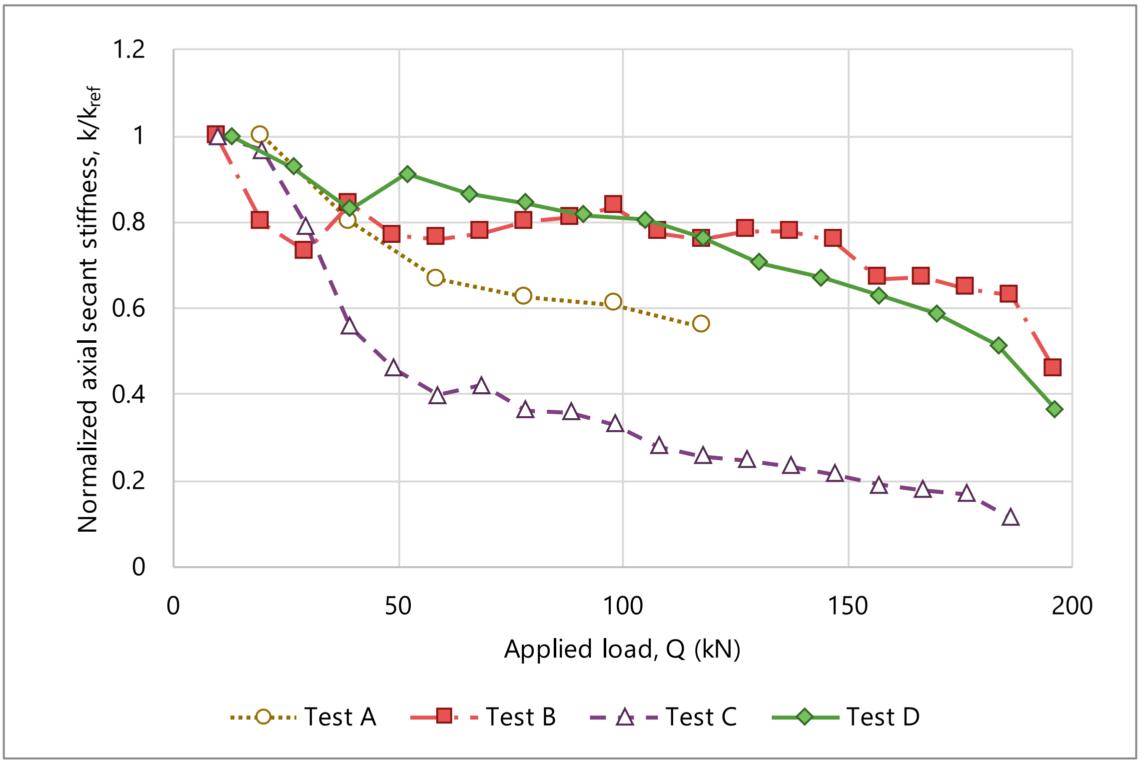
a)

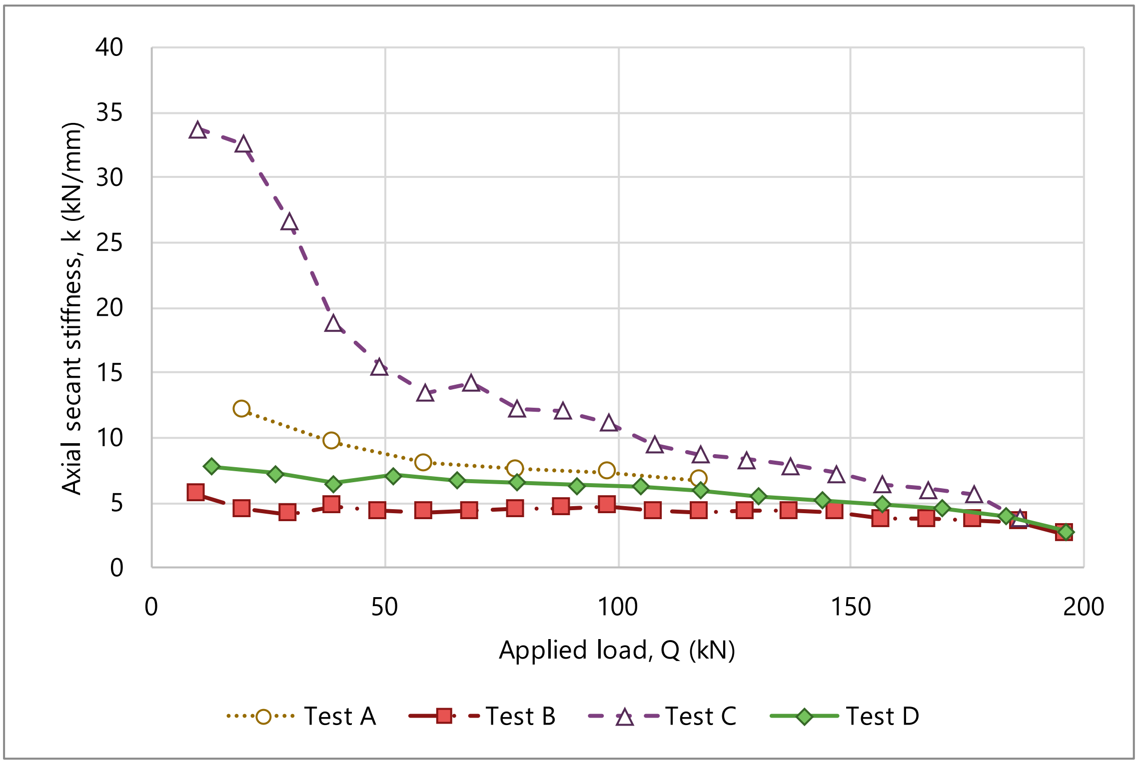
b)

Figure 4.7 – Axial stiffness plotted against applied load:

a) normalized against reference stiffness; b) absolute values.

4.3.4. Effect of load cycles on pile stiffness

Test A was performed with a single load-unload cycle, test B and C were performed with four cycles, and Test D was subjected to 15 cycles. In test B, C, and D it was possible to observe that the application of cycles has influence on the stiffness of the following cycles. The differences observed among the initial stiffness values calculated for each cycles are discussed in item 4.3.4.1. Item 4.3.4.2 discusses how stiffness changes within each cycle as the application of load progresses.

4.3.4.1. Loading axial stiffness

Figure 4.8 shows the axial stiffness (k) reached at the first loading step of the first cycle of each test (initial stiffness) and the axial stiffness calculated from the reloading steps of the subsequent cycles (reloading stiffness).

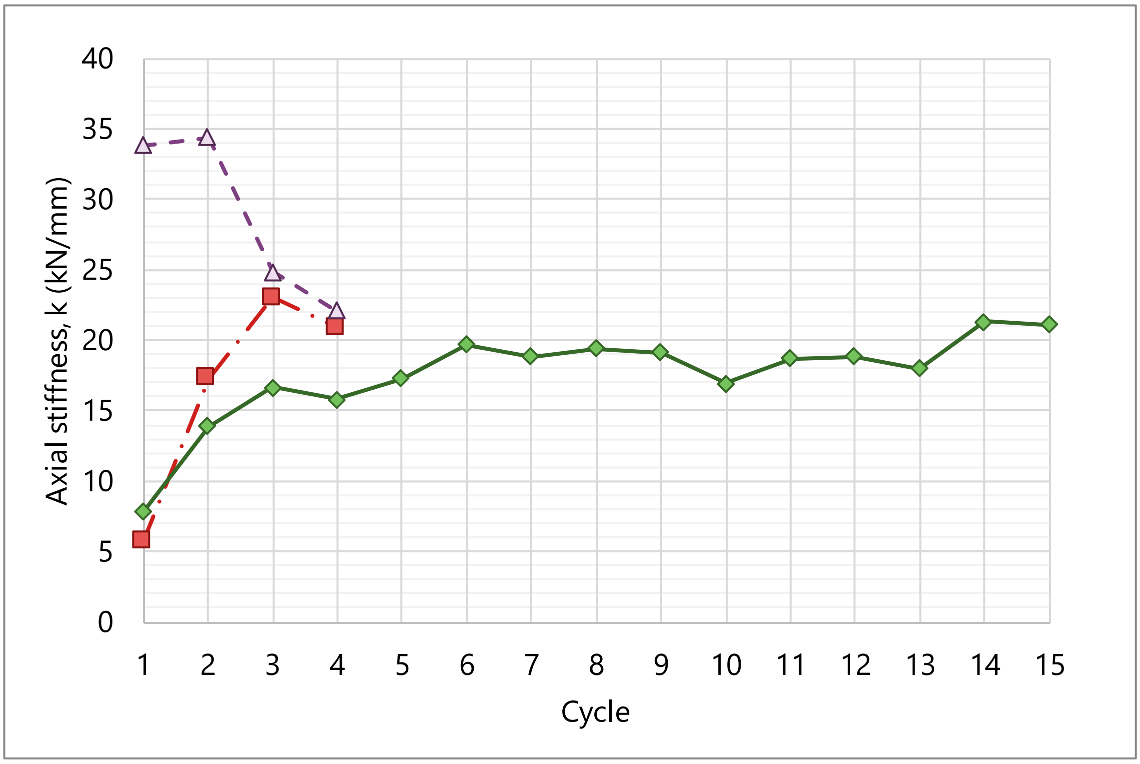

Figure 4.8 – Normalized stiffness from the first loading step of each cycle: a) Test B; b) Test C; c) Test D.

Initial stiffness is very different in each test installation. However, stiffness tends to converge to a single value as new cycles are applied. In Test B, k starts at 6 kN/mm and increases to 21 kN/mm after three cycles. In Test C, k starts at 34 kN/mm and decreases to 22 kN/mm after three cycles. In Test D, k starts at 8 kN/mm and increases until the sixth cycle. The tendency shown by k with the application of further cycles is to remain constant around 20 kN/mm. The trend shown in Test D clearly indicates that k converges to a residual axial stiffness (k_{res}) after several cycles. Although only a few cycles were applied in tests B and C, a tendency of reaching k_{res} is also noticed in these two tests.

The initial low stiffness in tests B and D may be explained by the comparatively loose condition of the soil around the plates before the tests, due to the disturbance caused by pile installation. Continuous deformations of the soil with the application of the loading cycles brings the soil to a denser state. In turn, a denser material above the helical plates leads to an increase in shear strength within the soil mass and in the stiffness of the soil-pile system. The sand reaches its maximum density after a few cycles and residual shear strength of the soil is also reached at large strains. The sand reaches its maximum density after a few cycles and residual shear strength of the soil is also reached at large strains. This causes stiffness to approach its residual value (k_{res}), as shown in Test D.

On the other hand, the installation of the pile for Test C resulted in a dense material around the plates, which led to a high soil-pile stiffness in the first load cycle. In the first cycle, peak shear strength is reached at small strains due to the high density of the soil. In the following cycles, shearing develops in a previously deformed soil. The peak strength reduces as strains accumulates upon successive load-unload-reload paths, and soil-pile stiffness becomes smaller after each new cycle. Additional cycles in Test D would give stiffness values approaching the residual stiffness k_{res} found in Test D, which is around 20 kN/mm.

The slippage of soil towards the gap formed beneath the bearing plates may also play an important role on the reduction of the soil-pile stiffness after each loading cycle. Decreases in the density of the soil around the plates caused by rearrangement of particles attenuates shear strength of the soil, and consequently reduces soil-pile stiffness. Experimental evidence of formation of gaps in helical piles is reported by Schiavon (2016).

4.3.4.2. Stiffness variation within a cycle

Figure 4.9 shows that stiffness in the first step of the reloading cycles follows the same general trend of degradation with increasing load shown in Figure 4.7.

Figures 4.9a and 4.9b show that increasing loads within each cycle decreased the stiffness to levels that are close to those observed in the previous cycles, particularly after the applied load exceeds the maximum load achieved in the previous cycle. For example, in the 4th cycle of Test B, stiffness decreased to 34% of its initial value after one single load step. After seven loads steps, close to reaching failure, stiffness decreased by 95% and became equal to the last load step of the previous cycle. In Test C, the stiffness in the last step of each load cycle reduced to a value between 12% and 46% of the initial stiffness.

In the cycles of Test D (Figure 4.9c), stiffness does not decreases immediately after the application of a new load step. In many cases, the stiffness achieved after application of a new load step is slightly higher than the initial stiffness, as observed in the 5th and 11th cycles. However, stiffness decreases after the applied load exceeds previous load levels. At the last loading step of most cycles of Test D, stiffness decreased to values between 53% to 87% of the initial value. The largest decrease was found in the 15th cycle, in which stiffness fell to 31% of its initial value. Unlike tests B and C, the stiffness at the end of the cycles of Test D do not show a stabilizing trend. This occurred because the load steps in this test were smaller than the steps used in tests B and C which resulted in reduced overlap between steps.

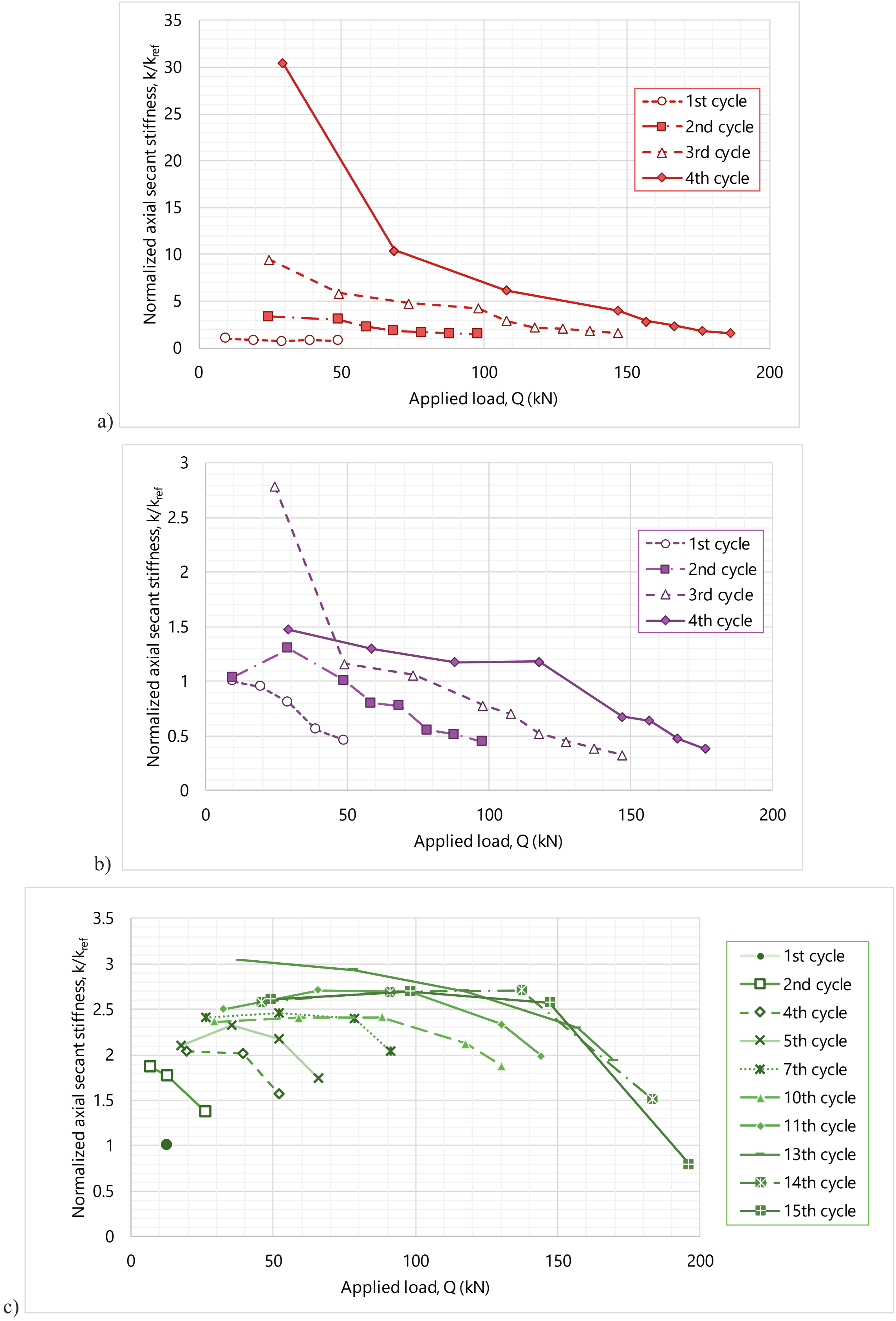

Figure 4.9 – Stiffness degradation of piles during loading cycles normalized by the reference stiffness plotted against normalized load: a) Test B; b) Test C; c) Test D (some cycles were removed for clarity).

4.4. Quasi-static cyclic loading tests

Two quasi-static load tests were performed on the anchor prototype in the investigated site. The tests were labelled Test E and Test G and each one was carried out in five steps. Details of the procedures of those tests can be found in item 3.4.4. Each step can be defined by a pair of mean load (Q_{mean}) and cyclic load (Q_{cyclic}) amplitude values. Table 4.3 shows the minimum and the maximum loads recorded during each step of test E and G, as well as the cyclic loading parameters from each step normalized by the mean uplift capacity Q_T, equal to 193 kN. In most steps, the minimum load of a step is lower than the maximum load of the previous step. This occurs when the difference between the minimum load of a step and the maximum load of its previous step, noted as Q_{inters}, is positive. In this situation, part of the load applied in a new step consists of a reloading, which has been observed in the static tests to increase soil stiffness and reduce the corresponding displacements. The parameter Q_{inters} was calculated for each step and normalized by the cyclic amplitude of the corresponding step. The ratio Q_{inters}/Q_{cyclic} is herein called intersection factor and is shown in Table 4.4 for all steps in which intersection was observed. For example, in step E-03, Q_{inters}/Q_{cyclic} is 0.17, which means that 17% of the cyclic amplitude of that step intersects with the loading applied in step E-02.

Table 4.3 – Normalized cyclic loading parameters used in test E and G

Step	Q_{min} (kN)	Q_{max} (kN)	Q_{inters}/Q_{cyclic}	Q_{mean}/Q_T	Q_{cyclic}/Q_T
E-01	11.2	20.0	N/A	0.08	0.02
E-02	22.2	39.6	N/A	0.16	0.05
E-03	35.4	59.5	0.17	0.25	0.06
E-04	48.1	79.0	0.37	0.33	0.08
E-05	57.5	98.2	0.53	0.40	0.11
G-01	18.2	39.9	N/A	0.15	0.06
G-02	18.7	59.8	0.52	0.20	0.11
G-03	17.6	79.3	0.68	0.25	0.16
G-04	19.5	99.4	0.75	0.31	0.21
G-05	20.2	147.8	0.62	0.44	0.33

The progress of quasi-static loading Test E is presented in Figure 4.10, which shows the applied loads and displacements plotted against time. Since the loads were applied manually, in a few circumstances the applied load either exceeded or went beneath the target load. Specifically, excessive loading was applied at the beginning of the second step of Test E. This resulted in a sharp increase in displacement and a slight increase in soil stiffness around the bearing plates, which might have had an influence in reducing the displacements of the initial cycles in subsequent steps. Similarly, the progress with time of applied loads and displacements in Test G is shown in Figure 4.11. In this test, the pre-tensile (or minimum) load was kept constant in all load steps, while the cyclic amplitude was increased gradually.

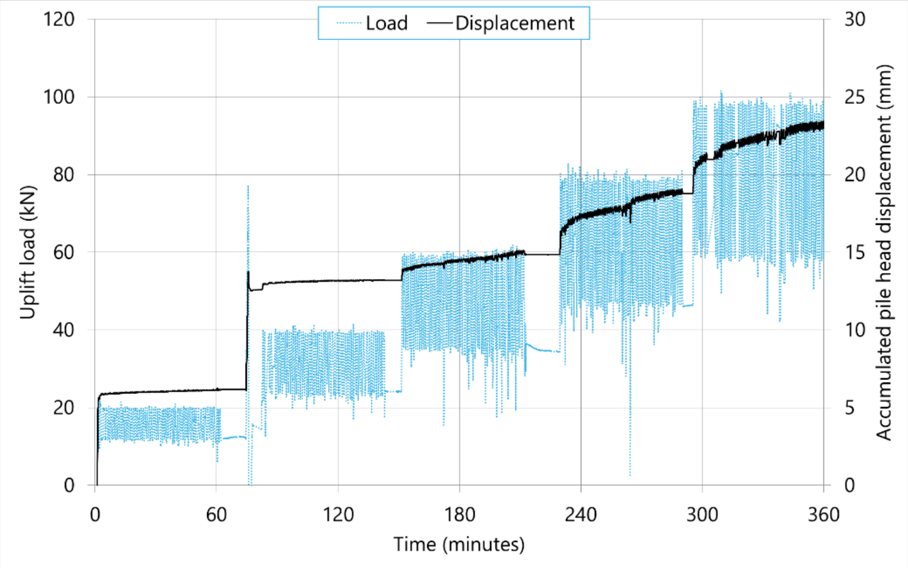

Figure 4.10 – Progress of Test E.

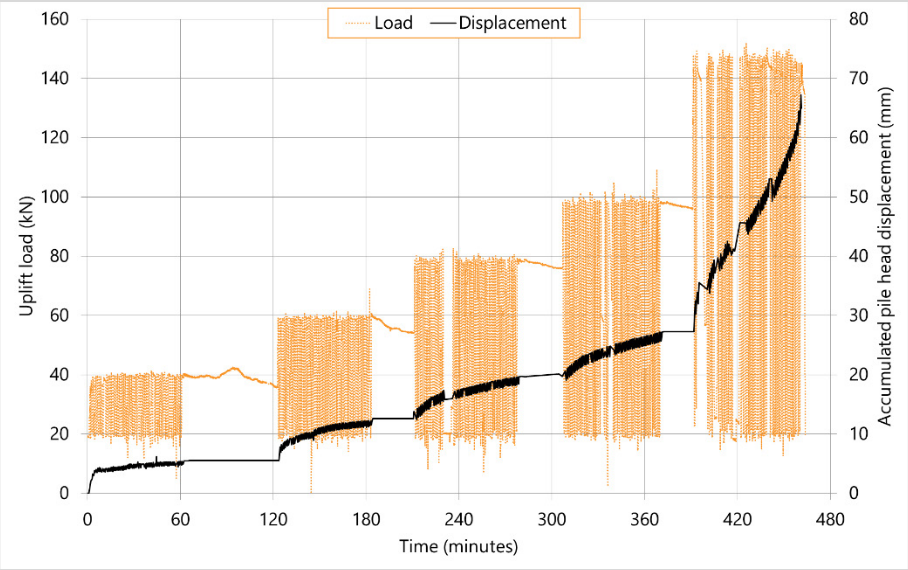

Figure 4.11 – Progress of Test G.

4.4.1. Accumulated displacements

Accumulated, or permanent, displacement (U_{acc}) is the difference between the displacement reading after a load cycle and the displacement reading before the first cycle was applied. The accumulated displacements in Test E is shown in Figure 4.12. It can be observed that displacements accumulated faster in the first 10 cycles in all steps of Test E. The first cycles of step E-01 exhibited particularly large displacements compared with other steps ($U_{acc,N=10}$ = 5.89 mm). This may be due to the loose joints in the pile shaft or the loose condition of the soil above the helical plates caused by disturbance during the installation of the pile, i.e. the presence of voids above the plates caused by the pile rotating in place during installation. The first loading cycles densified the soil and increased its stiffness. As mentioned before, it should be noted that the application of an excessive load before E-02 also increased the stiffness of the soil and may have reduced the initial displacements of subsequent steps. Figure 4.12 also shows that both the initial (after the first 10 cycles) and the final accumulated displacements increase gradually from steps E-02 to E-05 in response to the combination of increasing mean and cyclic loading levels. The closeness between the curves from steps E-04 and E-05 is possibly due to their increased intersection with their previous steps, 37% and 53%, respectively.

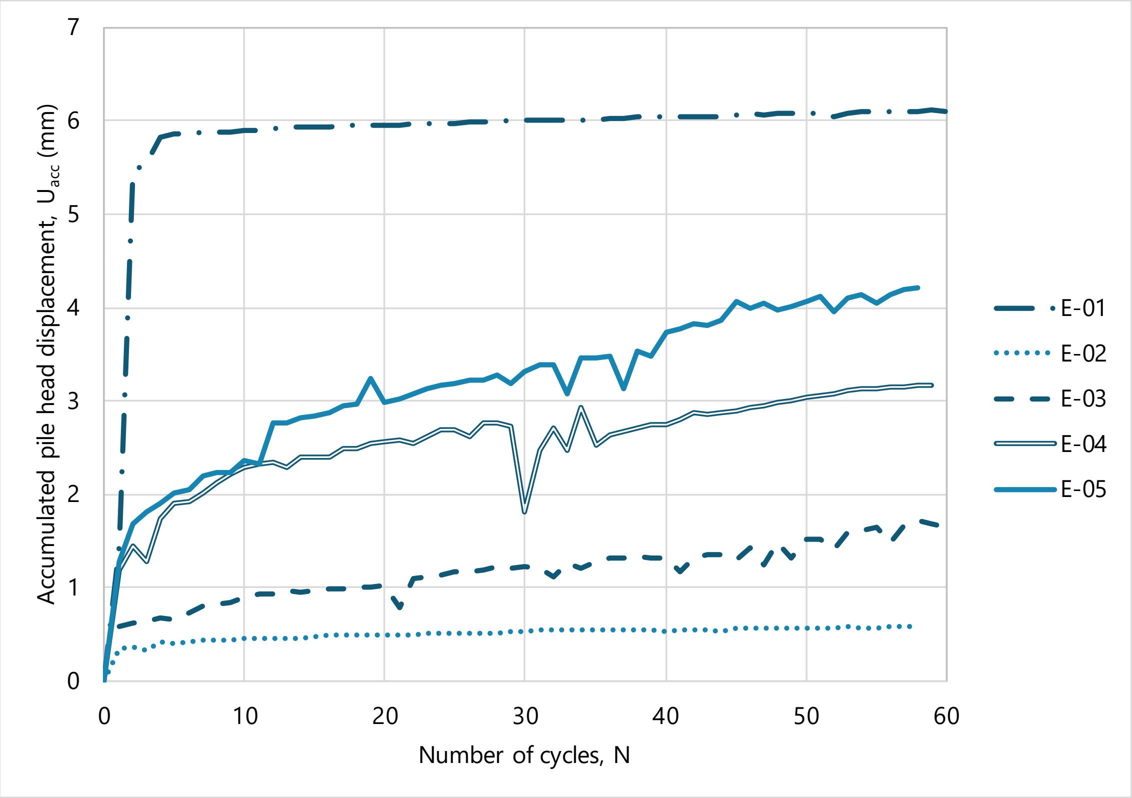

Figure 4.12 – Accumulated pile head displacements with number of cycles from Test E.

The results from the steps in Test G are presented in Figures 4.13a and 4.13b. Figure 4.13a includes the results of steps G-01 to G-04. The initial and final displacements recorded in steps G-02, G-03, and G-04 are similar, while the displacements in step G-01 are smaller. This behaviour is different from that of Test E and can be associated to the different loading path followed in the test. In Test G, the minimum load was kept constant and the maximum load was gradually increased. This resulted in steps G-02 to G-05 exhibiting intersection factors higher than 50%. Step G-05 reached much larger displacements and was removed from Figure 4.13a, so that the accumulation of displacements of the other previous steps. The results of step G-05 is shown in Figure 4.13b. Step G-05 had the highest cyclic average load associated with highest cyclic amplitude and exhibited initial and final accumulated displacements. Cyclic failure was defined as a permanent displacement equal to 10% of the average helix diameter. This criterion is similar to the one reported by Tsuha *et al.* (2012b). Step G-05 reached the failure condition before reaching 60 cycles.

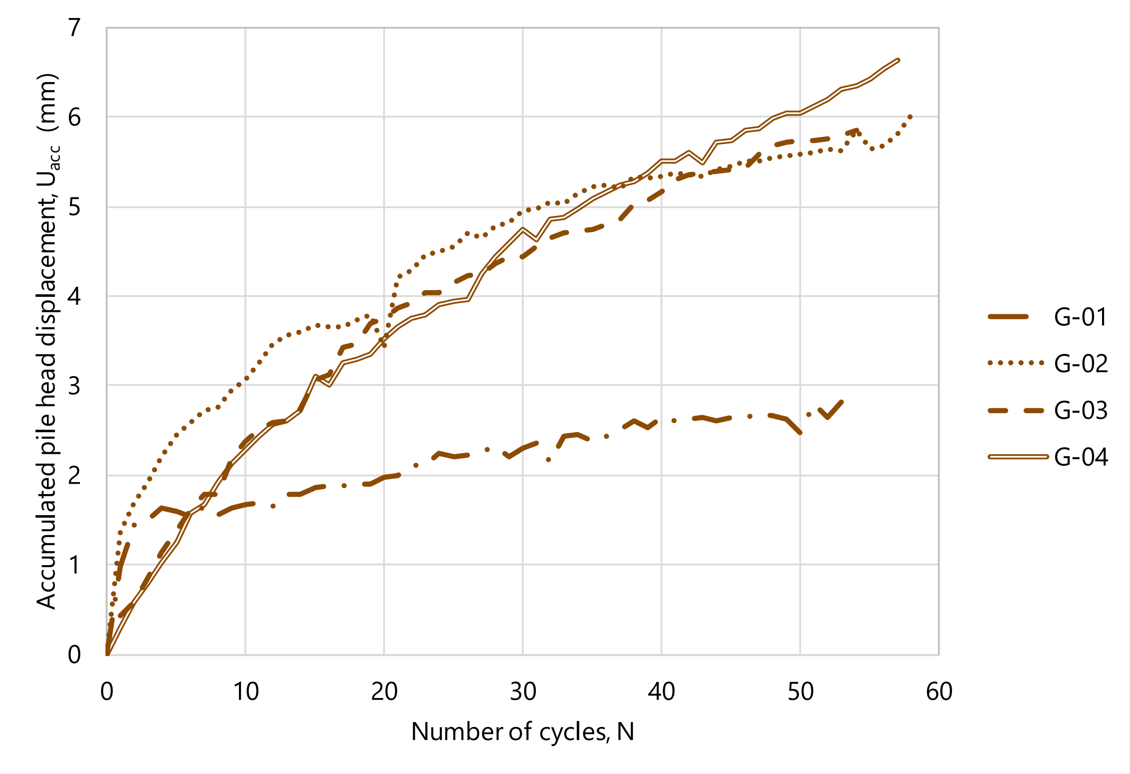

a)

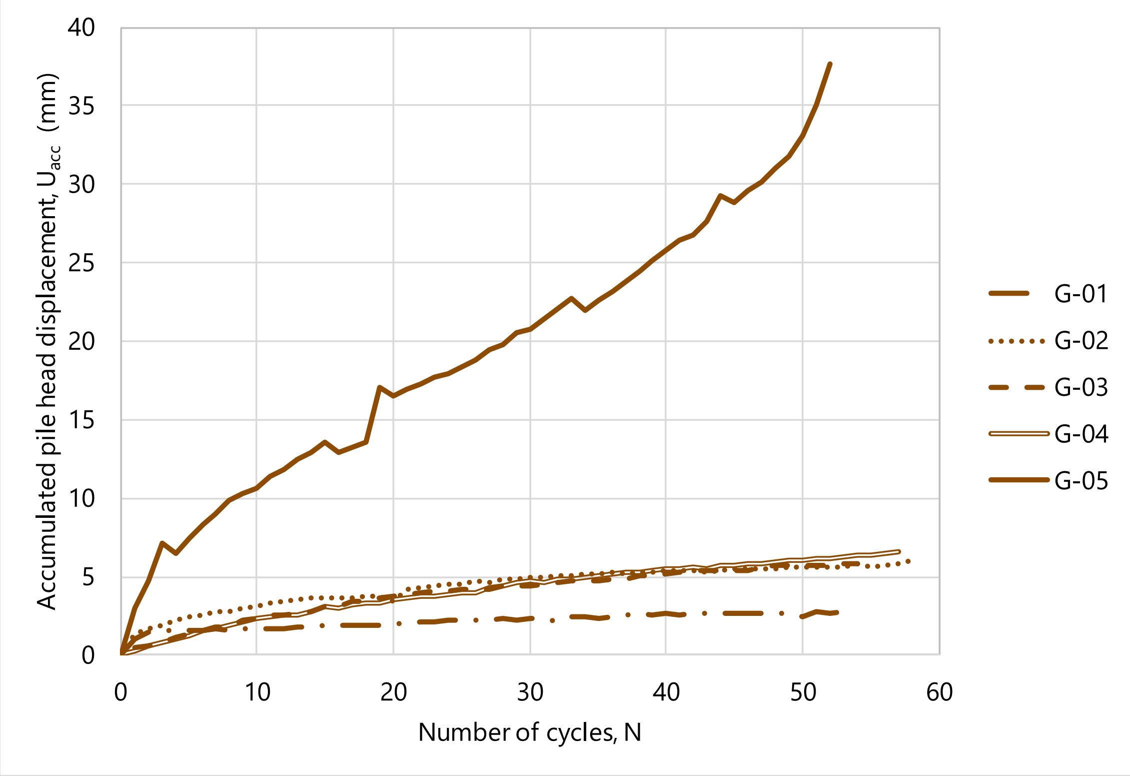

b)

Figure 4.13 – Accumulated pile head displacements with number of cycles from Test G: a) without step G-05; b) with step G-05.

4.4.2. Displacement accumulation rates and cyclic interaction diagram

Displacement accumulation rate is the difference between the displacement reading before and after a load cycle. After relatively large initial values, displacements start to accumulate more slowly and eventually reach a steady state. The displacements accumulated in the first 10 cycles ($U_{acc,N=10}$) and the mean displacement accumulation rate (V_{mean}) calculated for test E and G using Equation 4.2 is shown in Table 4.4.

Table 4.5 also shows the number of cycles before failure (N_f). In step G-05, the system sustained 46 cycles before failure. In the steps where failure was not observed, N_f was estimated from the displacement recorded after the first 10 cycles and the rate of displacement accumulation from the remaining cycles (Equation 4.3).

$$V_{mean} = \frac{U_{acc,N=n} - U_{acc,N=10}}{n-10} \tag{4.2}$$

Where: $U_{acc,N=n}$ = accumulated displacement after the last cycle; $U_{acc,N=10}$ = accumulated displacement after the 10th cycle; $(n-10)$ = number of cycles between the 10th cycle and the last cycle.

$$N_f = \frac{10\%\ D_{avg} - U_{acc,N=10}}{\mathrm{V}_{mean}} + 10 \tag{4.3}$$

Table 4.4 – Displacement accumulation, cycles before failure, and stability classification

Step	Q_{mean}/Q_T	Q_{cyclic}/Q_T	$U_{acc,N=10}$ (mm)	V_{mean} (mm/cycle)	N_f	Classification
E-01	0.08	0.02	5.89	4.40×10^{-3}	5484	Stable
E-02	0.16	0.05	0.46	2.72×10^{-3}	10855	Stable
E-03	0.25	0.06	0.90	16.5×10^{-3}	1770	Stable
E-04	0.33	0.08	2.30	18.1×10^{-3}	1544	Stable
E-05	0.40	0.11	2.36	39.1×10^{-3}	717	Meta-Stable
G-01	0.15	0.06	1.67	23.3×10^{-3}	1224	Stable
G-02	0.20	0.11	3.07	61.4×10^{-3}	448	Meta-Stable
G-03	0.25	0.16	2.37	80.5×10^{-3}	353	Meta-Stable
G-04	0.31	0.21	2.29	92.9×10^{-3}	308	Meta-Stable
G-05	0.44	0.33	10.6	644×10^{-3}	46	Unstable

The rate of displacement accumulation generally increases with the applied mean and cyclic load levels in both Test E and Test G. The rate from step E-02 is lower than that of step E-01, which may be explained by the load spike observed in Figure 4.10.

The calculated number of cycles was used to classify the stability of each step according to the stability criteria defined by Tsuha *et al.* (2012b), as described in item 2.9.3. Slow accumulation rates, smaller than 0.10×10^{-3} mm/cycle, were not achieved in the tests. In the steps classified as Stable, the rates ranged from 4.40×10^{-3} to 23.3×10^{-3} mm/cycle. All Meta-Stable and Unstable steps had fast accumulation rates, i.e. above than 10.0×10^{-3} mm/cycle. V_{mean} reached 92.9×10^{-3} mm/cycle in the Meta-Stable steps and 644×10^{-3} mm/cycle in the Unstable step. Displacements increased at fast rates when cyclic amplitudes higher than 20% of the static uplift capacity (Q_T) were used to load the pile. This took place in steps E-03, E-04, E-05, G-02, G-03, G-04, and G-05.

Figure 4.14 shows the cyclic loading parameters, normalized by the mean static uplift capacity, in the form of an interaction diagram. The tests were grouped in zones according to their stability class, shown in Table 4.5, following Karlsrud *et al.* (1986), Poulos, and Tsuha *et al.* (2012b).

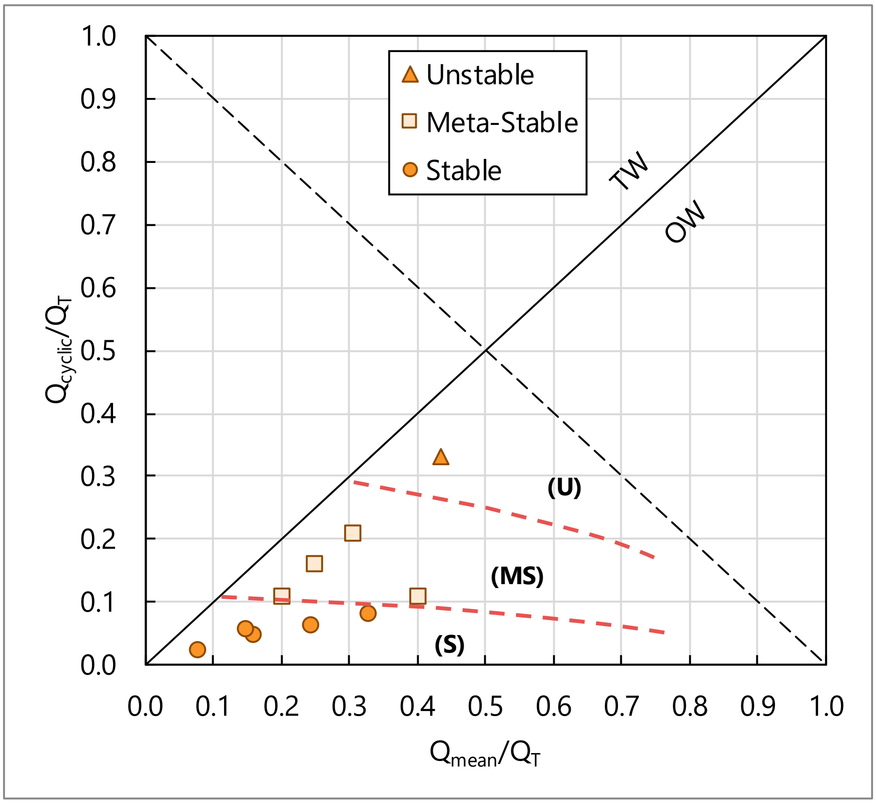

Figure 4.14 – Axial cyclic interaction diagram with results from test E and G.

The diagram of Figure 4.14 shows that the stability of a test depends on both the normalized cyclic amplitude and the normalized mean load. All tests with Q_{cyclic}/Q_T < 0.10 are located within the Stable region of the chart, indicating that these tests would take more than to 1000 cycles before reaching failure condition. This can be confirmed by the slow displacement accumulation rates.

The last step performed in Test E, E-05, and the three intermediate steps performed in Test G, G-02, G-03, and G-04, are classified as Meta-Stable. All four steps were performed with 0.10 < Q_{cyclic}/Q_T < 0.30. This is in agreement with the displacement accumulation rates calculated for those steps.

In the last step of Test G, G-05, the pile head reached a displacement of 30 mm after 46 cycles and the step can be classified as Unstable.

Tests with the same mean load can fail in different ways depending on the cyclic amplitude. For example, steps E-03 and G-03 have the same mean cyclic load, Q_{mean}/Q_T = 0.25, but cyclic amplitude, Q_{cyclic}/Q_T, of the latter is 2.7 times that of the former. Step E-03 is classified as Stable and sustains four times more cycles before failure than G-03, which is classified as Meta-Stable. The effect of the mean load can be found by comparing the steps E-05 and G-02. The normalized cyclic amplitude of both steps is 0.11 but the mean load acting on E-05 is twice that on G-02. Both are classified as Meta-Stable but the estimates show E-05 can sustain 61% more load cycles the G-02.

4.4.3. Cyclic stiffness

The reference secant stiffness (k_{ref}) value obtained from Test A, shown in item 4.3.3, is used in this item to evaluate the stiffness response of the piles under quasi-static cyclic loading. The loading cyclic stiffness (k_L) and the unloading cyclic stiffness (k_U) parameters, established by Rimoy *et al.* (2013) and illustrated in Figure 4.15, are also used in the analyses.

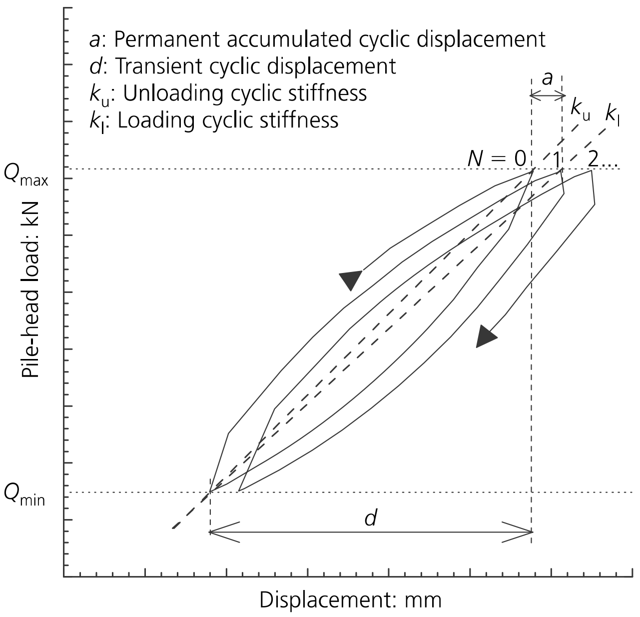

Figure 4.15 – Illustration of cyclic stiffness and displacement parameters used in analyses (Rimoy *et al.*, 2013).

Figure 4.16 shows the loading cyclic stiffness values from each cycle of all steps normalized by the reference stiffness calculated from the first loading in Test A ($k_L/k_{ref,A}$). The values were normalized to simplify comparisons between the two tests. Test A was chosen because it is representative of the average response obtained with the static tests.

The results of Test E are shown in Figure 4.16a. In step E-01, k_L starts at 50% of the value of $k_{ref,A}$, which indicates that the state of the soil around the plates is more disturbed than the observed in Test A. This can be confirmed by the large displacements observed during this cycle. In the same figure, it can be observed that the load stiffness values decrease as the cyclic loading parameters are increased from steps E-02 to E-05. The initial stiffness observed in step E-02 is four times the value of $k_{ref,A}$. In steps E-03 and E-04, the initial $k_L/k_{ref,A}$ values decrease to 3 and 2, respectively. The initial $k_L/k_{ref,A}$ value of step E-05 was 2 and was probably affected by the higher load amplitude used in the cycles from the previous step.

The normalized stiffness calculated from the steps of Test E tends to stay stable after increasing in the first cycles. The mean stiffness values after the first 10 cycles also tend to decrease with increasing mean and amplitude loading levels. The mean stiffness in the last cycles of step E-01 is 16 times higher than $k_{ref,A}$. The mean normalized stiffness increases in step E-02 to 31.7 and decreases in the following two steps, E-03 and E-04, to 11.5 and 6.0, respectively. A small change is observed in the last step, E-05, when mean normalized stiffness increases to 6.6. The higher intersection between the loads from the last two steps may have caused the stiffness increase in step E-05.

The results of Test G are shown in Figure 4.16b. The behaviour observed in G-01 is opposite to that of E-01. The initial normalized stiffness ratio in the first cycle was 1.8, which indicates that the disturbance during pile installation was lower than in Test E and that the minimum load kept during the step, which was twice that used in Test E-01, served to increase the relative stiffness of the soil and to tighten shaft connections. The initial normalized stiffness decreased to 0.7 in the following step, G-02, probably due to the disturbance caused by the previous cycle. In step G-03, initial normalized stiffness increases to 1.1. The parameter decreases slightly to 1.0 in step G-04. In the final step, G-05, the initial relative stiffness decreases again to 0.8, due to the non-linear behaviour of the stiffness around the soil when loads approach the static capacity of the pile, as observed in the static tests (item 4.3.3).

The steps in Test G show the same stabilizing trend observed in the steps in Test E. However, in the case of Test G, the mean normalized stiffness values of each step are close to each other. For steps G-01 to G-05, the mean values observed after the first 10 steps are 3.3, 3.3, 3.7, 4.0, and 3.8, respectively. The different behaviour may be associated with the different cyclic loading parameter used in the test and the higher intersecting loads between steps, as shown in Table 4.4.

Figure 4.16b also shows that the normalized stiffness starts to gradually decrease after cycle 49 of step G-05, which could indicate cyclic failure. In item 4.4.2 it was observed that failure occurred after cycle 46 according to the criterion used by Tsuha et al. (2012b). The similarity between the results validates the use of the criterion in the present work.

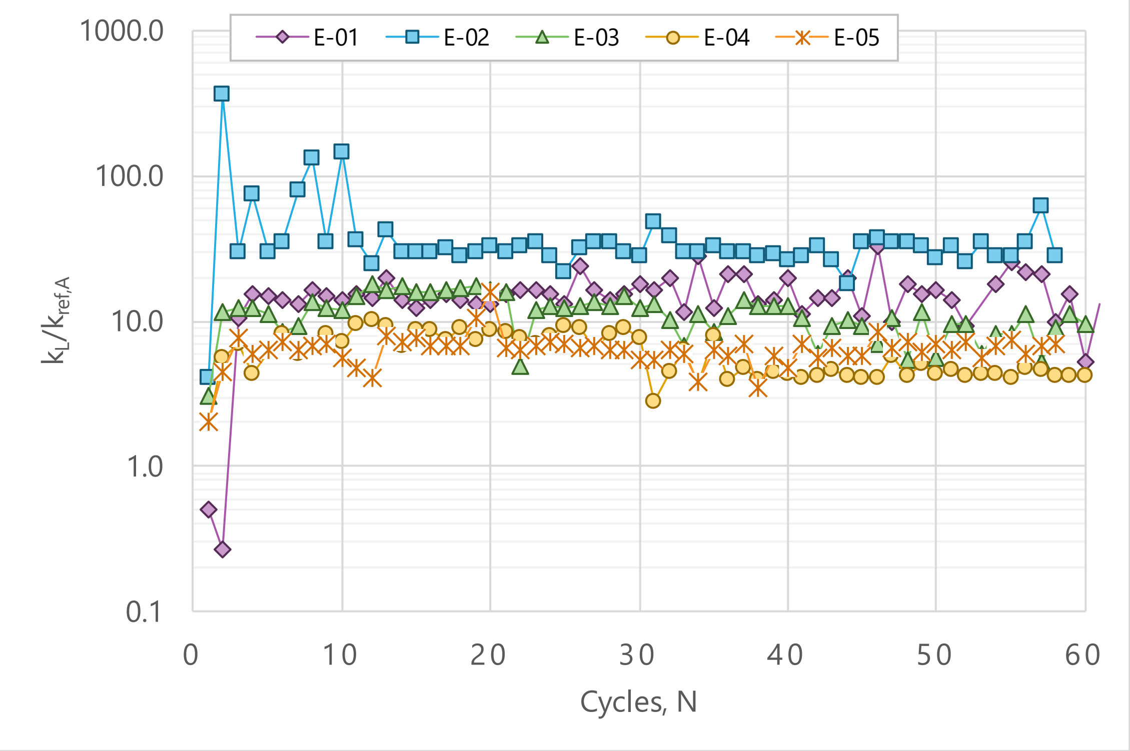

a)

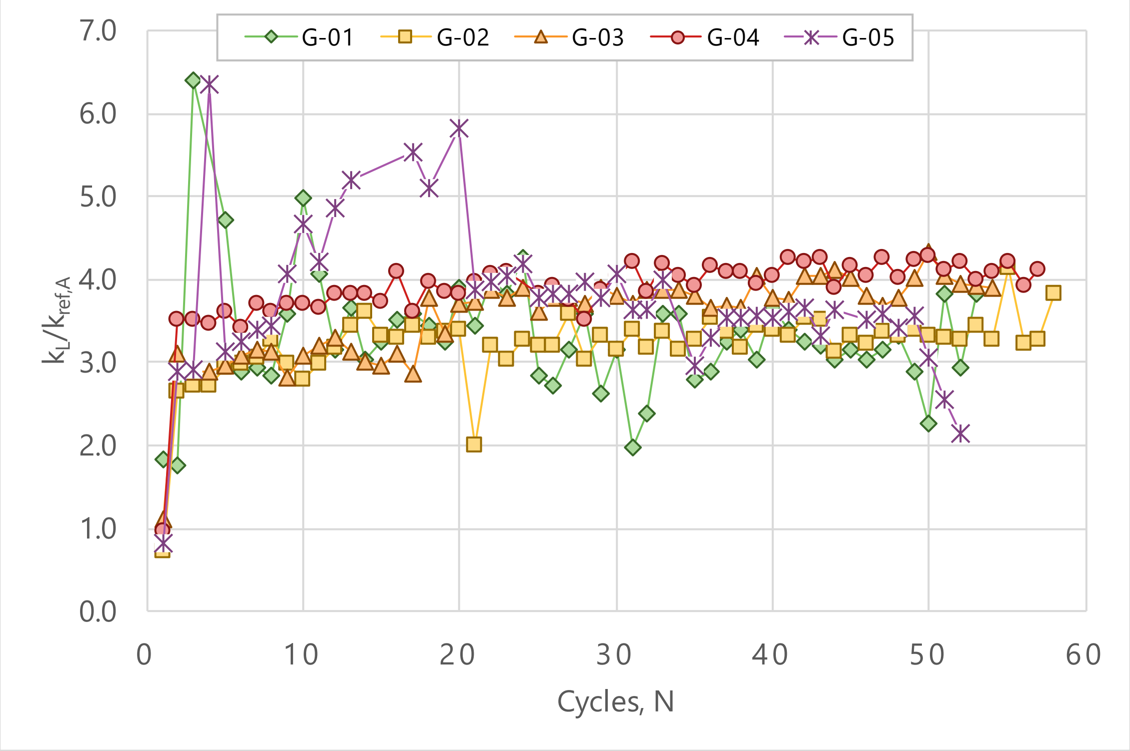

b)

Figure 4.16 – Axial cyclic loading stiffness (k_L) responses normalized in terms of $k_{ref,A}$, plotted against number of cycles: a) Test E; b) Test G.

Figure 4.17 shows the loading cyclic stiffness values from each cycle of all steps normalized by the stiffness calculated from the first cycle of each step ($k_L/k_{L,(N=1)}$). Using the initial stiffness from each step enables comparisons between the values observed in the same step. As observed in Figure 4.16, in general, stiffness tends to increase after the application of the first few cycles and then stabilize around a value.

The results of Test E are shown in Figure 4.17a. Step E-01 shows the largest stiffness gains of all steps, with a mean $k_L/k_{L,(N=1)}$ value of around 30. This high increase is due to the initial loose, disturbed state of the soil after installation. Step E-02 also showed slightly small stiffness gains, with $k_L/k_{L,(N=1)}$ between 7 and 9 during most of the step. The mean $k_L/k_{L,(N=1)}$ values of steps E-03, E-04, and E-05 are 3.8, 3.1, and 3.3, respectively.

The results of Test G are shown in Figure 4.17b. The average increase in stiffness caused by loading cycles in step G-01 was 80%, much smaller than the observed in E-01. The $k_L/k_{L,(N=1)}$ values of steps G-02 to G-04 stabilized between 3 and 5. In step G-05, in which cyclic failure occurred, $k_L/k_{L,(N=1)}$ rose to 7 after 20 cycles, then decreased to around 5 during the following 25 cycles, and fell to below 3 after the last three cycles.

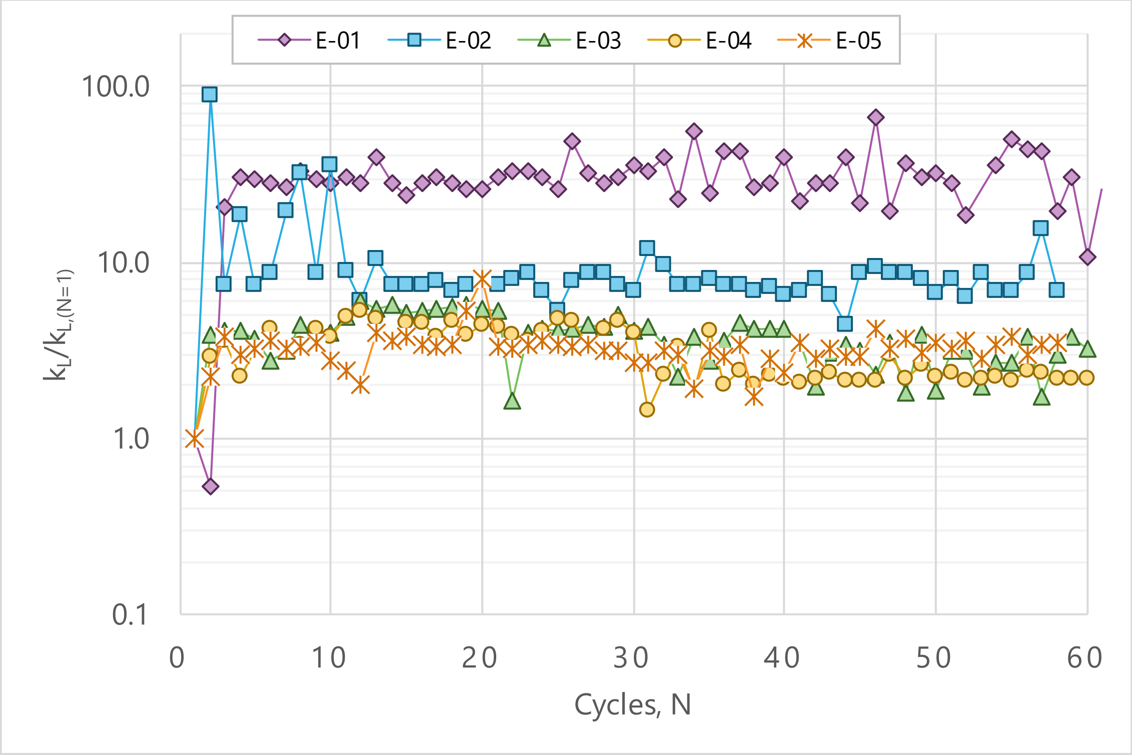

a)

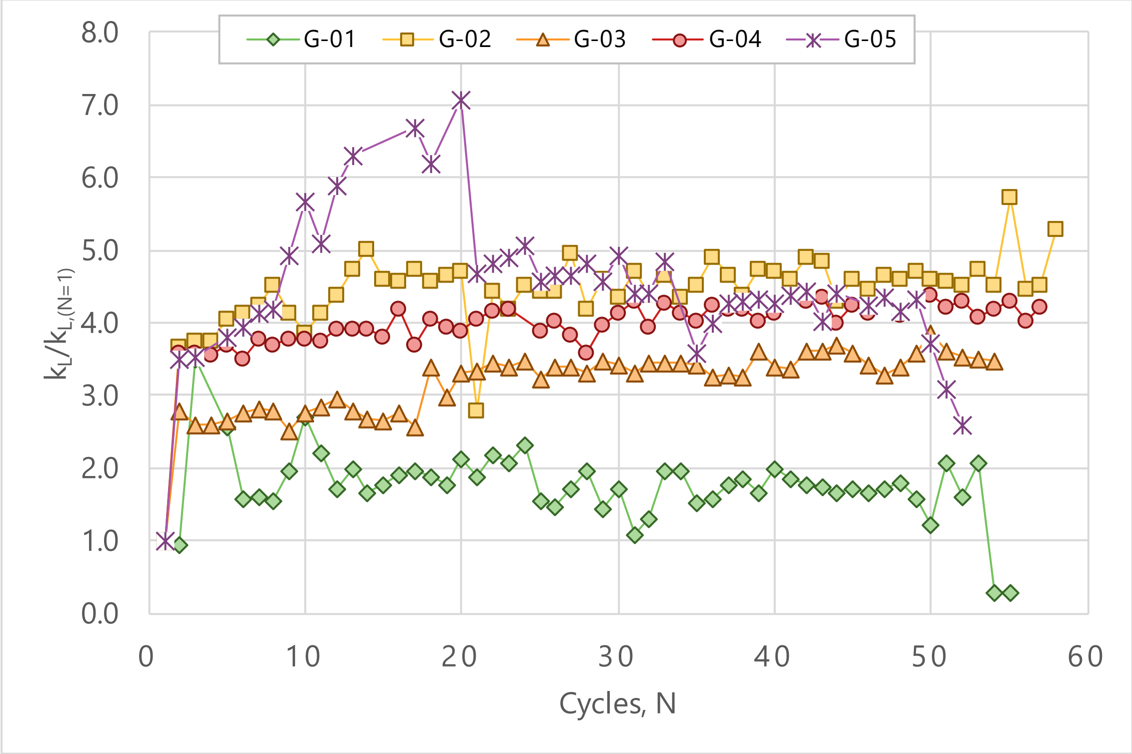

b)

Figure 4.17 – Axial cyclic loading stiffness (k_L) responses normalized in terms of $k_{L,(N=1)}$, plotted against number of cycles: a) Test E; b) Test G.

The behaviour of the unloading cyclic axial stiffness (k_U) is shown in Figure 4.18a and 4.18b for Test E and Test G, respectively. The data is normalized by the reference stiffness, $k_{ref,A}$, obtained from the first step of Test A.

The relative unloading stiffness ($k_U/k_{ref,A}$) measured in the first cycle of step E-01 is smaller than the reference stiffness. This behaviour was observed during the loading stage of the same cycle and can also be associated with soil disturbance caused by installation and initial looseness in the loading system. Unloading stiffness in step E-01 increases after few cycles and stays relatively constant until the end of the cycles, with a mean value of 14.5, close to the mean value obtained from the step during the loading stage. This is a sign that the application of cycles increases the stiffness of the soil. The initial unloading stiffness in step E-02 is 32 times higher than the loading stiffness, possibly caused by the load spike before the step. The stiffness in this step also stabilizes quickly, falling to the same levels observed during the loading stage. The initial relative unloading stiffness of steps E-03, E-04, and E-05, are 13.4, 9.5, and 8.2. These values are about 4.5 times higher than their loading counterparts. They also stabilize after the first cycles and reach values that are similar to those observed during loading.

In Test G, higher mean and cyclic loading levels resulted in small increases in the unloading stiffness values. Relative stiffness values during unloading obtained from the first cycle of steps G-01 to G-05 increased from 3.2 to 4.7. These values are about four times higher than their loading equivalents but very close to the mean loading stiffness values after stabilization. The stabilization trend can also be observed in the steps of Test G, but the mean unloading stiffness values of the final cycles are only slightly lower than the initial values and are also close to the mean stiffness values during loading.

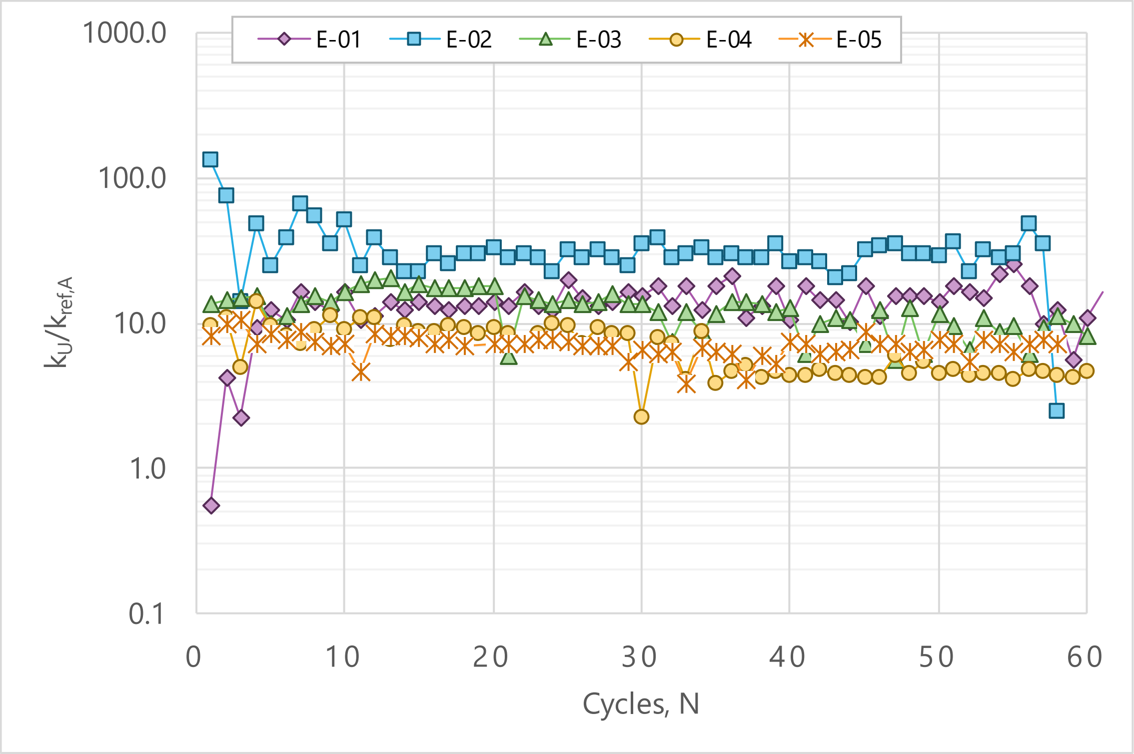

a)

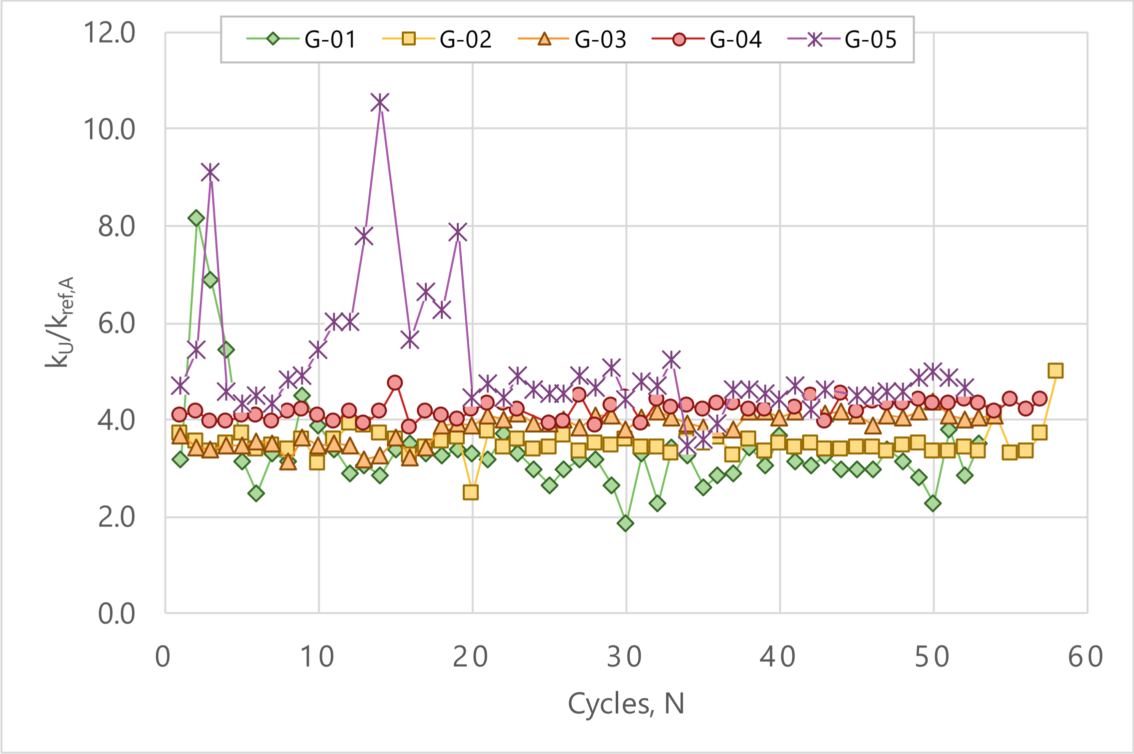

b)

Figure 4.18 – Axial cyclic unloading stiffness (k_U) responses normalized in terms of $k_{ref,A}$, plotted against number of cycles: a) Test E; b) Test G.

The plots of cyclic axial stiffness during unloading normalized by the initial unloading stiffness of each step ($k_U/k_{U,(N=1)}$) are shown in Figures 4.19a and 4.19b for Test E and Test G, respectively. Unloading stiffness values obtained from the steps of tests E and G tend to stabilize quickly at values that are close to the initial stiffness of each step. Steps E-01 and E-02 are exceptions.

Figure 4.19a shows that normalized unloading stiffness in step E-01 increases to about 26 times its initial value after less than 10 cycles. The opposite is observed in the following step. The unloading stiffness of step E-02 starts at a high absolute level and decreases quickly. In relative terms, after 10 cycles, unloading stiffness in step E-02 decreases to 23% of its initial value. In the following steps, E-03, E-04, and E-05, load cycles caused small decreases in unloading stiffness, which reached 92%, 67% and 83% of their initial values, respectively.

The relative unloading stiffness of the steps in Test G remained mostly stable, with variations of ±10% around the initial value.

Overall, the unloading stiffness observed in the first cycles of all steps is three to five times higher than the stiffness parameter during loading. After a few cycles, the unloading stiffness tends to show degradation and reach the same values as the loading parameter.

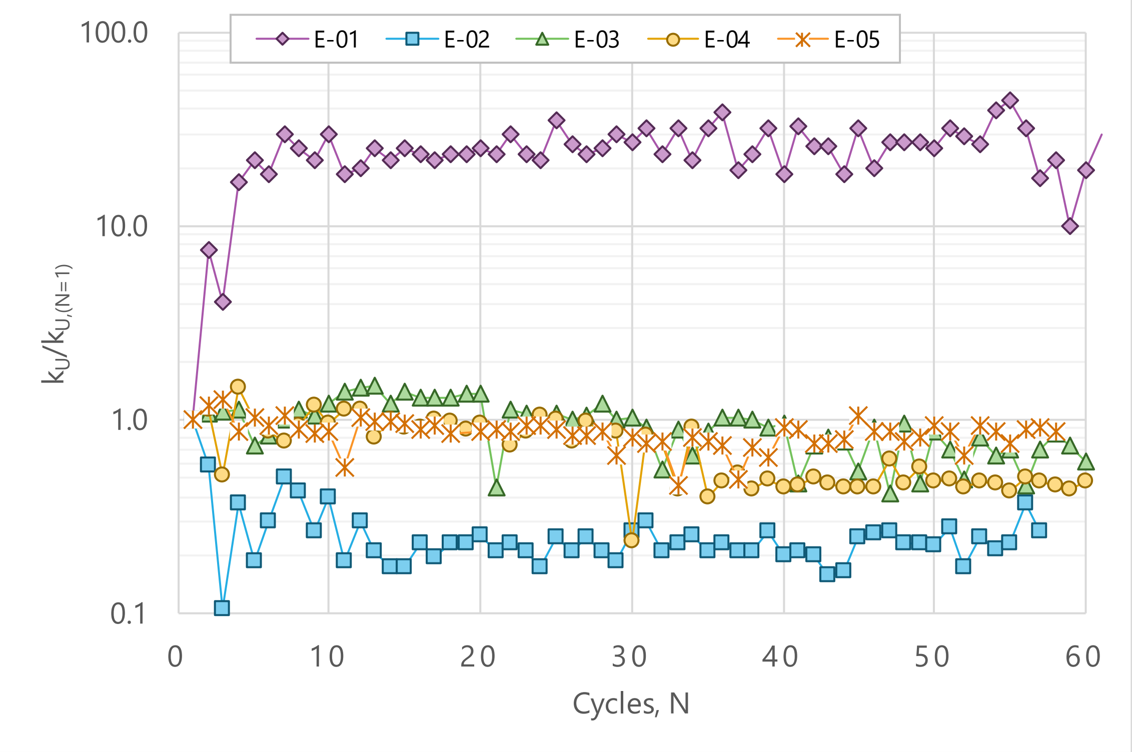

a)

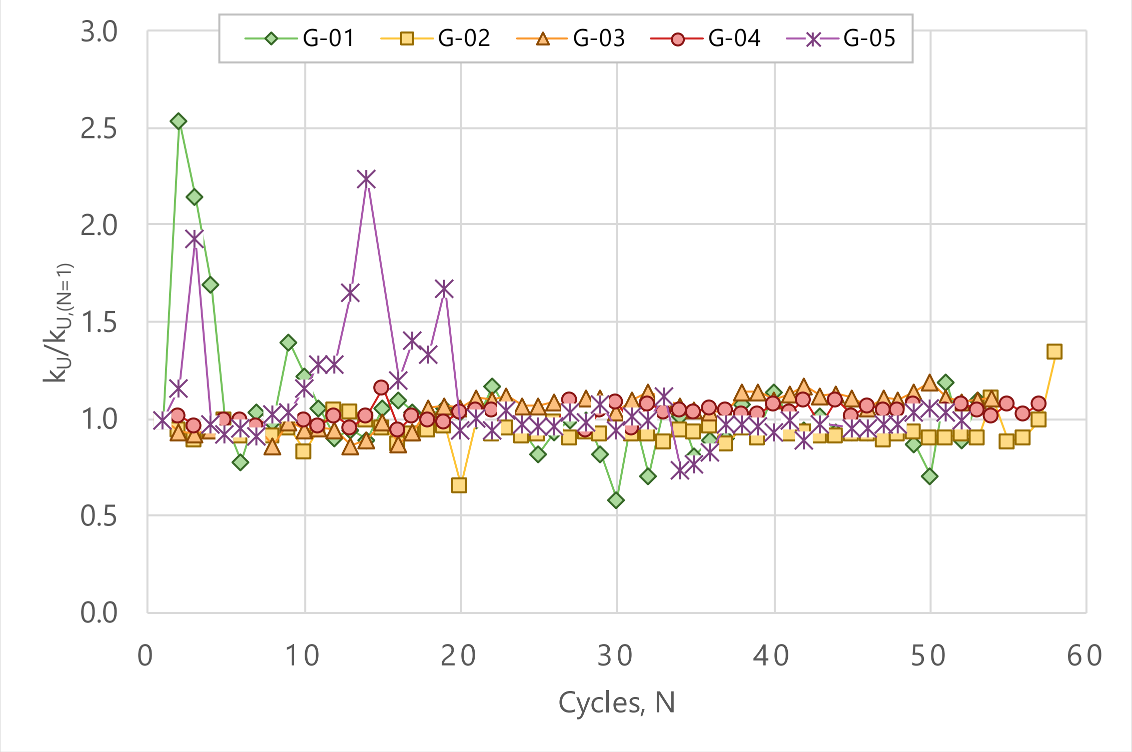

b)

Figure 4.19 – Axial cyclic unloading stiffness (k_U) responses normalized in terms of $k_{U,(N=1)}$, plotted against number of cycles: a) Test E; b) Test G.

Table 4.5 shows a summary of the mean stiffness parameters obtained after the 10th cycle from each step. When comparing all steps from the two tests, it is possible to observe that the mean normalized stiffness values during loading ($\overline{k_L/k_{ref}}$) and unloading ($\overline{k_U/k_{ref}}$) are very similar to each other and generally tend to decrease with increasing Q_{cyclic}/Q_T. The normalized stiffness values of Stable steps are generally higher than those in the Meta-Stable steps. The normalized stiffness parameters in the Unstable step are close to those Meta-Stable steps. Increasing cyclic loading levels caused a reduction in stiffness between the Stable and Meta-Stable steps. This indicates that the different behaviour between the Stable and Meta-Stable classes is related to changes in stiffness. No significant changes in stiffness were observed between the Meta-Stable and Unstable steps. This shows that increasing cyclic loading parameters in steps located in Meta-Stable zone tends to cause stiffness to stabilize, after initially decreasing from the levels observed in the Stable steps. The large displacements achieved in the Unstable zones are more related to high mean and cyclic load levels than to stiffness degradation, at least until cyclic failure. As noted previously, significant and continuous decreases in stiffness were only observed in the Unstable step G-05 when it approached the cyclic failure condition.

Table 4.5 also shows that the mean loading stiffness values (k_L) from all steps are higher than the initial values ($k_{L,(N=1)}$). In most cases, loading stiffness increased by a factor between 3 and 5. Regarding unloading stiffness (k_U), minor changes were observed in most steps. This behaviour is expected and can also be observed in Figures 4.3 to 4.5, where the stretch of the load-displacement curves during unloading, the slope of which correspond to k_U, are almost parallel to each other.

Table 4.5 – Mean axial cyclic stiffness parameters normalized in terms of k_{ref} and $k_{(N=1)}$

Step	$\boldsymbol{Q_{mean}/Q_T}$	$\boldsymbol{Q_{cyclic}/Q_T}$	$\overline{\boldsymbol{k_L/k_{ref}}}$	$\overline{\boldsymbol{k_U/k_{ref}}}$	$\overline{\boldsymbol{k_L/k_{L,(N=1)}}}$	$\overline{\boldsymbol{k_U/k_{U,(N=1)}}}$	**Classification**
E-01	0.08	0.02	16.0	14.5	32.0	26.0	Stable
E-02	0.16	0.05	31.7	29.0	7.85	0.23	Stable
E-03	0.25	0.06	11.5	12.3	3.81	0.92	Stable
E-04	0.33	0.08	6.03	6.35	3.10	0.67	Stable
G-01	0.15	0.06	3.26	3.09	1.78	0.97	Stable
G-02	0.20	0.11	3.31	3.51	4.56	0.94	Meta-Stable
G-03	0.25	0.16	3.72	3.93	3.33	1.07	Meta-Stable
E-05	0.40	0.11	6.61	6.80	3.29	0.83	Meta-Stable
G-04	0.31	0.21	4.01	4.24	4.09	1.03	Meta-Stable
G-05	0.44	0.33	3.83	5.08	4.65	1.08	Unstable

4.4.4. Post-cyclic static response

After Test E was performed, the pile was immediately subjected to a new static load test in the same installation, Test F. The purpose was to evaluate the effect of previous cyclic loads on the static capacity of the pile. After the five steps of cycles in test E, the load was removed and the pile was reloaded until the last maximum cyclic load. Test F was performed with 10-minute load increments, until failure occurred at a load of 204 kN; This failure load is designated here as the post-cyclic capacity, $Q_{T,pc}$, and was obtained following the same criteria used for obtaining the field failure loads of static tests A, B, C, and D (item 4.3.1).

The load-displacement curve from the static load test is shown in Figure 4.20. It can be observed that the cyclic loadings caused a significant increase in stiffness of the soil above the helical plates, resulting in small displacements in the first 120 kN of loading and an increase in ultimate capacity of 11 kN as compared to the average ultimate capacity of the static load tests. This represents an improvement of 6% in Q_T.

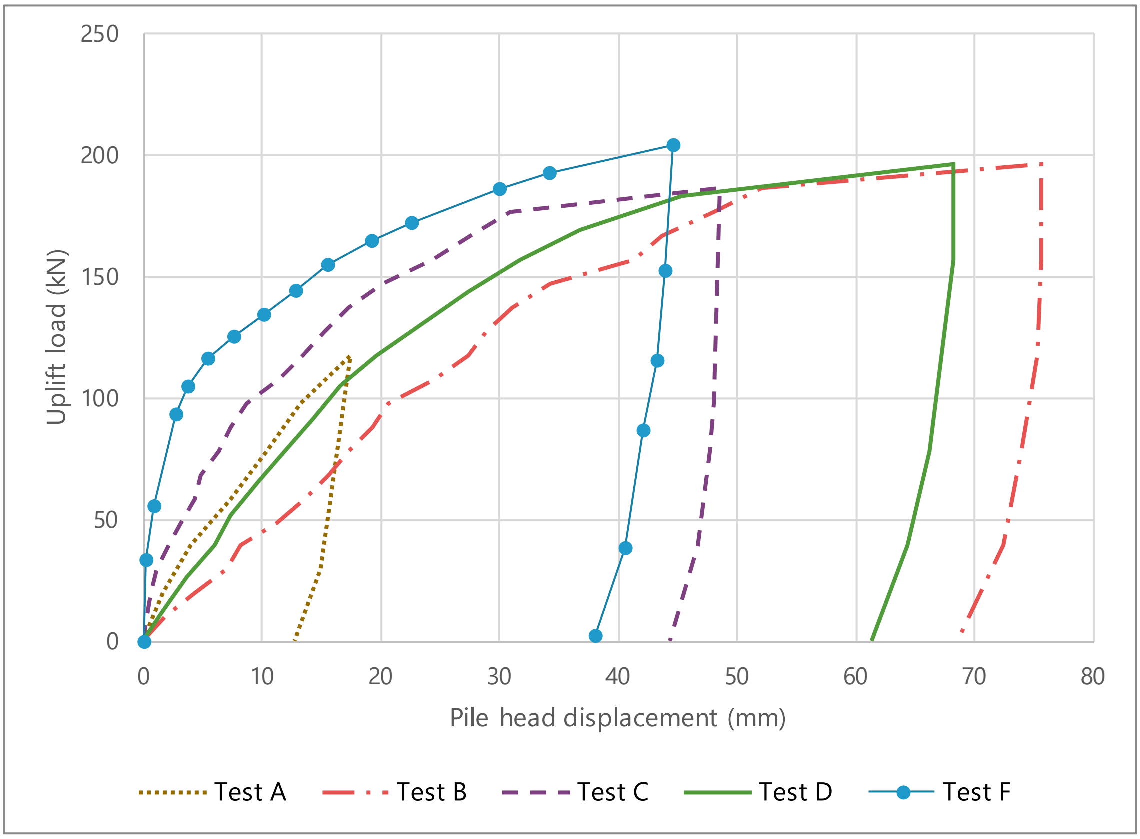

Figure 4.20 – Load-displacement response of Test F along the envelopes from previous static tests.

The normalized maintained mean load, $Q_{mean}/Q_T = 0.40$, and the normalized maximum cyclic load applied to test E, $Q_{max}/Q_T = 0.51$, were smaller than the values observed by Schiavon (2016) in the piles that exhibited gains in post-cyclic capacity, which were Q_{mean}/Q_T > 50% and $Q_{max}/Q_T > 0.80$.

Equation 2.22, developed by Schiavon (2016) to predict post-cyclic capacity, was used in the present study with the loading parameters of the last cyclic step and predicted a decrease of 4% in capacity. The equation was originally created for dense sands and its prediction error suggests its use in less dense sands is inadequate, although more tests would be required to confirm this.

4.5. Numerical modelling of the static loading tests

4.5.1. Model calibration

A numerical model of the static load tests performed on the prototype pile was developed using Plaxis 2D 2016 according to the procedures described in item 3.5. The numerical model was based on the geometrical properties of the field tests and on the materials properties shown in Tables 3.6 and 3.7. Preliminary simulations were performed to adjust the input parameters. After adjustments of the parameters, numerical simulations were performed individually for each static field test. The responses obtained with the numerical model were quite similar to the corresponding field results. The good agreement between the responses is partly due to the used of the "Hardening Soil" material model, which reproduced with high accuracy the progressive elastic-plastic behaviour observed in the experimental results. The numerical curve obtained for Test A is compared with the experimental curves in Figure 4.21. The numerical curves obtained for the other tests are omitted in Figure 4.21 for clarity.

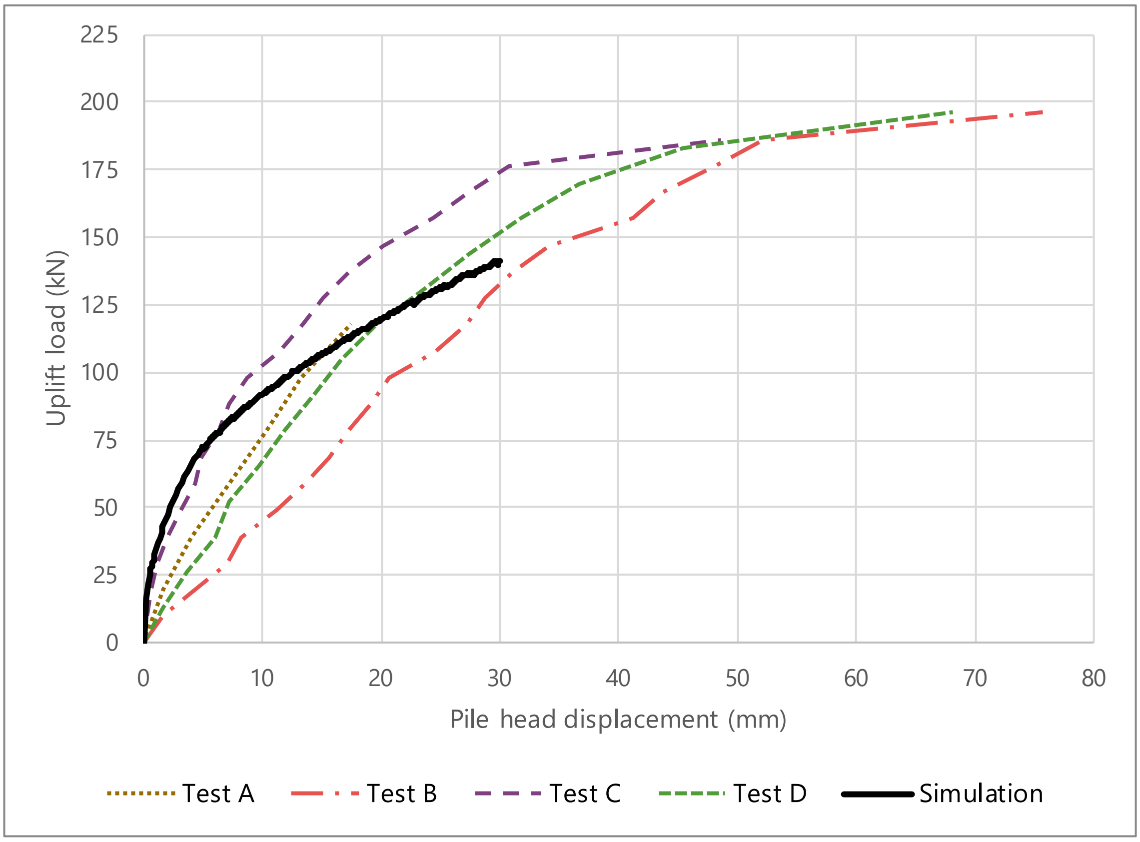

Figure 4.21 – Load-displacement response from field tests and from the numerical simulation.

The modified Davisson criterion, described in item 2.8.3, was used to provide the ultimate uplift capacity obtained from the numerical model. The obtained values are close to their corresponding field values. The obtained values are close to their corresponding field values. The numerical and field bearing capacity values are compared in Table 4.6.

Table 4.6 – Ultimate capacities from field tests and numerical simulations.

Test	$Q_{u,modDav}^{field}$ **(kN)**	$Q_{u,modDav}^{Plaxis}$ **(kN)**	$Q_{u,modDav}^{field}/Q_{u,modDav}^{Plaxis}$
A	-	141	-
B	138	137	1.00
C	177	131	1.35
D	156	142	1.11

Note: $Q_{u,modDav}^{field}$ = field ultimate uplift capacity obtained using the modified Davisson criterion; $Q_{u,modDav}^{Plaxis}$ = simulated ultimate uplift capacity obtained using the modified Davisson criterion.

Figure 4.22 shows the vertical displacements, the vertical normal stresses and the shear strains inside the soil mass for the conditions of test A, with $Q_{u,modDav}^{Plaxis}$ = 141 kN. It can be observed that the depth of installation in Test A, 2.57 m, which corresponds to an embedment ratio H_1/D_1 = 7.3, was sufficient to prevent the developed failure surfaces from reaching the ground surface. Such behaviour is referred to as deep anchor condition in the literature (Das, 1990; Perko, 2009).

Figure 4.22a shows that displacements concentrate more within the cylindrical zone representing the soil disturbed by the passage of the plates during installation. The displacements caused by the movement of the upper helix reached a vertical height above it equal to about 3 helical plate diameters.

Figure 4.22b shows that the top and the bottom helical bearing plates are subjected to high stresses and the middle plate is only moderately loaded. Between both helices, the top helix was much more loaded than the bottom helix. A possible explanation for the lower loading of the middle helix is that the relative free space above the top and lower helices is higher than that of the middle one. The relative free space is the free space above each helix divided by their diameter. In the case of the top helix, the parameter is the same as its embedment ratio (H_1/D_1 = 7.3). In the middle and lower helices, the parameter is equal to their spacing ratios (s_2/D_2 = 2.5 and s_3/D_3 = 3.0). This indicates that the spacing between the middle and the top helices was not sufficiently large to allow the full development of the failure mechanism in the middle helix. According to Lutenegger (2011), the transition between individual plate behaviour and cylindrical shear behaviour in sand occurs at a spacing ratio of about 3. The value is also considered as standard by the pile manufacturing industry (Hubbell Power Systems, 2014). Large spacing ratios allow the plates to develop their capacity individually, as is the case of the bottom helix.

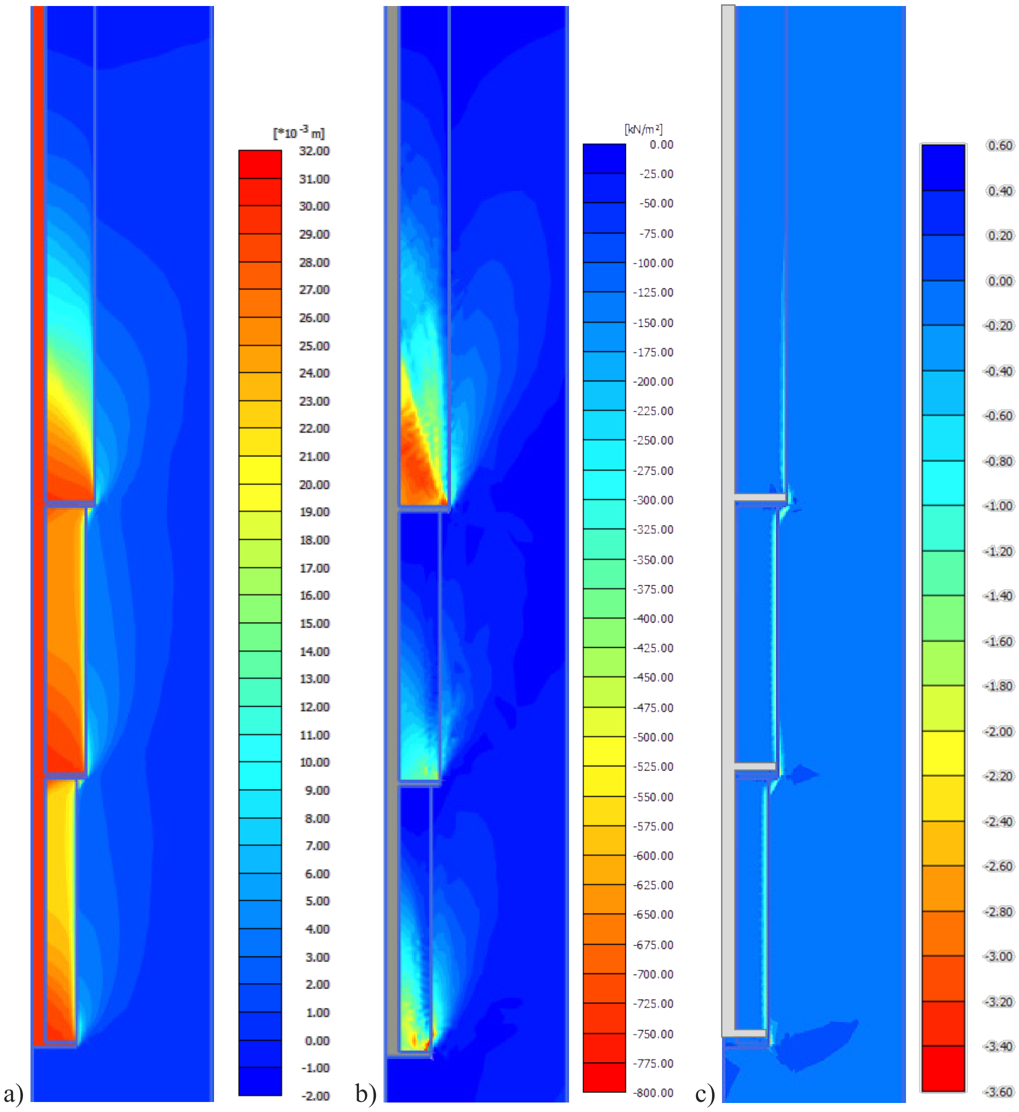

Figure 4.22 – Numerical simulation of Test A at failure load: a) vertical displacements; b) vertical effective stresses; c) accumulated shear strains.

As can be observed in Figure 4.22c, the shear strains in the lower and intermediate plates extend from the top of the plates to the bottom of the immediately superior plates. Zones of shearing left the edges of the top helix and extend up to a height approximately equal to three times the top helix diameter. The shearing does not reach the surface, confirming the deep anchor behaviour. Shear strains above the three helices are distributed around the zone created by the passage of the plates during installation, indicating that the load capacity mechanism of all helices in the field was developed inside the cylindrical surface that limits the zone containing material disturbed by the installation of the helical pile.

4.5.2. Parametric analyses

Parametric analyses were also performed with the developed numerical model. The objective of the parametric analyses is to understand how variations in the design parameters affect the pile uplift capacity and the distribution of loads and stresses around the pile, and to find the optimum configuration for this specific studied case. The ultimate uplift capacity was determined according to the modified Davisson criterion (ICC-ES, 2007), with $Q_{u,modDav}^{field}$ equal to the load reached at a net displacement of 10% of D_{avg}.

4.5.2.1. Relative embedment ratio

In this analysis, the numerical model based on the prototype pile used in the field tests was simulated using relative embedment (or depth) ratios, H_1/D_1, ranging from 1.43 to 14.3. The ultimate uplift capacity obtained from the results is plotted in Figure 4.23. The uplift capacity was found to improve with increasing embedment ratios. Increases in uplift capacity higher than 40% can be observed when the depth ratio is increased by 100%. Zhang (1999) observed increases in tension capacity of around 90% when increasing the embedment ratio by 130%.

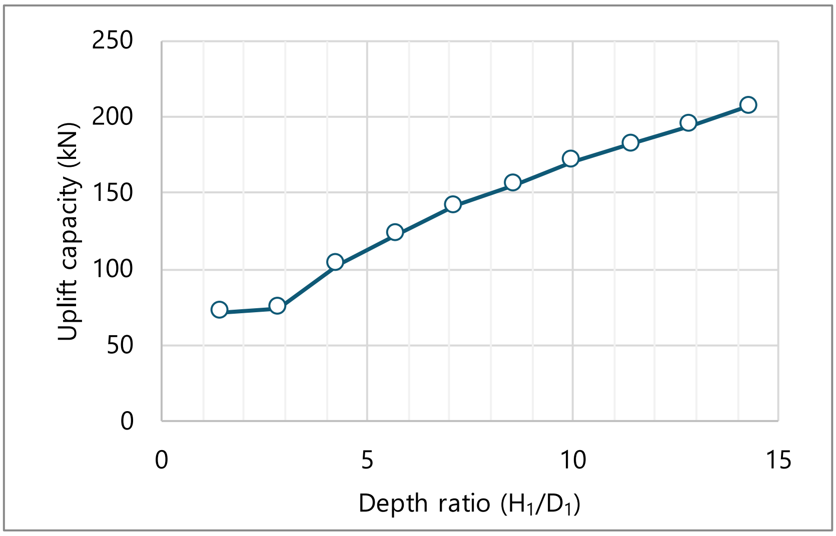

Figure 4.23 – Parametric analysis: relative embedment ratio.

Vertical displacements inside the soil mass are shown in Figure 4.24 and are used to assess the transition between shallow and deep failure modes as the embedment ratio is increased. In simulations in which the depth ratio was smaller than 4 (Figures 4.24a and 4.24b), displacements extend up to the ground surface, indicating the top helix behaves as a shallow anchor. The gain in uplift capacity is mostly due to the increased weight of the soil in the cylinder above the top helix. The larger depth ratios represented by Figures 4.24c, 4.24d and 4.24e result in the displacements caused by the movement of the top helix no longer reaching the surface. This feature indicates deep anchor behaviour. Most of the gains in uplift capacity achieved with larger embedment ratios are due to the increased confinement of the soil around each bearing plate.

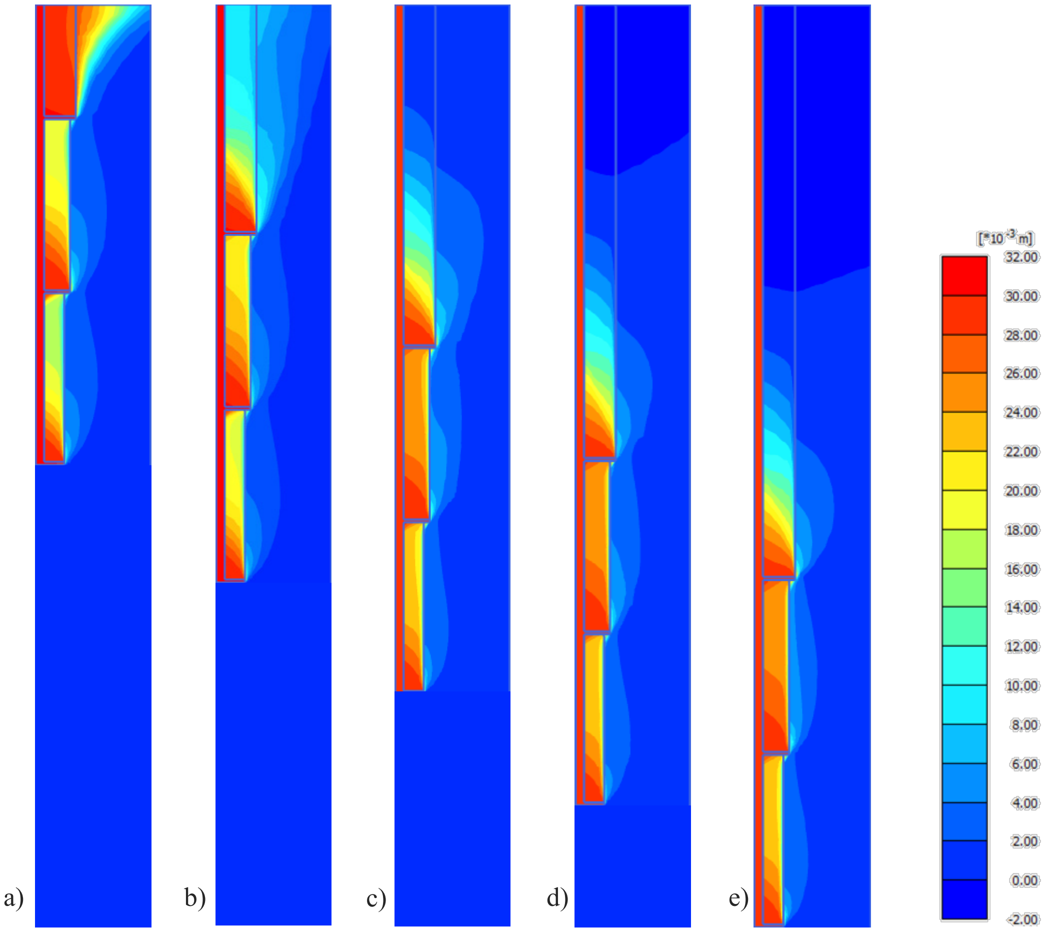

Figure 4.24 – Vertical displacements in piles installed at different depths: a) H_1/D_1 = 1.43; b) H_1/D_1 = 2.9; c) H_1/D_1 = 4.3; d) H_1/D_1 = 5.7; and e) H_1/D_1 = 7.1.

The transition between shallow and deep behaviours occurs with an embedment ratio around 4. The same value was estimated by Perko (2009) as the minimum embedment ratio for loose, coarse-grain soil. Das (1990) proposed a chart to determine the critical value of H_1/D_1 for which the transition between shallow and deep behaviour take place in cohesionless soils. The ratios obtained from the chart for sands with internal friction angles equal to those exhibited by the sand investigated in the present study, φ' = 32° in looser conditions and φ' = 36° in denser conditions, are 4.4 and 6.3, respectively. According to Mitsch and Clemence (1985), the critical H_1/D_1 is equal to 5.

4.5.2.2. Helical plate diameter

Variations in the diameter of the plates were simulated in two ways. Piles with uniformly sized plates were simulated first and the ultimate capacity obtained from the tests is shown in Figure 4.25a. Then, piles with tapered plates (i.e., diameters decreasing with increasing depth) were simulated and the results are shown in Figure 4.25b. The piles are represented by the sum of the net area of their plates, A_t, i.e. the gross area of the plate minus the area occupied by the pile shaft. All piles use the relative embedment ratio of Test A, $H_1/D_1 = 7.3$, and all plates have the same inter-helix spacing ratio, $s_i/D_i = 3$. Tables 4.7 and 4.8 summarize the uniform and tapered plate configurations, respectively, along with the total effective areas and their corresponding capacities.

Table 4.7 – Plate configurations and uplift capacity: uniform configuration

$D_1 = D_2 = D_3$ (mm)	A_t (cm^2)	$Q^{Plaxis}_{u,modDav}$ (kN)
200	817	56
225	1067	71
250	1347	86
275	1656	116
300	1995	140
325	2363	176
350	2761	206
375	3188	239
400	3644	278

Table 4.8 – Plate configurations and uplift capacity: tapered configuration

D_1 (mm)	D_2 (mm)	D_3 (mm)	A_t (cm^2)	$Q^{Plaxis}_{u,modDav}$ (kN)
150	200	250	856	59
175	225	275	1107	77
200	250	300	1386	98
225	275	325	1696	124
250	300	350	2034	150
275	325	375	2402	180
300	350	400	2800	221
325	375	425	3227	252
350	400	450	3684	296

It can be observed that increase in uplift capacity with plate area is virtually linear. The data from Tables 4.7 and 4.8 are plotted in Figures 4.25a and 4.25b, respectively, along with linear fittings were adjusted to the points of curves and their corresponding equations.

Figure 4.25c compares the uplift capacity obtained according to both configurations. The different between the two results is negligible. Tapered configurations are expected to provide higher capacities because they generate less disturbance in the ground during installation. (Tsuha *et al.*, 2013). However, the numerical models used in the present work were not able to reliably reproduce the effect of many levels of disturbance.

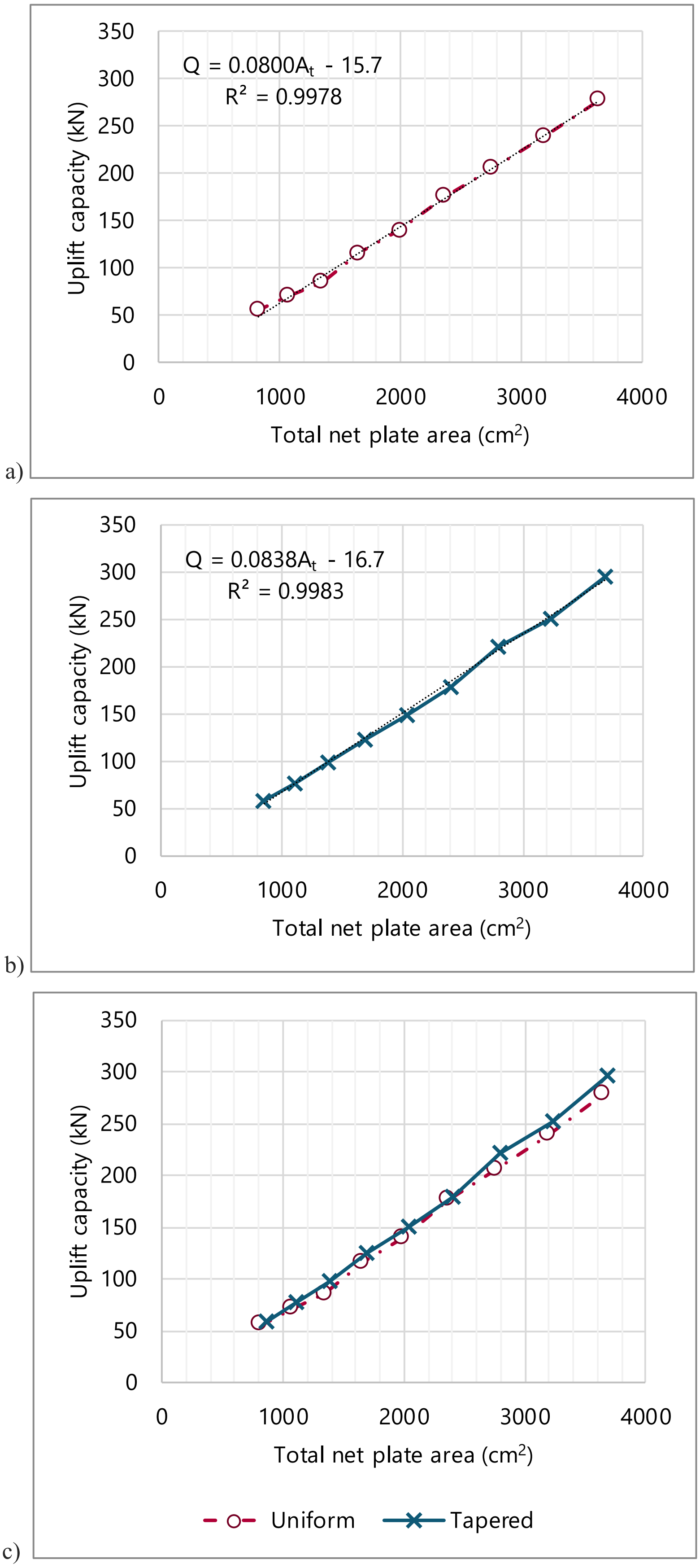

Figure 4.25 – Uplift capacity as a function of helical plate diameter: a) piles with uniform helices; b) piles with tapered helices; c) comparison between both configurations.

4.5.2.3. Inter-helix spacing

Inter-helix spacing ratio (s_i/D_i) is the spacing between two consecutive helical bearing plates divided by the diameter of the lower helix. Ratios between 2 and 5 were simulated, with 0.5 intervals between them. The helix sizes of prototype pile (350-300-250 mm) were used in this simulation. All piles were set with the same installation depth, H_4 = 4.08 m. The ultimate uplift capacities obtained in this analysis are shown in Figure 4.26. Increasing the relative spacing between plates results in gains in uplift capacity until the s_i/D_i reaches 4.0. Further increases in spacing ratio reduces the uplift capacity.

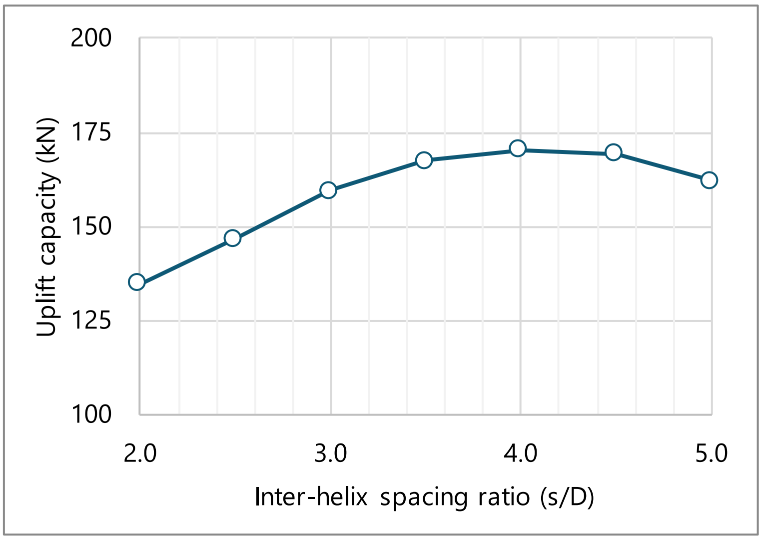

Figure 4.26 – Uplift capacity as a function of inter-helix spacing ratio (s_i/D_i).

Figure 4.27 shows the distribution of accumulated shear strain in the soil with increasing spacing ratios. The shear strain in the two lower ratios (Figures 4.27a and 4.27b) starts from the lower plates and reaches the upper plates, revealing a cylindrical shear failure mechanism. A different behaviour can be observed in models with larger s_i/D_i values. With higher spacing ratios, shear strains start to concentrate closer to the helices, indicating that failure mechanism of the system is partly provided by the individual capacity of the plates (Figures 4.27d to 4.27g). Even with large relative spacing, the strains still reach the upper helices, however with less intensity. The presence of shear strains extending to the upper helices in piles in these cases can be associated to the lower strength of the soil in the disturbed zone. The test with s_i/D_i = 3.0 (Fig. 4.27c) represents the transition from cylindrical shear to individual capacity mechanisms. The result is consistent with optimal spacing ratio used in industry practice (A.B. Chance, 2014). Lutenegger (2011) also observed this transition with the same spacing ratio.

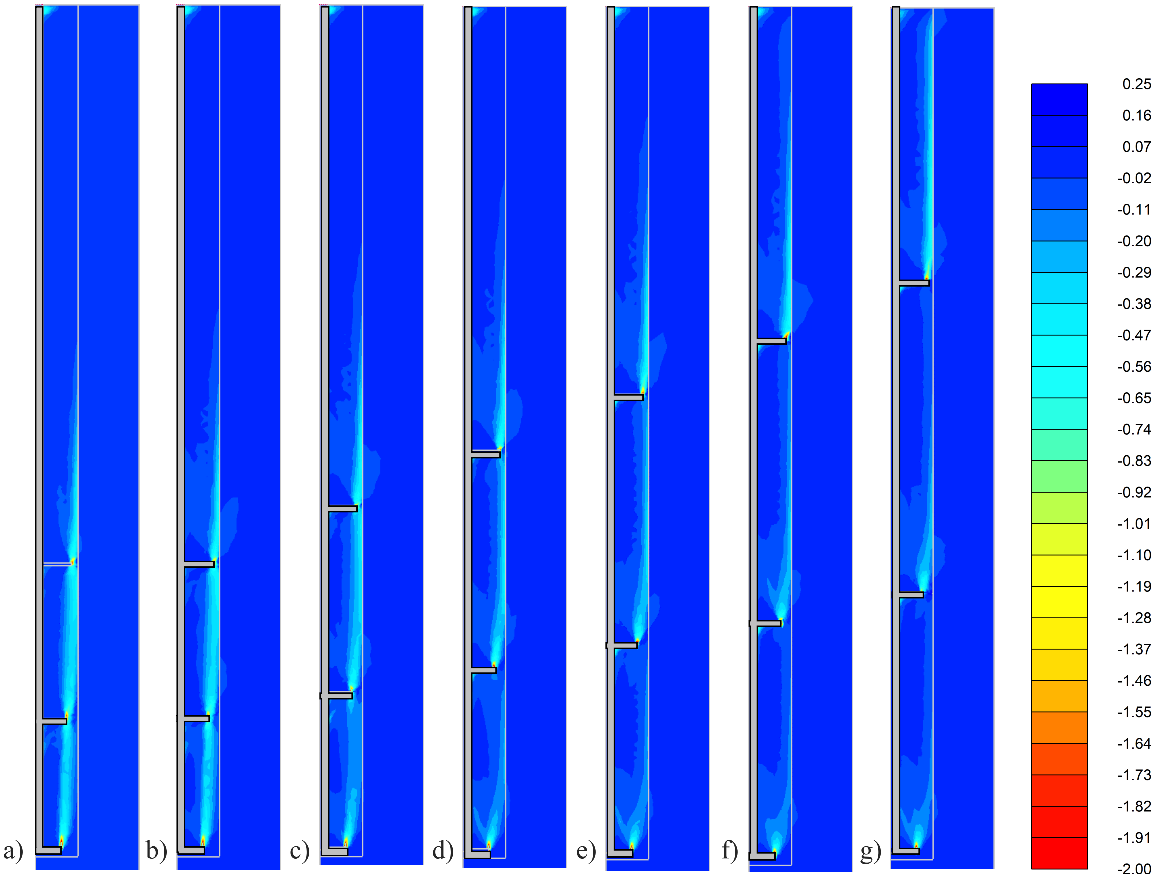

Figure 4.27 – Shear strains in the soil mass with increasing spacing ratios: a) s_i/D_i = 2.0; b) s_i/D_i = 2.5; c) s_i/D_i = 3.0; d) s_i/D_i =3.5; e) s_i/D_i = 4.0; f) s_i/D_i = 4.5; and g) s_i/D_i = 5.0.

Figure 4.28 shows the vertical stresses developed in the soil mass with increasing spacing ratios. In Figures 4.28a and 4.28b, the stresses acting on the top helical plate are clearly higher than the stresses acting on the two lower plates, indicating the failure mechanism of the two lower plates is not fully developed. That is, the load acting on the two lower helices is being resisted by the shear stresses developed around the surface of the cylinder formed around between the uppermost and the lowermost plates, as observed in Figure 4.27. Stresses on other piles (Figures 4.28c to 4.28e) are more evenly distributed between the plates, indicating that their individual capacities are more developed. This means the load transfer mechanism occurs individually and not along a cylindrical shear surface. The stresses on the top helix in Figures 4.28f and 4.28g are lower than that of the other two helices, showing that increasing the spacing ratio without increasing depth reduces the embedment ratio of the top helix, causing the reductions in uplift capacity observed in Figure 4.26.

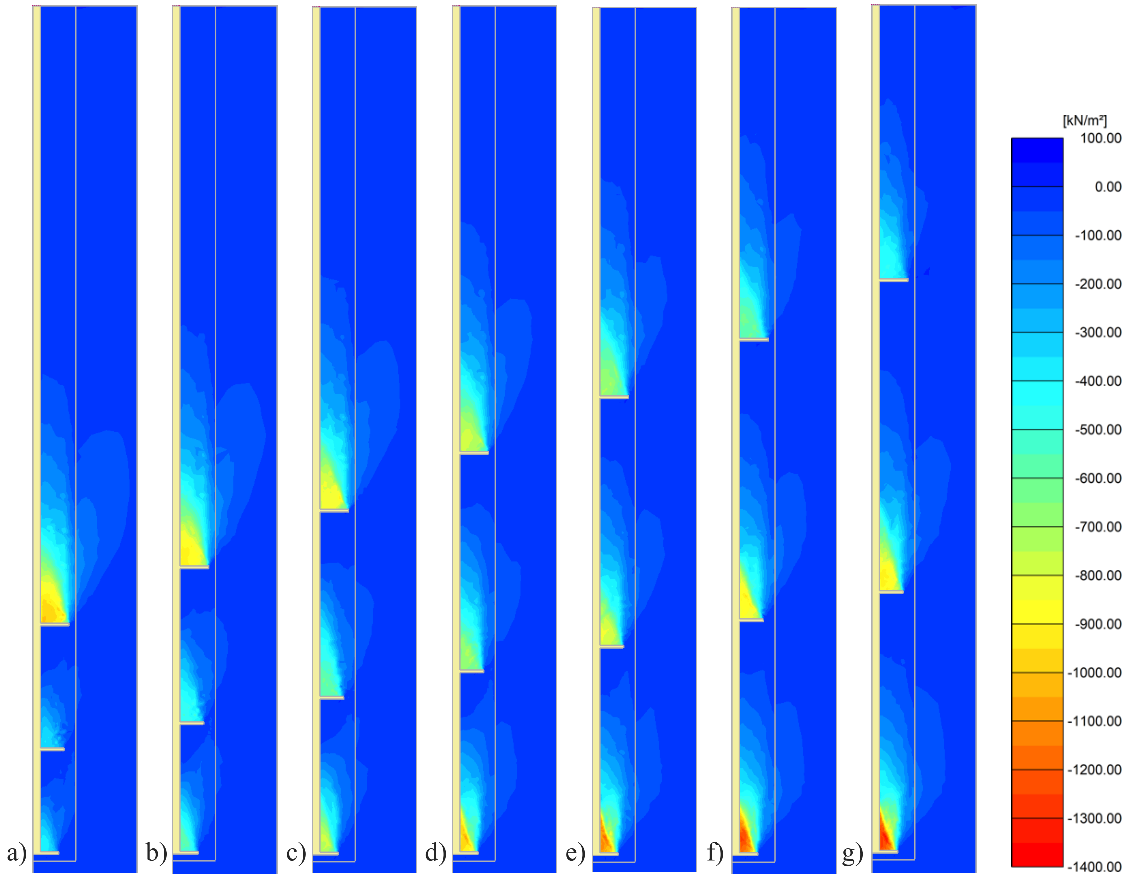

Figure 4.28 – Vertical stresses in the soil mass with increasing spacing ratios: a) s_i/D_i = 2.0; b) s_i/D_i = 2.5; c) s_i/D_i = 3.0; d) s_i/D_i =3.5; e) s_i/D_i = 4.0; f) s_i/D_i = 4.5; and g) s_i/D_i = 5.0.

4.5.2.4. Number of helices

Simulations using one to four helical plates were also performed. They used the prototype helix sizes (250 mm, 300 mm, and 350 mm) and an additional helix with diameter equal to 400 mm with s/D = 3 and H_1/D_1 = 7.3 . A summary of the performed simulations is shown in Table 4.9.

Figure 4.29 shows the uplift capacities obtained from configurations (d), (e), (f), and (g), with 1, 2, 3, and 4 helical plates, respectively. The corresponding sum of individual uplift capacities obtained from configurations (a), (b), (c), and (d) is also plotted. It can be observed that using the recommended inter-helix spacing ratio of 3.0, which is supposed to prevent interaction between the plates, the uplift capacities of helical piles are not equal to the sum of the capacities of individual plates. For example, in the configuration with two plates, the computed capacity of the associated plates, configuration (e), is 31% smaller than the sum of the individual plates (configurations (d) and (c)). The disturbance caused by the installation process, which was simulated using zones with weaker material, is a probable cause of this effect. The problem of efficiency was studied by Lutenegger (2011). According to the author, efficiency decreases with increasing number of helices and is more noticeable with smaller spacing ratios.

Table 4.9 – Simulations of effect of number of helices

Config.	**Number of plates**	D_4 (m)	H_4 (m)	D_3 (m)	H_3 (m)	D_2 (m)	H_2 (m)	D_1 (m)	H_1 (m)	Q_u (kN)
a	1	-	-	-	-	-	-	400	2.92	106
b	1	-	-	-	-	350	3.97	-	-	114
c	1	-	-	300	4.87	-	-	-	-	104
d	1	250	5.62	-	-	-	-	-	-	94.4
e	2	250	5.62	300	4.87	-	-	-	-	144
f	3	250	5.62	300	4.87	350	3.97	-	-	205
g	4	250	5.62	300	4.87	350	3.97	400	2.92	259

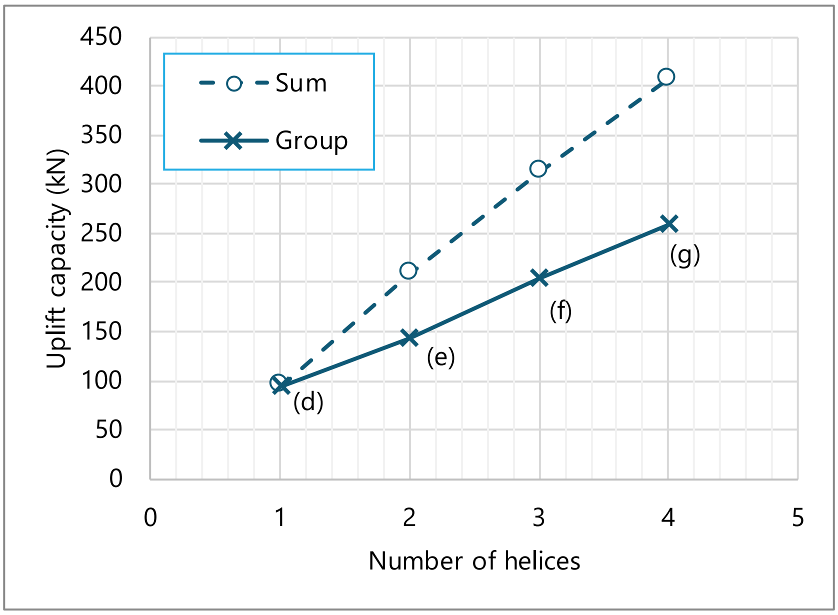

Figure 4.29 – Uplift capacity as a function of the number of helical plates.

5. CONCLUSION

5.1. Summary and conclusions

This research presents an evaluation of the behaviour of helical piles installed in a pure sand deposit of eolian origin. Static and quasi-static axial load tests were performed in a construction site located in Natal, Brazil. A numerical model was developed based on the experimental results and was used to investigate the effects of specific design parameters on pile behaviour.

A helical steel pile prototype was designed and built with three bearing plates with diameters decreasing rom the top to the tip of the pile. An adapted drilling machine was used to install the pile in different locations in the test site.

Four static tensile load tests were performed after the installation. The loads were applied in loading-unloading cycles with increasing maximum loads until plunging failure of the helical plates was observed. The results show that the piles failed around the same load, 193 kN, usually after the pile head had reached a displacement greater than 30 mm.

Comparisons were stablished between the ultimate uplift capacities obtained from the experimental results and from predictions based on theoretical methods. The individual bearing method gave the closest predictions to the actual results. Results from this method were slightly underestimated. Analysis of the load-displacement curves from the static tests show that stiffness tends to increase after each loading cycle. The response observed in one test with 15 load-unload cycles revealed that this stiffening effect is greater in the first few cycles.

Two tensile load tests were performed with quasi-static loading cycles. Each test was conducted in five steps. During the steps, the minimum loads were kept constant or increased and the maximum loads were increased, resulting in increasing mean cyclic loads and cyclic amplitudes in both cases. Increasing average load and cyclic amplitude resulted in large accumulated displacements and large rates of displacement accumulation. Cyclic stability showed high dependency on both cyclic amplitude and mean cyclic load. Quasi-static tests include stable, meta-stable and unstable steps. Stable loadings were achieved with cyclic amplitudes below 10% of the static uplift capacity. Unstable loading was reached with cyclic amplitude above

30% of the static uplift capacity. Meta-stable loading was achieved with cyclic amplitudes between 10% and 30% of the static uplift capacity.

Axial loading and unloading stiffness of the soil-pile system were calculated for each cycle. In stable and meta-stable loading, loading cyclic stiffness tended to increase in the first few cycles and then stabilize. In unstable loading, the stiffness tended to decrease after an initial decrease.

In the second test, which included medium cyclic load amplitudes, axial loading stiffness increased with increasing load amplitudes. Within a range of low loading amplitudes, increases in amplitude led to reductions in loading stiffness. On the other hand, within a range of medium loading amplitudes loading stiffness increased with increasing amplitude.

The first quasi-static test was followed by a static load test. The previous cyclic loadings caused an overall improvement in axial stiffness and a small improvement in ultimate uplift capacity.

A numerical model was developed to simulate the static load tests. The model was validated against the load-displacement responses from the field tests. The numerical results showed good agreement with the experimental results. The output from the finite element software enabled a look into the stresses and strains inside the soil mass and indicated that the developed failure mechanism was characterized by large loading of the top and the bottom plates and by shearing in the cylindrical surface formed between the middle and the top plates.

Parametric analyses were carried out to investigate the effect of specific design parameters on the pile response. Uplift capacity increased with depth of installation in a nearly linear fashion. Uplift capacity increased by 40% as the depth ration of the upper helix (H_1/D_1) was doubled. It was observed that piles installed with a depth ratio below 2.9 failed as shallow anchors, while deep anchor mode was achieved with piles installed with depth ratios greater than 4.3.

Pile uplift capacity showed a virtually linear increase with increasing plate diameter, in both uniform and tapered configurations. Comparisons were made for piles with same net plate are. Uplift capacity was basically the same for both uniform and tapered configurations.

Increasing inter-helix spacing caused increases in uplift capacity due to a load transfer from the top helical bearing plate to the middle and bottom plates. Moreover, increasing inter-helix spacing was observed to promote a transition in the failure mechanism from cylindrical shear to individual bearing. The transition starts with a spacing ratio s_i/D_i equal to 3.

The uplift capacities of single helix piles were compared with the uplift capacities of multi-helix piles. Increasing the number of helices in a pile results in improved uplift capacities. However, pile efficiency reduces as the number of plates is increased.

5.2. Suggestions for future research

During execution of this project, other areas of study using the studied soil and manufactured pile were identified and are described below:

- An instrumentation could be developed to investigate the distribution of loads among the helical plates and its relationship with soil disturbance. Instrumented sections could also be used to study the degradation plate capacity during cyclic load tests.
- The installation equipment can also be used to install piles at inclined angles. The design of inclined piles and how they behave in group is another area that requires further study.
- The cyclic lateral load performance of the pile on sand could also be investigated.
- The instrumentation could provide new data that could be used to further improve the numerical models, taking into account factors such as load distribution, friction degradation, and installation disturbance.

REFERENCES

Abdelghany, Y. and El Naggar, M. H. 2010. Monotonic and Cyclic Behavior of Helical Screw Piles under Axial and Lateral Loading. *Fifth International Conference on Recent Advances in Geotechnical Earthquake Engineering and Soil Dynamics*. 8. http://scholarsmine.mst.edu/icrageesd/05icrageesd/session09/8.

ABNT. 1984. *ABNT NBR-6508: Grãos de solos que passam na peneira de 4,8 mm - Determinação da massa específica*. Rio de Janeiro: ABNT.

ABNT. 1990. *ABNT NBR-12004: Soil - Determination of maximum index void ratio of cohesionless soils*. Rio de Janeiro: ABNT.

ABNT. 1991. *ABNT NBR-12051: Soil - Determination of minimum index void ratio of cohesionless soils – Method of test*. Rio de Janeiro: ABNT.

ABNT. 1995. *ABNT NBR-6502: Rocks and soils - Terminology*. Rio de Janeiro: ABNT.

ABNT. 2001. *ABNT NBR-6484: Soil - Standard penetration test - SPT - Soil sampling and classification - Test method*. Rio de Janeiro: ABNT.

ABNT. 2006. *ABNT NBR-12131: Piles - static load test - test method.* Rio de Janeiro: ABNT.

ABNT. 2016. *ABNT NBR-7181: Soil – Grain size analysis*. Rio de Janeiro: ABNT.

ABNT. 2016. *ABNT NBR-8800: Design of steel and composite steel structures for buildings*. Rio de Janeiro: ABNT.

ABNT. 2016. *ABNT NBR-9813: Soil – "In situ" determination of apparent specific gravity using a core cutte*r. Rio de Janeiro: ABNT.

Airey, D. W., Al-Douri, R. H. and Poulos, H. G. 1992. Estimation of Pile Friction Degradation from Shearbox Tests. *Geotechnical Testing Journal*, GTJODJ, 15(4), pp. 388-392.

Andersen, K. A., Puech, A. A. and Jardine, R. J. 2013. Cyclic resistant geotechnical design and parameter selection for offshores engineering and other applications. In: A. Puech (Ed.), *Proceedings of TC 209 Workshop 18th ICSMGE. Design for cyclic loading: piles and other foundations.* (pp. 85-88). Paris: Presses des Ponts.

Andersen, K. H. 2009. Bearing capacity under cyclic loading — offshore, along the coast, and on land. The 21st Bjerrum Lecture presented in Oslo, 23 November 2007. *Canadian Geotechnical Journal*, 46, pp. 513-535.

ASTM International. 2011. *ASTM D1586-11, Standard Test Method for Standard Penetration Test (SPT) and Split-Barrel Sampling of Soils*, West Conshohocken, PA.

ASTM International. 2011. *D3080M-11, Standard Test Method for Direct Shear Test of Soils Under Consolidated Drained Conditions*, West Conshohocken, PA.

ASTM International. 2013. *D3689M-07(2013)e1, Standard Test Methods for Deep Foundations Under Static Axial Tensile Load*, West Conshohocken, PA.

Blanc, M., and Thorel, L. 2016. Effects of cyclic axial loading sequences on piles in sand. *Géotechnique Letters, 6*(2), pp. 163-167.

Bobbitt, D. E. and Rogers, W. 2006. "*What's Wrong with This Helical Foundation?", presented at the DFI Seminar November 11, 2006*, Newark, NJ.

Brinch-Hansen, J. 1963. The Ultimate Resistance of Rigid Piles against Transversal Forces. *Danish Geotechnical Institute Bulletin No. 12*, pp. 5-9.

Butler, H, Hoy, H. 1977. *User's manual for the Texas quick load method for foundation load testing*. Federal Highway Administration, Office of Development, Washington, DC.

Cerato, A., and Victor, R. 2009. Effects of long-term dynamic loading and fluctuating water table on helical anchor performance for small wind tower foundations. *Journal of performance of constructed facilities*, pp. 251-261.

Chan, S., and Hanna, T. 1980. Repeated loading on single piles in sand. *Journal of the geotechnical engineering division, 102*(2), pp. 171-180.

Chow, S., O'Loughlin, C., Corti, R., Gaudin, C., and Diambra, A. 2015. Drained cyclic capacity of plate anchors in dense sand: experimental and theoretical observations. *Géotechnique Letters, 5*(2), pp. 80-85.

Cintra, J. C. A., Aoki, N., and Albiero, J. H. 2011. *Fundações Diretas: Projeto Geotécnico*. Oficina de Textos. São Paulo.

Clemence, S. P. and Lutenegger, A. J. 2015. Industry survey of state of practice for helical piles and tiebacks, *DFI Journal - The Journal of the Deep Foundations Institute*, 9(1), pp. 21-41.

Clemence, S., and Smithling, A. 1984. Dynamic Uplift Capacity of Helical Anchors in Sand. *4th Australia-New Zealand Conference on Geomechanics*, (pp. 88-93). Perth.

Costa, J. P. S. and Costa, Y. D. J. 2016. Dimensionamento de protótipo de estaca helicoidal para reação em provas de carga estática em solo tropical sedimentar. *8º Congresso Luso-Brasileiro de Geotecnia*, Porto.

Costa, G. F. 2017. *Análise da zona de perturbação causada pela instalação de estacas helicoidais em solo arenoso*. Term paper. Federal University of Rio Grande do Norte, Natal.

CZM Foundation Equipment. 2012. *MC150: Technical Specifications*. São Paulo.

Das, B. 1990. *Earth anchors*, 1st ed. Amsterdam: Elsevier Science.

Davisson, M.T. 1972. “High Capacity Piles.” In *Proceedings of Lecture Series on Innovations in Foundation Construction*, ASCE, Illinois Section, Chicago (March), pp. 81–112.

DeJong, J., Randolph, M., and White, D. 2003. Interface load transfer degradation during cyclic loading: a microscale investigation. *Soils and Foundations, 43*(4), pp. 81-93.

El Sharnouby, M., and El Naggar, M. 2011. Monotonic and cyclic axial full-scale testing of reinforced helical pulldown micropiles. *Proceedings of the 14th Pan-American Conference on Soil Mechanics and Geotechnical Engineering*, (p. 6). Toronto.

Fioravante, V. 2002. On the shaft friction modelling of non-displacement piles in sand. *Soils and Foundations, 42*(2), pp. 23-33.

Gavin, K., Doherty, P., and Tolooiyan, A. 2014. Field investigation of the axial resistance of helical piles in dense sand. *Canadian Geotechnical Journal, 51*(11), 1343-1354.

Ghaly, A. and A. Hanna. 1992. Stresses and Strains around Helical Screw Anchors in Sand. *Soils and Foundations*, 32(4), pp. 27–42.

Ghaly, A. M., Hanna, A. M., and Hanna, M. S. 1991. Uplift behavior of screw anchors in sand - Part I: dry sand. *Journal of Geotechnical Engineering, 117*(5).

Ghaly, A., and Clemence, S. 1998. Pullout performance of inclined helical screw anchors in sand. *Journal of Geotechnical and Geoenvironmental Engineering, 124*(7), pp. 617-627.

Gill, H.S. and J.J. Udwari. 1980. *Pullout Tests: Multi-Helix Screw Anchors*. Report prepared for the Virginia Electric and Power Company, Richmond, VA.

Gudehus, G., and Hettler, A. 1981. Cyclic and monotonous model tests in sand. *Proceedings of the 10th International Conference on Soil Mechanics and Foundation Engineering*, *2*, pp. 211-214. Stockholm.

Hanna, T., Sivapalan, E., and Senturk, A. 1978. Behaviour of dead anchors subjected to repeated and alternating loads. *Ground Engineering, 11*(3), pp. 28-34, 40.

Hansen, J. B. (1970). A Revised and Extended Formula for Bearing Capacity. *Danish Geotechnical lnstitute Bulletin*, 28, Copenhagen, 21 pp.

Hoyt, R., and Clemence, S. 1989. Uplift capacity of helical anchors in soil. In: P. C. ICSMFE (Ed.), *Proceedings of the 12th International Conference on Soil Mechanics and Foundation Engineering* (pp. 13-18). Rio de Janeiro: CRC Press.

Hubbell Power Systems, Inc.. 2014. *Technical Design Manual*. 3rd ed. Hubbell Power Systems, Inc., Centralia, MO.

ICC-Evaluation Services. 2007. *AC358 Acceptance Criteria for Helical Pile Foundations and Devices.* www.icc-es.org.

Ilamparuthi, K., Dickin, E.A., and Muthukrisnaiah, K. 2002. Experimental investigation of the uplift behaviour of circular plate anchors embedded in Sand. *Canadian Geotechnical Journal*, 39, pp. 648–664.

International Code Council. 2014. *2015 International Building Code (IBC)*. Washington, DC: International Code Council.

Jardine, R., and Standing, R. 2000. *Pile load testing performed for HSE cyclic loading study at Dunkirk, France. Two Volumes.* Offshore Technology Report, Health and Safety Executive, London.

Jesus, A. P. 2002. *Caracterização Geológica, Geomorfológica e Geotécnica de um Corpo de Dunas na Cidade de Natal/RN*. MSc Thesis, Federal University of Rio Grande do Norte, Natal.

Karlsrud, K., Nadim, F., and Haugen, T. 1986. Piles in clay under cyclic axial loading: field tests and computational modeling. In: I. F. Chaissées (Ed.), *Proceedings of the 3rd International Conference of Numerical Methods in Offshore Piling* (pp. 165-190). Nantes: Technip.

Kulhawy, F. H. 1984. Limiting tip and side resistance-Fact or fallacy, *Analysis and Design of Pile Foundations*, ed. J. R. Meyer, ASCE, New York, N.Y., pp. 80-98.

Livneh, B. and El Naggar, M. 2008. Axial testing and numerical modeling of square shaft helical piles under compressive and tensile loading. *Canadian Geotechnical Journal*, 45(8), pp.1142-1155.

Lutenneger, A.J. 2011. Behavior of multi-helix screw anchors in sand. *Proceedings of the 14th Pan-American Conference on Soil Mechanics and Geotechnical Engineering*, Toronto.

Lutenegger, A. J and Tsuha, C. H. C. 2015. Evaluating Installation Disturbance from Helical Piles and Anchors Using Compression and Tension Tests. In: Manzanal, D and Sfriso, A. O (Eds.), From Fundamentals to Applications in Geotechnics. (pp. 373-381). IOS Press.

Lutenegger, A. J., Erikson, J., and Williams, N. 2014. Evaluating Installation Disturbance of Helical Anchors in Clay from Field Vane Tests. Deep Foundations Institute.

Meyerhof, G.G. 1951. The Ultimate Bearing Capacity of Foundations. *Geotechnique*, 2(4), pp. 301–331.

Meyerhof, G.G. and J.I. Adams. 1968. The Ultimate Uplift Capacity of Foundations. *Canadian Geotechnical Journal*, 5(4), pp. 224–244.

Mitsch, M. P., and Clemence, S. P. 1985. The uplift capacity of helical anchors in sand. *Uplift behavior of anchor foundations in soil* (pp. 26-47). Michigan: ASCE.

Moraes, L. S. 2014. Análise numérica de dutos enterrados sujeitos a elevação e recalque localizado. MSc Thesis, Federal University of Rio Grande do Norte, Natal.

Moreira, M. M., Souza, N. M., Cuellar, M. D. Z., and Arraes, K. A. 2014. Carta Geotécnica do Município de Natal-RN: Áreas de Risco de Deslizamentos e Inundações. *XVII Congresso Brasileiro de Mecânica dos Solos e Engenharia Geotécnica*, ABMS, Goiânia.

Murray, E. J., and Geddes, J. D. 1987. Uplift of anchor plates in sand. *Journal of Geotechnical Engineering*, ASCE, 113(3), pp. 202-215.

Narasimha Rao, S., Y.V.S.N. Prasad, and C. Veeresh. 1993. Behavior of Embedded Model Screw Anchors in Soft Clays. *Geotechnique*, 43, pp. 605–614.

Nazir, R., Chuan, H. S., Niroumand, H., and Kassim, K. A. 2014. Performance of single vertical helical anchor embedded in dry sand, *Measurement*, 49, pp. 42-51,

Nogueira A.M.B. 1981. *O cenozóico continental da região de Natal*. MSc Thesis, Federal University of Pernambuco, Recife.

Perko, H. 2009. *Helical piles: a practical guide to design and installation.* J. W. Sons, Ed.

Perlow Jr., M. 2011. Helical Pile Acceptance Criteria, Design Guidelines and Load Test Verification. *Geo-Frontiers Congress 2011*, ASCE, Dallas, pp. 94-102.

Plaxis. 2016. *Plaxis 2D 2016: Reference Manual*. The Netherlands.

Poulos, H. 1988. Cyclic stability diagram for axially loaded piles. *Journal of Geotechnical Engineering, 114*(8), pp. 877-895.

Poulos, H. 1989. Cyclic axial loading analysis of piles in sand. *Journal of Geotechnical Engineering, 115*(6), pp. 839-852.

Puech, A., Benzaria, O., Thorel, L., Garnier, J., Foray, P., Silva, M., and Jardine, R. 2013. Cyclic stability diagrams for piles in sands. In: A. Puech (Ed.), *Proceedings of TC 209 Workshop 18th ICSMGE. Design for cyclic loading: piles and other foundations.* (pp. 85-88). Paris: Presses des Ponts.

Queiroz, F. L. 2018 (in print). *Comportamento à tração de estacas helicoidais instrumentadas em areia submetidas a carregamento cíclico estático e quase estático*. MSc Thesis, Federal University of Rio Grande do Norte, Natal.

Rao, S., Prasad, Y. and Shetty, M. 1991. The behavior of model screw piles in cohesive soils, *Soils and Foundations*, 31, pp. 35–50.

Rimoy, S., Jardine, R., and Standing, J. 2013. Displacement response to axial cycling of piles driven in sand. *Proceedings of the Institution of Civil Engineers-Geotechnical Engineering, 166*(2), pp. 131-146.

Ruberti, M. 2015. Investigation of installation torque and torque-to-capacity relationship of screw-piles and helical anchors. *Geotechnical Engineering Masters Projects*. 1. http://scholarworks.umass.edu/cee_geotechnical/1.

Sailer, D. and Soth, B. 2004. Helical Pier Foundations for Problem Sites. *Journal of Light Construction* (May).

Sakr, M. 2010. High Capacity Helical Piles – A New Dimension for Bridge Foundations. Proceedings of the 8th Internation Conference on Short and Medium Span Bridges, 142, Niagara Falls, Canada.

Santos Jr., O. F.; Chaves, L. F. M. 2005. A Prática da Engenharia de Fundações na Região de Natal – RN. In: Gusmão, A. D.; Gusmão Filho, J.; Oliveira, J. T. R.; Maia, G. de B. (Eds.), *Geotecnia no Nordeste*. (pp. 282-293). Editora Universitária UFPE. Recife.

Schiavon, J. A. 2016. *Comportamento de ancoragens helicoidais submetidas a carregamentos cíclicos*. PhD thesis, University of São Paulo and Nantes Angers and Le Mans University, São Carlos.

Science Museum Group. 1838-1887. *Model of the lighthouse on the Maplin Sands*. 1899-41. Science Museum Group Collection Online. Retrieved from https://collection.sciencemuseum.org.uk/objects/co55426.

Seider, G. 2004. Helical Foundations: What an Engineer Needs to Know. *Structure Magazine*, 11(6), pp. 27–28.

Silva, E. A. J., Santos Jr., O. F., Jesus, A. P.; Amaral, R. F. 2002. Caracterização Geológica, Geomorfológica e Geotécnica de Sedimentos do Setor Sul de Natal/RN, com Base em Análises de Perfis de Sondagens de Simples Reconhecimento. *10° Congresso Brasileiro de Geologia de Engenharia e Ambiental*. Ouro Preto.

Tappenden, K. M. 2006. "Screw Piles: Use and Design." www.almita.com/html/technical/html.

Terzaghi, K. 1943. *Theoretical Soil Mechanics*. New York: John Wiley and Sons.

Tsuha, C. H. C. 2007. *Theoretical model to control on site the uplift capacity of helical screw piles embedded in sandy soil.* DSc thesis, University of São Paulo, Department of Geotechnical Engineering, São Carlos.

Tsuha, C. H. C. and Aoki, N. 2010. Relationship between installation torque and uplift capacity of deep helical piles in sand. *Canadian Geotechnical Journal*, 47(6), pp. 635-647.

Tsuha, C. H. C., Aoki, N., Rault, G., Thorel, L., and Garnier, J. 2012a. Evaluation of the efficiencies of helical anchor plates in sand by centrifuge model tests. *Canadian Geotechnical Journal, 46*(9), pp. 1102-1114.

Tsuha, C. H. C., Foray, P., Jardine, R., Yang, Z., Silva, M., and Rimoy, S. 2012b. Behaviour of displacement piles in sand under cyclic axial loading. *Soils and foundations, 52*(3), pp. 393-410.

Tsuha, C. H. C., Santos, T. C., Rault, G., Thorel, L. Garnier, J. 2013. Influence of multiple helix configuration on the uplift capacity of helical anchors. *Proceedings of the 18th International Conference on Soil Mechanics and Geotechnical Engineering*, pp. 2893-2896, Paris.

Turner, J., and Kulhawy, F. 1990. Drained uplift capacity of drilled shafts under repeated axial loading. *Journal of geotechnical engineering, 116*(3), pp. 470-491.

Urabe, K., Tokimatsu, K., Suzuki, H., and Asaka, Y. 2015. Bearing capacity and pull-out resistance of wing piles during cyclic vertical loading. In *Proceedings of the 6th International Conference on Earthquake Geotechnical Engineering*. Christchurch.

USACE Engineering and Design Manual. 1991. *Design of pile foundations*, EM 1110-2-2906, US Army Corps of Engineers, Washington, DC.

Van Weele, A. 1979. Pile bearing capacity under cyclic loading compared with that under static loading. *Proceedings of the 2nd International Conference on the Behaviour of Off- Shore Structures*, *1*, pp. 475-488. Bedford.

Veesaert, C. J. and Clemence, S. P. 1977. Dynamic pullout resistance of pullout anchors in sand. *Proceedings of the International Symposium on Soil-Structure Interaction*. Roorkee, India, pp. 389-397.

Vesic, A.S. 1973. Analysis of Ultimate Loads of Shallow Foundations. *Journal of Soil Mechanics and Foundation Design*, 99(SM 1), pp. 45–73.

Victor, R. and A. Cerato. 2008. Helical Anchors as Wind Tower Guyed Cable Foundations. In *Proceedings of the BGA International Conference on Foundations*. Dundee, Scotland: HIS BRE Press.

Wichtmann, T. 2005. *Explicit accumulation model for non-cohesive soils under cyclic loading.* PhD thesis, Ruhr University Bochum, Bochum.

Zhang, D. 1999. *Predicting capacity of helical screw piles in Alberta soils.* MSc Thesis, University of Alberta, Edmonton.